EXPERIMENTAL STUDY OF NANOSECOND PULSED DISCHARGES AND DC-DRIVEN HELIUM PLASMA JETS

by

Xingxing Wang

A Dissertation

Submitted to the Faculty of Purdue University

In Partial Fulfillment of the Requirements for the degree of

Doctor of Philosophy

School of Aeronautics and Astronautics

West Lafayette, Indiana

August 2021

THE PURDUE UNIVERSITY GRADUATE SCHOOL
STATEMENT OF COMMITTEE APPROVAL

Dr. Alexey Shashurin, Chair

School of Aeronautics and Astronautics

Dr. Sergey Macheret

School of Aeronautics and Astronautics

Dr. Sally Bane

School of Aeronautics and Astronautics

Dr. Alina Alexeenko

School of Aeronautics and Astronautics

Approved by:

Dr. Gregory Blaisdell

To my parents,
Wang Bo & Huang Yin
&
my girlfriend
Yuying Huang

ACKNOWLEDGMENTS

Firstly, I would like to express my deepest appreciation to my advisor, Dr. Alexey Shashurin. I am extremely grateful for the effort and time you spent on mentoring me. Despite of the excellent research environment, numerous opportunities in/outside of the lab, and financial support you provided, the most important thing is that you are the role model of what a research experimentalist should be.

I would also like to extend by gratitude to all other committee members including Dr. Sally Bane, Dr. Sergey Macheret, and Dr. Alina Alexeenko. Your advice and support really help me polishing my research work. It would not be possible for me to accomplish my thesis to this level without you.

Many thanks to all the fellow graduate students that I have worked with. It has been a pleasure working with every single one of you. Special thanks to certain individuals, including but not limited to: Omar Dary, Andrei Khomenko, and Adam Patel. I learned a lot from Omar in my early years of master's degree study when I knew very little about experimental skills. In addition, it was a joy working with Andrei: his serious and prudent attitude and superb experimental skills always urge me to do better. I would also not be able to finish the last pieces of my dissertation without the help from Adam with his laser expertise.

I also gratefully acknowledge all the staff for their assistance including Morgan Delaney, Xiaomin Qian, Beverly Clenden, Amdanda Dalton, and many others.

TABLE OF CONTENTS

LIST OF TABLES 8
LIST OF FIGURES 9
ABBREVIATIONS 13
ABSTRACT 15
1 INTRODUCTION 17
1.1 Atmospheric pressure plasmas 17
1.2 Corona, streamer, and atmospheric pressure plasma jet (APPJ) 18
1.3 Nanosecond repetitively pulsed (NRP) pin-to-pin discharges 19
1.4 Microwave Rayleigh scattering (MRS) 20
1.4.1 Theory of MRS 20
1.4.2 Applications of MRS 24
1.5 Motivation 26
1.6 Objectives 27
1.7 Outline 28
2 DEVELOPMENT OF DIAGNOSTIC TECHNUQES FOR NRP PIN-TO-PIN DISCHARGES 30
2.1 Time-revolved measurements of electron density in nanosecond pulsed plasmas using microwave scattering 30
2.1.1 Abstract 30
2.1.2 Introduction 30
2.1.3 Experimental setup 33
2.1.4 Results and Discussion 35
2.1.5 Conclusion 38
2.2 Gas thermometry by optical emission spectroscopy enhanced with probing nanosecond plasma pulse 38
2.2.1 Introduction 38
2.2.2 Methods and Equipment 40
2.2.3 Results and Discussion 42
2.2.4 Conclusion 46

2.3 Combined microwave and laser Rayleigh scattering diagnostics for pin-to-pin nanosecond discharge 47
2.3.1 Abstract 47
2.3.2 Introduction 47
2.3.3 Experimental details 49
2.3.4 Results and discussion 52
2.3.5 Conclusion 59
3 STUDY OF THE NRP PIN-TO-PIN DISCHARGES 60
3.1 Experimental study of atmospheric pressure nanosecond discharge in pin-to-pin configuration 60
3.1.1 Abstract 60
3.1.2 Introduction 61
3.1.3 Methodology and Experimental Setup 62
3.1.4 Results and Discussion 67
3.1.4.1 Discharge Regimes 67
3.1.4.2 Spark Regime 69
3.1.4.2.1 Typical discharge parameters 69
3.1.4.2.2 Effect of pulse energy on discharge parameters 74
3.1.4.2.3 Effect of gap distance on discharge parameters 80
3.1.4.3 Corona Regime and Comparison with Spark 83
3.1.5 Conclusion 86
3.2 Experimental study of pin-to-pin nanosecond pulsed (NRP) discharges at atmospheric conditions with different pulsing frequency. 87
3.2.1 Abstract 87
3.2.2 Introduction 88
3.2.3 Experimental setup 89
3.2.4 Results and discussion 90
3.2.5 Conclusion 99
4 STUDY OF THE DC-DRIVEN HELIUM PLASMA JET 100
4.1 DC-driven plasma gun: self-oscillatory operation mode of atmospheric-pressure helium plasma jet comprised of repetitive streamer breakdowns 100

4.1.1 Abstract 100
4.1.2 Introduction 100
4.1.3 Experimental setup 101
4.1.4 Results and Discussion 102
4.1.5 Conclusion 108
4.2 Enhancement of positive pulsed corona by dielectric enclosure 110
4.2.1 Abstract 110
4.2.2 Introduction 110
4.2.3 Experimental setup 112
4.2.4 Experimental results and discussion 114
4.2.5 Conclusion 121
4.3 Study of atmospheric pressure plasma jet parameters generated by DC voltage driven cold plasma source. 121
4.3.1 Abstract 121
4.3.2 Introduction 122
4.3.3 Methods and equipment 123
4.3.4 Results and discussion 127
4.3.5 Conclusion 132
5 CONCLUSIONS 133
5.1 Summary 133
5.2 Recommendation for future work 134
PUBLICATIONS AND PRESENTATIONS 136
APPENDIX A –VIBRATIONAL TEMPEARTURE OF N_2 AT GROUND STATE 137
REFERENCES 139

LIST OF TABLES

Table 1. Summary of the discharge properties in the two regimes observed in this work: spark ($d \leq 6$ mm) and corona ($d \geq 8$ mm). 69

Table 2. Frank-Condon coefficients for nitrogen Tanaka band system (C-X) 138

LIST OF FIGURES

Fig 1-1. Schematics of horns and plasma orientation. E-field is parallel to the page and H-field is oscillating perpendicular to the page. 21

Fig 1-2. MRS measurements of plasma parameters in non-equilibrium atmospheric pressure plasma jet (APPJ). (a-b) Regular and fast photograph of APPJ; (c) Temporal evolution of discharge parameters and plasma density in APPJ measured by MRS diagnostics..... 24

Fig 1-3. Temporal evolution of plasma density, plasma conductivity, and electric field obtained using the MRS technique in electrosurgical discharge. 25

Fig 1-4. Absolute measurements of parameters of fs-laser induced plasmas in air. (a-b) Total number of electrons in laser-induced plasma volume $\mathbf{Ne(t)}$; (c) Photoionization rates; (d-e) Plasma density vs. laser intensity and 2D distribution of the plasma density for $\mathbf{I0 = 2.68 \times 1013\ W/cm2}$..... 26

Fig 2-1. Voltage pulse applied to the electrodes without breakdown of the electrode gap. 33

Fig 2-2. (a) Schematic of the RMS system. (b) Entire experimental setup. 35

Fig 2-3. Images of an NRP discharge plasma in a pin-to-pin electrode configuration with varying gap distances L at different moments of time after breakdown. The distribution of intensities for each case is plotted on the right-hand side of each ICCD image. (a) L = 2mm; (b) L = 5mm; (c) L = 8 mm. Exposure time = 3 ns. 36

Fig 2-4. (a) Temporal evolution of ne and Ne on the μs time scale. (b) Temporal evolution of voltage, current, and Ne on the ns time scale. 37

Fig 2-5. peak value of ne and Ne vs gap distance L 37

Fig 2-6. Schematics of the OES measurement system 41

Fig 2-7. Sample waveform illustrating NRP discharge pulse and subsequent probing pulse applied with delay $\Delta t = 20$ μs. 42

Fig 2-8. Temporal evolution of V, I, T_{rot} and T_{vib} for NRP discharge..... 43

Fig 2-9. Full spectrum from 200 nm to 800 nm of the light emission of the discharge. (a) initial 20 ns after the breakdown, (b) 20-40 ns after the breakdown. 43

Fig 2-10. Voltage/current waveform of the probing pulse with $\Delta t = 20$ μs. The shaded square represents the duration when the ICCD camera gate was open. The waveform of the probing pulse was different from that of the NRP discharge pulse in Fig 3 due to the impedance change between the electrodes in the wake of the NRP discharge..... 44

Fig 2-11. Temporal evolution of the rotational temperature measured using OES technique enhanced by nanosecond probing pulse. (a) in linear time scale, (b) in log time scale. 46

Figure 2-12. Schematic of the ns-discharge setup (blue), MRS diagnostic equipment (gold), and LRS diagnostic equipment (green). 50

Figure 2-13. Voltage (red) and current (blue) waveforms of the nanosecond HV pulse..... 52

Figure 2-14. (a) Temporal evolution of the plasma diameter and volume. Black line + scatter: visual measurement for diameter; Blue line + scatter: calculated plasma volume. (b) Sample ICCD images of the plasma dimensions. 53

Figure 2-15. Temporal evolution of U_{out} measured by the MRS system. Three distinct regions of microwave scattering behavior are distinguished by the dashed red lines. 54

Figure 2-16. (a) Temporal evolution of local gas density measured by LRS. (b) Example profiles of the density distribution along the radial direction of plasma filament for 1-5 μs after discharge. A sample of the LRS raw image is displayed on the left-bottom corner at t = 3 μs. 57

Figure 2-17. Temporal evolution of (a) N_e and (b) n_e. 58

Figure 3-1. Schematic of the experimental setup. (Blue) Pulse generator and voltage/current diagnostics. (Green) Laser Rayleigh scattering equipment. (Red/Orange) OES equipment. (Yellow) Microwave Rayleigh scattering equipment. 63

Figure 3-2. V-I waveform of a pulse: (a)without breakdown with dielectric between electrodes; (b) in corona regime at 10 mm; (c) in spark regime at 2mm. ICCD images for corona and spark regime are also presented to the side of the V-I curve for each regime. 68

Figure 3-3. Temporal measurement of discharge parameters within the pulse at d = 5 mm. Moments of two breakdowns (BD) events are also labeled. 70

Figure 3-4. Temporal evolution of gas temperature T_{gas} within the pulse and post-discharge. (a) linear scale; (b) log scale 71

Figure 3-5. (a) Temporal evolution of ng measured by LRS. Radial profile of the relative density perpendicular to the plasma filament for (b) t = 1-5 μs after discharge, (c) 5-1000 μs after discharge. 72

Figure 3-6. (a) Temporal evolution of plasma diameter and volume. Black: diameter; blue: volume. (b)ICCD image of the plasma. 72

Figure 3-7. Temporal evolution of N_e (top) and n_e (bottom). The insert images indicate first 300 ns of the discharge in detail. The grey area represents the duration of the ns-pulse. 74

Figure 3-8. Temporal measurement for different energy deposition. (a) voltage; (b) reduced field; (c) current; (d) energy; (e) gas temperature; (f) vibrational temperature; (g) total electron number; (h) electron number density 77

Figure 3-9. Temporal evolution of T_{gas} for different energy deposition within and after the HV pulse. 78

Figure 3-10. (a) Full temporal evolution of relative gas density for different energy deposition. (b)Temporal evolution of gas density and plasma diameter post-discharge for different energy deposition within the first 5 μs. Solid line + square; relative gas density; dash line + triangle: plasma diameter. 79

Figure 3-11. Temporal evolution of N_e and n_e for different energy deposition. (a) N_e; (b) n_e..... 79

Figure 3-12. Temporal evolution of (a) voltage; (b) reduced field; (c) current; (d) energy; (e) gas temperature; (f) vibrational temperature; (g) total electron number; (h) electron number density for d = 2, 4, 6 mm 81

Figure 3-13. (a) voltage and reduced field at breakdown, (b) Peak value of current, (c) Energy input and energy input per unit length with respect to gap distance from 2 to 6 mm. (d) N_e after BD1, (e) n_e after BD1 with respect to gap distance from 2 to 6 mm. 82

Figure 3-14. Temporal evolution of T_{gas} for d = 2, 4, 6 mm 83

Figure 3-15. Temporal evolution of (a) voltage and (b) current for corona regime at d = 8 mm 84

Figure 3-16. Dependence of conducting current and peak N_e on d for corona regime 85

Figure 3-17. Discharge parameters vs d: (a) breakdown voltage. (b) peak current. (c) total energy input and energy input per gap distance. (d) total electron and electron per gap distance. Regime of spark and corona are colored by red and green background, respectively. 86

Figure 3-18. Voltage/current waveform. (a1) V-I waveform of a 10-pulse burst at 1 kHz. (a2) V-I waveform of a single pulse at quasi-steady-state at 1 kHz. (b1) V-I waveform of a 15-pulse burst at 10 kHz. (b2) V-I waveform of a single pulse at quasi-steady-state at 10 kHz. (c1) V-I waveform of a 15-pulse burst at 100 kHz. (c2) V-I waveform of a single pulse at steady-state at 100 kHz. 92

Figure 3-19. Energy deposition per pulse vs. number of pulses for different repetition frequencies 94

Figure 3-20. Gas temperature vs. number of pulses for different repetition frequencies 95

Figure 3-21. Relative gas density vs number of pulses for different repetition frequencies 96

Figure 3-22. Temporal evolution of n_e at (a) 10 kHz; (b) 100 kHz 99

Figure 4-1 Schematics of the experiment setup 102

Figure 4-2 (a) Current and voltage waveforms of series of the streamer breakdowns excited by the 5 kV DC voltage supplied to the electrode. (b) Current and voltage waveforms of an individual streamer breakdown. [t1]-[t6] are the time periods when a photograph of the streamer was taken. (c) Photographs of the streamer at certain time from [t1] to [t6]. The grounded electrode was located at $d \approx$ 0.5 m. The He flow rate was 1 L/min. 103

Figure 4-3 Breakdown voltage required for triggering the first streamer for three different sizes of spherical electrodes. Threshold electric field required for the breakdown is about 2.5 kV/cm regardless the electrode size. 105

Figure 4-4 Streamer breakdowns vs. He flow rate for d = 5 cm and U = 5000 V. 106

Figure 4-5 Average period between streamer breakdowns vs. distance to the grounding plate d. Flow rate = 1 L/min, U= 5000 VDC. 107

Figure 4-6 Photographs of the APPJ driven by DC high voltage. (a) Length of the free jet is about 1 cm, (b) Length of the plasma jet can be extended to 2 cm if finger is placed nearby. He flow rate is 2 L/min and U = 3400 V. 109

Figure 4-7. Current and voltage waveforms of the APPJ driven by DC high voltage. (a) Multiple breakdown events. (b) Temporally resolved individual breakdown. 109

Fig 4-8. Experimental setup for the case without Teflon enclosure (a) and with Teflon enclosure (b). 113

Fig 4-9. Electric circuitry used in the experiment. 113

Fig 4-10. Schematics of the system utilized for testing reactive gases produced by the plasma source. 114

Fig 4-11. Temporal evolution of current of DC-driven pulsed corona without dielectric. (a) Series of current pulses, (b) Typical appearance of the individual current pulse. 115

Fig 4-12. Frequency of current pulses vs. DC voltage at different gap distances without Teflon (a). Peak value of current pulses vs DC voltage at different gap distances without Teflon (b). 116

Fig 4-13. Frequency of current pulses vs. DC voltage at different gap distances with Teflon enclosure (a). Peak value of current pulses vs DC voltage at different gap distances with Teflon enclosure (b) 117

Fig 4-14. Comparison of the average discharge power with and without Teflon enclosure for 5 mm gap distance. 118

Fig 4-15. Ozone (a) and nitrogen dioxide (b) concentrations with respect to inverse air flow. The points with zero inverse air flow (or infinite air flow) correspond to plasma-off case. 120

Figure 4-16. Schematic of the DC driven plasma device 124

Figure 4-17. DC driven plasma device when DC voltage was 5 kV and helium flow rate was 5 LPM 124

Figure 4-18. Setup of the Rayleigh Microwave Scattering system 126

Figure 4-19. Setup of the optics for OES measurement 127

Figure 4-20. Waveforms of current and voltage of series streamer breakdowns. Current is generated in pulses with a constant 5 kV applied voltage. The region marked in dashed rectangle is presented in Figure 4-21. 128

Figure 4-21. (a) Waveforms of current, voltage, and N_e from a single streamer breakdown. [t1]-[t5] represents the times periods when the intensifier of the ICCD camera is working. (b) Photograph of the streamer at certain times from [t1] to [t5]. This image is taken during a single breakdown. 128

Figure 4-22. T_{rep} of the streamer breakdown vs. the applied voltage 129

Figure 4-23. Waveforms of current, N_e and n_e from one streamer breakdown 130

Figure 4-24. Maximum of current and n_e vs applied voltage 131

Figure 4-25. Measurement by OES. (a) Measured and simulated spectrum when applied voltage was 5 kV. (b) T_{rot} and T_{vib} when applied voltage is between 4.7 kV and 5 kV. 132

ABBREVIATIONS

A	Proportionality factor of MRS system
C	Capacitance
d	Gap distance between electrodes
D	Diameter of plasma channel
E	Incident electric field
e	Electron charge
$\mathscr{E}$	Energy
f	Repetition frequency
I_{cond}	Conduction current
I_d	Discharge current
I_{disp}	Displacement current
k	Depolarization factor
k_1	Attachment coefficient for $e + O_2 + O_2 \rightarrow O_2^- + O_2$
k_2	Attachment coefficient for $e + O_2 + N_2 \rightarrow O_2^- + N_2$
l	Length of scatterer
m	Electron mass
N_e	Total electron number
n_e	Electron number density
n_g	Gas density
p	Dipole moment
p	Pressure
P	Power
r	Distance between source of radiation and scattered object
R	Resistance
s	Amplitude of electron oscillation
t	Time
T	Temperature

T_e	Electron temperature
T_{gas}	Gas temperature
T_{rot}	Rotational temperature
T_{vib}	Vibrational temperature
U_{out}	Signal output of MRS system
V_0	Volume
V_d	Discharge voltage
V_{dr}	Drift velocity
α	Ionization coefficient
β	Recombination rate
ε	Relative permittivity
ε_0	Dielectric permittivity of vacuum
λ	Wavelength of incident microwave
ν	Collisional frequency for momentum-transfer
ν_{att}	Attachment rate
σ	Conductivity
σ_8	Cross-section for 8-photon ionization
ω	Incident microwave frequency
τ	Characteristic rise time of voltage

ABSTRACT

Atmospheric pressure plasma has been found valuable for numerous kinds of applications in multiple fields. The capabilities of it being operable under atmospheric pressure/room temperature, efficiently producing active gas species, and quickly depositing energy into the gas volume have earned its irreplaceable role in the field of aerodynamics, combustion, food, medicine, material processing, and nanotechnology. This work focuses on the diagnostics of two specific kinds of atmospheric pressure plasmas: nanosecond pulsed discharges with pin-to-pin configuration, and DC-driven helium plasma jet, with an emphasis on the application of microwave Rayleigh scattering for the electron number (density) measurement.

Firstly, a large set of diagnostic tool infrastructure was built. It includes development of diagnostic techniques based on the traditional methods that expand their default capabilities - for instance, OES measurement assisted with HV probing pulse. In addition, the accuracy of the electron number density measurement by MRS was further improved by the simultaneous measurement of gas density by LRS.

Secondly, the study of the nanosecond high-voltage discharges with pin-to-pin configuration was conducted, in which multiple discharge parameters were measured, including discharge voltage, current, temperatures (gas/rotational/vibrational), gas density, electron number/number. Multiple discharge conditions were also studied, such as different pulse energy, gap distance between electrodes, and pulsing frequency. To start with, two discharge regimes (spark and corona) were identified by different discharge properties and visual presentations. It was further demonstrated that discharges are operating within spark regime at smaller gap distances (<6 mm) and corona at larger distances (>8mm). Within the spark regime under single pulsed condition, a higher electron number density, current, temperature was achieved at smaller gap distances, with a maximum value of 7.5×10^{15} cm^{-3}, 22 A, and 4000 K (10 μs after discharge) at a gap distance of 2 mm, respectively. Lower electron number density/current/temperature was observed at 5mm gap by lowering the pulse energy with additional current-limiting resistors. Electrons after discharge decayed with a characteristic decay time of 150-200 ns governed by a mix of dissociative recombination and three-body attachment. Gas properties including temperature and density recovered to ambient level within approximately 1 ms. In addition, higher temperature, lower gas density, and lower electron number density were measured at higher

repetition frequency where: above 5000 K (minimum gas temperature), 2.0×10^{18} cm^{-3}, 1.0×10^{15} cm^{-3} were measured at a repetition frequency of 100 kHz, respectively. The decay rate of electrons was also lowered at higher repetition frequency due to a lower gas density and electron temperature. A substantially lower pulse energy, gas heating, and electron production was achieved within the corona regime.

Thirdly, a new type of atmospheric pressure plasma jet was proposed in this work driven by DC high-voltage where the supplied DC voltage was held constant during operation. The discharges however were firing repetitively in the kHz range in auto-oscillatory mode. Each discharge pulse is associated with a streamer discharge event with a current amplitude ~ 1mA and a duration ~ 5 μs. The electron number density of the resulting plasma volume was measured to be on the order of 10^{11} cm^{-3} by microwave Rayleigh scattering. The gas temperature of the plasma jet was also measured to be less than 400 K with optical emission spectroscopy. The governing breakdown mechanism of this DC-driven plasma jet, namely, flashing corona, was further investigated. It has been shown that an enclosure of dielectric material could increase the pulsing frequency by 10 times and enhance the intensity of each discharge so that the peak current increases from 14 to 35 mA. Furthermore, the applicability of such discharge for sterilization was assessed by quantifying the energy cost of the production of ozone and NOx, which were 150 eV and 1950 eV per molecule, respectively.

1 INTRODUCTION

1.1 Atmospheric pressure plasmas

Atmospheric pressure plasmas have been a trending topic for the last few decades for multiple of their unique characteristics. [1] [2] Unlike traditional plasmas which only exist in the chamber at low pressures, atmospheric pressure plasmas are operable at atmospheric pressure or higher, enabling better accessibility in a more comprehensive range of applications. The nature of atmospheric pressure plasma being highly non-equilibrium implies that the bulk temperature of the plasma can be contained to be close to room temperature. It has also been investigated as a source for efficient production of certain kinds of gas species (atomic oxygen, NO, etc). [3]

Given the uniqueness described above, atmospheric pressure plasmas have been proven to be promising in various applications. The ability to produce active species such as atomic oxygen (thus ozone and hydroperoxide) and NO makes it an ideal means for sterilization in the industry of food, medicine, etc. [4] [5] It is especially applicable to any temperature-sensitive objects since the plasma is 'cold', such as organic tissues, non-heat-resistive materials, and even the human body. [6] [7] It further amplifies its advantage in wound sterilization compared to traditional means such as alcohol for leaving no residuals and doing no additional damage to the wounds. Atmospheric pressure plasmas have been found to be especially valuable in the dentistry industry for being effective in treating intraoral diseases, root canal sterilization, composite restoration, and tooth bleaching. [8] Atmospheric pressure plasmas have also been found to be a prominent source of species such as H and OH which can be valuable in the field of assisted combustion. [9] [10] [11] On the other hand, one can precisely adjust the energy input of the plasma for heat treatment on the microscale on material surfaces. In the field of material processing, in addition to deposition of coatings, it can thus be utilized for material surface processing by etching and roughening. [12] Additionally, the implementation of microdischarges in the form of dielectric-barrier-discharges (DBD) on the surface of the airfoil can effectively delay flow separation and thus reduce drag by energy addition, which is very well known as the plasma actuator. [13] [14] Many other fields that show interest in atmospheric pressure plasmas include nanotechnology, medicine, etc. [1] [15] [16] [17]

This work focuses on the study of two specific atmospheric plasma objects: atmospheric pressure plasma jets (APPJ) and nanosecond repetitively pulsed (NRP) discharges with pin-to-pin configuration; substantial efforts were put in the development of microwave scattering diagnostics.

1.2 Corona, streamer, and atmospheric pressure plasma jet (APPJ)

Corona discharge occurs when the local electric field is highly ununiform. It most commonly appears around sharp edges of high-voltage components as a luminous glow region. Unlike those that are generally desired to be prevented, corona discharge plays an essential role in the plasma production at atmospheric pressures for its low current density compared to glow and arc. One particular type of corona discharge is called 'flashing corona'. When a pointed high voltage electrode is placed in the vicinity to grounded potential, under certain conditions, corona discharges are firing repetitively in the range of kHz without significant change of the voltage. When a wave of corona discharge occurs, gas near the anode is ionized, and electrons are pulled into the anode. The resulting positive ions accumulate in the vicinity to the anode, and this positively charged cloud exhibits a counter field to the anode. The anode is thus 'shielded', and further discharge is prohibited. As ions are slowly pulled away towards the cathode, the field near the anode is restored, and corona discharge is again initiated. It was also found that the repetition frequency of flashing corona first increases then decreases when the ground potential was brought closer to the high voltage point. [18]

Corona discharges at atmospheric pressure are supported by streamers, which are defined as filamentary ionization channels originate from the electrode with a highly ununiform field and propagate towards another electrode. As the streamer propagates, the highly nonuniform electric field is carried by the tip of the streamer, where additional gas molecules are ionized, electrons from ionization are pulled towards anode along the path of the streamer, and the positive ions are however left still. The path of the streamer, therefore, is extended. [18] Streamers usually propagate randomly in all directions but can also be 'guided' by an external field. In another particular case, which applies to the modern atmospheric pressure plasma jet (APPJ), the path of the streamer propagation is confined by the flow path of the noble gas (helium or argon), because plasma quickly quenches when reaching air on the boundary where oxygen with high concentration exists. The firing frequency of streamers is normally controlled by the frequency of the driving power that a wave of ionization initiates whenever the local field reaches its threshold

value, and typical APPJ devices are producing streamers at a frequency of kHz in sync with the driving power. Streamers are therefore propagating along the noble gas flow with illumination at a very high 'refresh rate', which forms a plasma jet to the naked eye.

APPJs can be generated in various kinds of setups and gas media according to specific needs. It can also be powered by high voltages in the form of AC, pulsed DC, or RF and microwaves. [2] Types of gases utilized include helium, argon, or a mixture of oxygen/nitrogen with helium/argon. Various kinds of diagnostic techniques have been utilized for the diagnostic of atmospheric pressure plasmas. Voltage/current was measured by traditional probes; temperatures (rotational and vibrational) were measured by optical emission spectroscopy (OES); concentration of certain species can be determined utilizing OES as well as laser-based techniques such as LIF. [19] As one of the most critical parameters of the plasma, electron number density has been measured by OES (e.g., Stark broadening [20]), laser Thomson scattering, [21] etc. As presented in work [22], microwave Rayleigh scattering has also been proven to be a promising technique for the electron number density measurement for APPJs. [22]

1.3 Nanosecond repetitively pulsed (NRP) pin-to-pin discharges

Another type of atmospheric pressure plasma considered in this work is nanosecond pulsed discharges. In a nanosecond pulsed high-voltage discharge event, voltage can quickly rise above the threshold value for breakdown in the DC case (known as 'over-voltage), allowing the capacitor between electrodes to be 'over-charged' and thus a large amount of energy can be deposited. [23] Pin electrodes are also utilized to enhance the local electric field near electrodes and to further amplify the over-voltage effect. The resulting plasma can have a high concentration of electrons and excited species. During the de-excitation/quenching process of excited species, a large amount of energy is released which heats the gas in a much faster manner than traditional Joule heating, which is known as 'fast gas heating'. [24] [25] A series of nanosecond pulsed discharges with high repetition frequency, also known as nanosecond repetitively pulsed (NRP) discharges, are therefore extensively utilized in the field of aerodynamics and combustion for flow control, shockwave modification, fuel-lean combustion assistance, flame instability mitigation, etc. [9] [10] [11] [14] [38] [39] [41] [42] [44] [43] [45] [48] [49] [50]

NRP discharges thus draw great attention from research groups for fast gas heating as well as the capability to produce certain molecules (for instance, atomic oxygen). NRP pin-to-pin

discharges have been studied under a wide variety of operational conditions: temperature from room temperature to preheated at 1000 K, pressure from a few Torrs to atmospheric pressure, gap distance from hundreds of microns to a few millimeters. Different gases were also tested as the ambient gas for the discharge such as air, nitrogen, argon. Discharge parameters such as temperature and electron number density were measured for the plasmas in the corresponding discharge conditions. OES of the nitrogen 2^{nd} positive system (SPS) is a popular method for vibrational/rotational(=gas) temperature measurement when nitrogen is involved. [26] [27] [28] [29] [30] [31] Electron number density was also measured through various kinds of techniques. For instance, Pai conducted electron number density measurement based on the voltage/current measurements, with which the conductivity and thus electron number density were evaluated. [32] Electron number density was also estimated via OES-based techniques such as Balmer H_α line, Stark broadening in the works. [27] [30] Laser-based techniques such as laser Thomson scattering was also recently proposed to measure electron number density in nanosecond pin-to-pin microdischarges. [33]

1.4 Microwave Rayleigh scattering (MRS)

One particular focus of this work is development of microwave Rayleigh scattering diagnostic techniques and its applications for NRP discharges and DC-driven APPJ in the total electron number/electron number density measurement. It has been proven applicable for many atmospheric pressure microplasma objects and is intended for the electron number measurement for the nanosecond pin-to-pin discharges for the first time.

1.4.1 Theory of MRS

The idea of MRS technique is based on scattering microwave radiation off electrons inside of plasma volume in the quasi-Rayleigh regime. ‘Quasi’ refers to the case that the scattering scheme is equivalent to the classical Rayleigh scattering only when the incident radiation is linearly polarized along the orientation of the plasma channel. In practice, prolonged plasma volume is placed parallel to the linearly polarized microwave and the aspect ratio of plasma volume is high such that the incident microwave electric field is evenly distributed across the entire plasma volume. In this case, electrons in the plasma volume are

performing coherent oscillations in the incident wave and radiating as Hertzian dipole seen from far-field. Since each electron is reacting to the incident microwave independently, the amount of the scattered signal is increasing linearly with the total electron number in the plasma volume, thus can be further utilized for the quantitative determination of total electron number after appropriate calibration procedure of the microwave detecting system.

We consider a plasma volume of high aspect ratio; namely, considerable plasma length in comparison with its diameter, which is quite typical geometry of non-equilibrium plasmas used in practice. However, corrections could be made when plasma shape and/or its orientation with respect to the incident wave are different by introducing depolarization factor k. For example, spherical plasma volume at any orientation with respect to the incident wave yields k=1/3; k=0.5 for elongated plasma filaments when placed perpendicular to the E-filed of the incident wave. When elongated plasma volume is placed parallel to the E-field of the incident wave as applied in MRS technique, k<<1 as shown below in Fig 1-1.

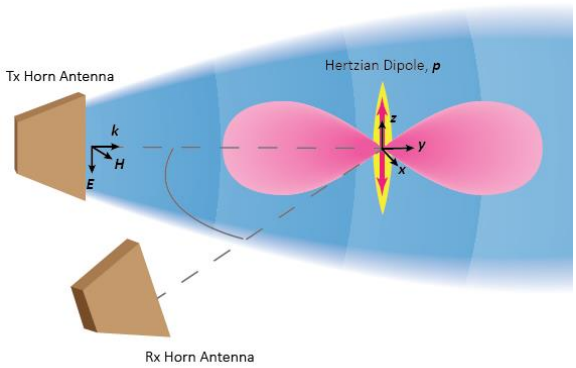

Fig 1-1. Schematics of horns and plasma orientation. E-field is parallel to the page and H-field is oscillating perpendicular to the page.

Let us first consider the electric field induced inside of an elongated scatter as a result of irradiation of incident microwave which is uniformly distributed throughout the channel with an amplitude of E_i. An elongated prolate plasma channel geometry is assumed in this analysis where its length is much greater than its diameter. Furthermore, the plasma's skin depth is considered to be thicker than the plasma channel diameter ($f[\mathrm{GHz}] \leq$

$\frac{2.5}{\sigma[\Omega^{-1}cm^{-1}]\cdot d[mm]^2}$). Thus, the electric field induced inside of the scatterer with dielectric permittivity ε and conductivity σ can be expressed as:

$$\mathbf{E} = \frac{\mathbf{E_i}}{\sqrt{(\mathbf{1+k(\varepsilon-1)})^2+\left(\mathbf{k}\frac{\sigma}{\varepsilon_0\omega}\right)^2}} \qquad (1)$$

where k is the depolarization factor which is much smaller than 1 given plasma shape as a prolate spheroid oriented parallel to the incident E-field. Thus, the amplitude of the electric field induced inside the scatterer can be equated to the incident electric field where $E = E_i$. Furthermore, the incident E-field needs to be experienced by the whole scatterer without any phase shift which requires the flatness of the wave front when hitting the scatterer. Such requirement can be satisfied as: $r > \frac{l^2}{\lambda}$ where r is the distance between the source of radiation and scattered object, l is the length of the scatterer and λ is the wavelength of the incident microwave. In most of the experiments conducted where plasma is < 1 cm and 10 GHz microwave were utilized, r was kept larger than 6 cm which is much greater than $\frac{l^2}{\lambda} \approx 0.3$ cm.

As a result, electrons in the plasma body are experiencing oscillations with an amplitude of $s = \frac{eE_i}{m\nu\,\omega}$. For non-equilibrium plasmas at atmospheric pressures ($n_e<10^{17}$ cm^{-3}), electron collision frequency ν is dominated by the electron-gas collision frequency ν_{eg} such that $s = \frac{eE_i}{m\nu\omega}$. Thus, the dipole moment of the whole plasma channel (p) can be expressed as:

$$\mathbf{p = es\int n(r,z)2\pi rdrdz = esN_e = \frac{e^2}{m\nu}\frac{E_i}{\omega}N_e} \qquad (2)$$

Radiated scattered signal off the plasma volume can be detected by the same horn as the radiating one when placed at far field of microwave. For 10 GHz microwave frequency, the minimum distance between plasma object and detecting horn antenna was determined to be 6 cm to ensure the far-field radiation$\left(\sim\frac{k^2p}{r}\right)$ is dominant over the near-field component $\left(\sim\frac{p}{r^3}\right)$. As a result, the amplitude of the electric field at the location of the detecting horn can be expressed as:

$$\mathbf{E_s = \frac{k^2p}{r} = \frac{e^2}{mc^2\nu}\frac{\omega E_i}{r}N_e} \qquad (3)$$

The output signal of a detection system (U_{out}) thus has relation with the scattered signal off the scatterer E_s as below:

$$\mathbf{U_{out} \propto E_s = \frac{e^2}{mc^2 \nu} \frac{\omega E_i}{r} N_e} \qquad (4)$$

One can see that the MRS system is able to detect the total electron number inside of a plasma volume if the linear coefficient between U_{out} and E_s which is determined by specific microwave system used can be found. Absolute calibration of the MRS system can be conducted using dielectric materials with known physical properties.

Let us now consider applying MRS system onto a prolate scatterer made of dielectric material with volume V and dielectric constant ε. The difference caused by using dielectric rather than plasma is that the total dipole moment induced needs to be re-written as: $p = \varepsilon_0(\varepsilon - 1)E_i V$ and thus:

$$\mathbf{U_{out} \propto E_s = \frac{\varepsilon_0(\varepsilon - 1)}{c^2} \frac{\omega^2 E_i}{r} V} \qquad (5)$$

By combining two types of scatterers, one can express U_{out} as the following:

$$\mathbf{U_{out}} = \begin{cases} \mathbf{A \cdot \frac{e^2}{m\nu} N_e} & \mathbf{-\ for\ plasma} \\ \mathbf{A \cdot V \cdot \varepsilon_0(\varepsilon - 1)\omega} & \mathbf{-\ for\ dielectric\ scatterrer} \end{cases} \qquad (6)$$

where e: electron charge

m: electron mass

ε_0: dielectric permittivity of vacuum

ε: relative permittivity of the dielectric bullet

ω: microwave frequency

ν: collisional frequency

A: proportionality factor

V: volume of the plasma/dielectric scatterer

U_{out}: signal detected by the MRS system

N_e: total number of electrons

n_e: electron number density

Factor A is the proportionality coefficient that's shared by the two cases. It is a coefficient independent of the scatterer properties but solely depends on the experiment's

microwave components and geometric setup. This coefficient is first determined by introducing a dielectric scatterer into the microwave field. Then the calibrated MRS system is utilized for the total electron

1.4.2 Applications of MRS

MRS technique has been successfully utilized in measuring total electron number/electron number density in various kinds of non-equilibrium plasmas at atmospheric pressure: atmospheric pressure plasma jet (APPJ) driven by RF and DC, microdischarges for electrosurgery, laser-induced plasmas by multiphoton ionization (MPI), etc. [22] [34] [35] [36] Helium APPJ was driven by a high voltage source (about 4 kV) operating at a frequency of about 30 kHz. A typical photograph of the plasma jet (approximately 5 cm long) is shown in Fig 1-2 (a) for helium flow rate 5 L/min. The use of the MRS technique allowed conducting temporary-resolved plasma density measurements in a single plasma pulse simultaneously with measurements of other discharge parameters, as shown in Fig 1-2. Temporal evolution of plasma density in the range 10^{12}-10^{13} cm^{-3} was successfully measured in a single exposure. With the help of this unique approach, interesting physics were traced, as described in Ref [37].

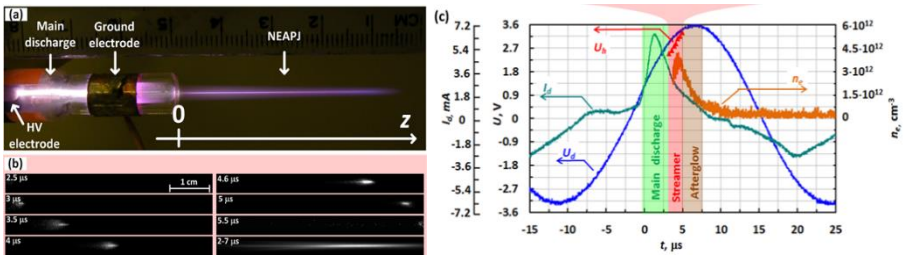

Fig 1-2. MRS measurements of plasma parameters in non-equilibrium atmospheric pressure plasma jet (APPJ). (a-b) Regular and fast photograph of APPJ; (c) Temporal evolution of discharge parameters and plasma density in APPJ measured by MRS diagnostics.

The MRS technique was also applied for studying microdischarges utilized in electrosurgery. [35] Evolution of the plasma parameters in the near-electrode sheaths and in the positive column was measured and analyzed. The electrosurgical system produced an RF-driven discharge with a strongly contracted positive column with current densities reaching 10^3 A/cm^2. The plasma electron density and electrical conductivities in the channel were found

to be 10^{16} cm^{-3} and 1-2 $Ohm^{-1}cm^{-1}$, respectively. The plasma electron density, electrical conductivities, and electric field were measured, allowing studying the physics of the RF-driven discharge utilized in electrosurgery.

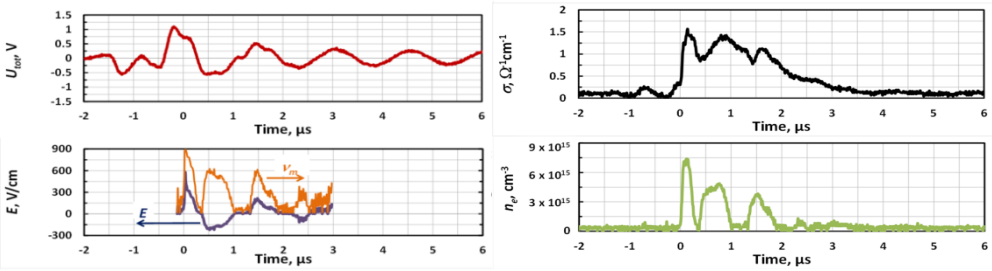

Fig 1-3. Temporal evolution of plasma density, plasma conductivity, and electric field obtained using the MRS technique in electrosurgical discharge.

Very recently, the MRS technique was applied in the first direct measurement of absolute plasma electron numbers generated in a multiphoton ionization (MPI) of air [36]. Subsequently, a cross-section of eight-photon ionization of an oxygen molecule by 800 nm photons was determined: $\sigma_8 = (3.3\pm 0.3) \times 10^{-130}$ $W^{-8}m^{16}s^{-1}$. The motivation for this work was the lack of reliable data on multi-photon ionization cross-sections; with the discovery of MPI more than 50 years ago, spread in the literature values often reaches 2-3 orders of magnitude. The method proposed in that work established a general approach to directly measure and tabulate basic constants of the MPI process for various gases and photon energies.

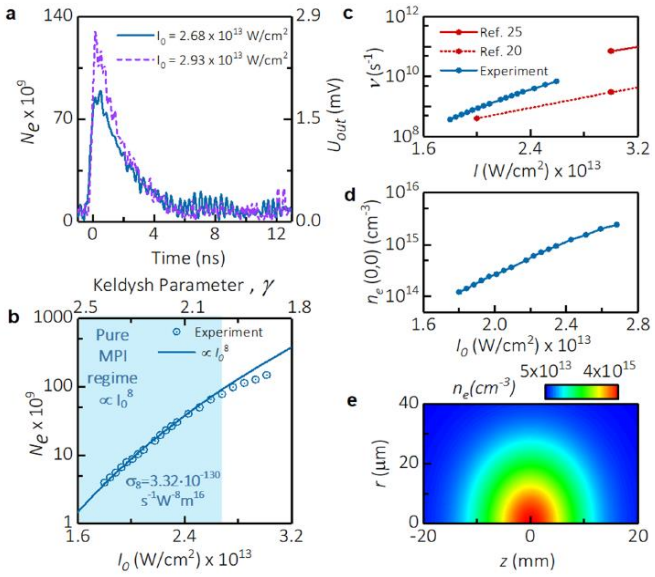

Fig 1-4. Absolute measurements of parameters of fs-laser induced plasmas in air. (a-b) Total number of electrons in laser-induced plasma volume $\mathbf{N_e(t)}$; (c) Photoionization rates; (d-e) Plasma density vs. laser intensity and 2D distribution of the plasma density for $\mathbf{I_0 = 2.68 \times 10^{13}\ W/cm^2}$.

1.5 Motivation

Firstly, traditional APPJ devices driven by time-varying voltage sources (AC, pulsed DC) inevitably have disadvantages including massive EMI, potential danger of electric leakage, as well as high cost of the power supply. On the other hand, DC flashing corona has been extensively studied and exempt from these disadvantages as driven by pure DC voltage. Therefore, attempt to develop DC-driven APPJ is beneficial. This work is thus motivated to develop and study the performance and feasibility of DC-driven APPJ device.

Secondly, for NRP pin-to-pin discharges, as discussed above, reliable diagnostics of NRP microdischarges are not currently available - even though these parameters have critical importance for practical applications and validation of numerical codes. The central motivation was to study the plasma parameters experimentally in NRP discharges with an ultimate goal to advance understanding of the underlying discharge physics. Knowledge of discharge and plasma properties, such as discharge voltage and current, gas temperatures, and electron number densities, is critical for tailoring the NRP discharges to specific applications. Specifically, it was a purpose of this work to generate a comprehensive dataset that contains the parameters relevant for

experiments and simulations of flow effects induced by the NRP discharges, such as temporal evolution of gas temperature and electron number density in the interelectrode space.

One particularly important parameter of both plasma objects mentioned above is total electron number/electron number density. However, currently available methods are all still in their infancy as discussed above. On the other hand, microwave Rayleigh scattering has been proven recently to be a reliable diagnostic for a broad range of miniature plasma objects at atmospheric conditions. Therefore, this work has also been motivated by the idea to develop a methodology of microwave Rayleigh scattering application for both APPJ and NRP discharges at atmospheric conditions.

1.6 Objectives

The objectives in this work can be divided into two groups: studying the NRP pin-to-pin discharges and studying the DC-driven APPJ. The NRP discharge related goals are detailed below:

1. **Develop methodology of MRS application for NRP discharges.** This includes the construction of MRS homodyne detection system and optimizing the system's sensitivity. The system is aimed to enable precise positioning of microwave horn antennas in all directions. Correct accounting for the effect of proximity of surrounding structures such as the electrodes and electrode holder on the calibration procedure is targeted. In addition, the local gas density will be measured by Laser Rayleigh scattering to identify collisional frequency required for interpretation of MRS data.
2. **Measure dynamics of plasma parameters in NRP discharges.** This includes measurement of total electron number (by combination of MRS and LRS), rotational and vibrational temperature (by OES), gas density (by LRS) for various discharge conditions such as different gap distances, energy deposition per pulse, and repetition frequencies. This work is also aimed to measure the plasma parameters in different discharge regimes (corona and spark) and transition between the regimes.

The objectives related to the development and study of DC-driven APPJs are:

1. **Develop helium DC-driven APPJ device.** This includes the machining and assembling of raw materials for the construction of APPJ device, adjusting geometries and other

parameters such as helium flow rate/voltage level to optimize the outcome plasma jet in terms of brightness and length.

2. **Investigate the enhancement effect of dielectric enclosure on the intensity of flashing corona.** This focuses on the discharge phenomenon itself, where an enhanced flashing corona was realized when brought into a semi-closed system covered by dielectric material. Parameters studied were distance between ground and HV electrode, HV voltage level, which both have an effect on the intensity of flashing corona in terms of peak current and repetition frequency.
3. **Measurement of discharge parameters for DC-driven APPJ.** This includes the implementation of MRS technique for the electron number measurement, and temperature measurement by OES.

1.7 Outline

Chapter 2 presents the development of the diagnostic techniques for the study of NRP discharges. Firstly, the validity of the application of MRS technique on the pin2pin ns-discharges is confirmed in Chapter 2.1. Secondly, a noble technique for temperature measurement utilizing nanosecond probing pulse is proposed and presented in Chapter 2.2. Thirdly, a combined diagnostic technique of microwave and laser Rayleigh scattering is proposed in Chapter 2.3 to re-adjust the microwave scattering measurement of microplasmas with which local gas density varies due to extensive pulse energy input.

Experimental study of the ns-discharges was described in Chapter 3. Chapter 3.1 focuses on the diagnostics of single pulsed ns-discharges without the memory effect, in which different discharge regimes are defined (spark and corona), effect of energy input, gap distance on the discharge parameters is also investigated. In Chapter 3.2, ns-discharges at high repetition frequencies are discussed. Various repetition frequencies of NRP discharges were chosen to investigate the memory effect accumulated during a burst of ns-discharges.

In Chapter 4, experimental study of DC-driven APPJ operating at atmospheric conditions is conducted. The idea of a pure DC-driven helium plasma gun was proposed and presented in Chapter 4.1. In Chapter 4.2, the principle of device operation is considered and the effect of enhancement by dielectric enclosure is discussed. Lastly, the DC-driven helium plasma jet is

further investigated by MRS and OES techniques for the electron number and temperature measurements.

Chapter 5 presents conclusions and recommendations for future work.

2 DEVELOPMENT OF DIAGNOSTIC TECHNUQES FOR NRP PIN-TO-PIN DISCHARGES

2.1 Time-revolved measurements of electron density in nanosecond pulsed plasmas using microwave scattering

Xingxing Wang, Paul Stockett, Ravichandra Jagannath, Sally Bane and Alexey Shashurin
Purdue University, School of Aeronautics and Astronautics, West Lafayette, IN 47907, USA

Portions of this chapter have previously been published in Plasma Sources Sci. Technol.
DOI: 10.1088/1361-6595/aacc06

2.1.1 Abstract

In this work, microwave scattering was utilized to measure the electron number density produced in a nanosecond-long high-voltage breakdown of air between two electrodes in a pin-to-pin configuration. The approach allows tracing the absolute electron number in the plasma volume during the high-voltage pulse and the plasma decay for wide range of plasma and discharge parameters. Electron number density decayed on the timescale of about several μs governed by plasma-chemical processes including dissociative recombination, three-body attachment and formation of cluster ions.

2.1.2 Introduction

Atmospheric pressure plasmas have unique characteristics which can be leveraged for a wide range of applications, including plasma-assisted ignition and combustion, aerodynamic flow control, medicine and environment, nanotechnology, and materials processing [1]. Detailed diagnostics of atmospheric pressure plasmas generated under various conditions (electrode configuration, discharge-driving high voltage waveform, background gas composition and temperature, etc.) remain a critical challenge. In recent years, nanosecond repetitively pulsed (NRP) plasma discharges have attracted great interest as an efficient method for creation of non-equilibrium plasmas at high pressures. The very large voltage rise over very short time scales and subsequent strong electric field accelerates electrons to very high energies, leading to efficient production of reactive and ionized species. Pulsing of these discharges at high repetition rates results in accumulation of metastable and active species. These plasmas are especially of interest

in combustion and aerodynamic flow control applications. In the combustion field, NRP plasmas have been used to increase flame speed [38] [39], enhance flame stabilization at low fuel/oxidizer ratios [40] [9] [10] [11], and mitigate combustion instability [41] [42] [43] [44]. For aerodynamic flow control, surface dielectric barrier discharge (DBD) plasmas driven by NRP discharges has been explored for controlling boundary layers at realistic flight conditions [45] [14], and for shock wave modification in supersonic flow [46] [47]. NRP spark plasmas have also been shown to be effective at inducing flow instabilities by generating pressure waves [48] [49] [50].

High-resolution measurements of the temporal evolution of NRP plasmas are critical for understanding the discharge physics and ultimately for designing plasma sources tailored to specific applications. Conventional diagnostics of NRP discharges include optical emission spectroscopy (OES), Stark broadening, fast photography, measurements of voltage and current waveforms, etc. [51] [28] [52] [29] [30]. One of the most important characteristics of NRP plasmas is electron number density. However, direct experimental data available on electron number density and its evolution in time is limited and the measurement techniques used often have some significant limitations.

Electron density has been measured by several groups utilizing OES. Rusterholtz et al. estimated the peak electron density of NRP spark plasma in preheated (1000 K) air to be in the range of 10^{15} cm^{-3} using spectra of the Balmer H_α line [51]. Van der Horst and co-workers performed similar measurements in room temperature air and found the peak electron density to be approximately $3 \cdot 10^{18}$ cm^{-3} [28]. In these studies, this method is restricted to the time range from 3-11 ns due to masking of the H_α line by N_2(B-A) emission after 11 ns and requires the background N_2(B-A) spectrum to be accurately determined and subtracted. Another method for measuring electron density from OES spectra is to use Stark broadening of the atomic nitrogen line and H_α/H_β. This method was used to measure electron density of NRP plasmas in various kinds of gas mixtures, with resulting electron density was in the range of 10^{15} - 10^{18} cm^{-3} [29] [30]. One potential issue, however, is that Stark broadening sensitivity is limited for electron densities > 10^{15} cm^{-3} [30]. Furthermore, the interpretation of the broadening of the spectrum can be problematic due to contributions from several competing mechanisms to the line broadening.

In several detailed studies on NRP plasmas in preheated (1000 K) air with a pin-to-pin electrode configuration, Pai et al. identified three different plasma discharge regimes: corona, glow, and spark [53] [54] [32]. These regimes are categorized by the energy deposited per pulse: <10 μJ

for corona, 10-100 μJ for diffuse or glow, and >100 μJ for spark. The resulting gas heating is <200 K for the corona and glow regimes [53] and in the range of 2000-4000 K for the spark regime [54]. The electron density in the spark mode was estimated to be in the range of $3{\cdot}10^{13}$ to $3{\cdot}10^{15}$ cm^{-3} [32]. These values of electron density were estimated using measurements of the discharge voltage (V_d) and current (I_d). First, the voltage and current were used to calculate the equivalent resistance of the plasma column as $R = \frac{V_d}{I_d}$. Then, the plasma conductivity was determined based on the visually observed length (L) and cross-sectional area (S) of the plasma column as $\sigma = \frac{L}{R \cdot S}$. The plasma density was then calculated as $n_e = \frac{\sigma \cdot \nu \cdot m}{e^2}$ where ν is the electron-gas collision frequency, and m and e are the electron mass and charge, respectively. However, this approach to estimating electron density has some significant limitations. First, the voltage drop in the plasma column is different from V_d (especially in the case of low-V_d arc-type discharges) due to the presence of near electrode sheaths [55]. This causes overestimation of plasma column resistance and thus, underestimation of conductivity and plasma density. Second, the experimental data presented by the authors is not consistent with their assumption that the plasma acts as a purely resistive load. During the discharge, the times of zero-crossings of the V_d and I_d waveforms are shifted with respect to each other (e.g. see the figure 6 in Ref. [32] at $t \approx$10 ns where $V_d \approx$0 while $I_d \approx$30 A). This offset in time between the discharge voltage and current clearly indicates the presence of a reactive part in the plasma load impedance and causes unreasonable estimation of the plasma density near the moment where $V_d \approx$0 if method proposed by the authors' is used since $n_e \propto \sigma \propto \frac{1}{R} \propto \frac{I_d}{V_d} \to \infty$.

Thus, reliable diagnostics to measure the electron number density in the NRP plasmas are not available even though this parameter has critical importance for practical applications and validation of numerical codes. In this paper, a method for direct measurement of electron number density in the plasma column of the NRP discharge in a pin-to-pin electrode configuration by means of Rayleigh microwave scattering (RMS) is presented. This method was recently proposed [56] [34] and successfully applied for measurements in various types of atmospheric pressure microplasmas [22] [57] [36]. The idea of the RMS approach is scattering of microwave radiation off the plasma volume in the quasi-Rayleigh regime, when the prolonged plasma volume is oriented along the linearly polarized microwaves and the plasma diameter is small compared to

the spatial scale of the microwave field change, so that the incident microwave electric field is distributed uniformly across the entire plasma volume

2.1.3 Experimental setup

The plasma was generated between two pointed-tip tungsten electrodes separated by an inter-electrode gap distance *L*. In this work, three different gap distances were used: *L* = 2, 5, and 8 mm. Capacitance of the electrode geometry was measured to be around C=3.5 pF (by measuring electrode voltage and current waveform without plasma generation). The plasma was produced using high voltage pulses with pulse duration (FWHM) of 55 ns generated by a nanosecond high voltage pulser (Eagle Harbor NSP-3300-20-F). Short series of pulses (up to 10 pulses 1 ms apart) were used to ensure the plasma creation. The peak voltage applied to the pin-to-pin electrodes was approximately 26 kV. The voltage between the electrodes was measured by two high voltage probes (Tektronix P6015A) connected to the corresponding electrodes with grounds of both probes connected together to obtain a differential measurement to maintain the pulser output floating. Thus, the actual voltage applied to the electrodes was calculated as the difference between the measurements of the two voltage probes. The waveform of the voltage pulse sent to the electrodes with no breakdown of the gap is shown in Fig 2-1. Discharge current was measured by a high-bandwidth current transformer (Bergoz FCT-028-0.5-WB) on the positive voltage line. Time resolved images were taken by an ICCD camera (Princeton Instrument PI-MAX 1024i).

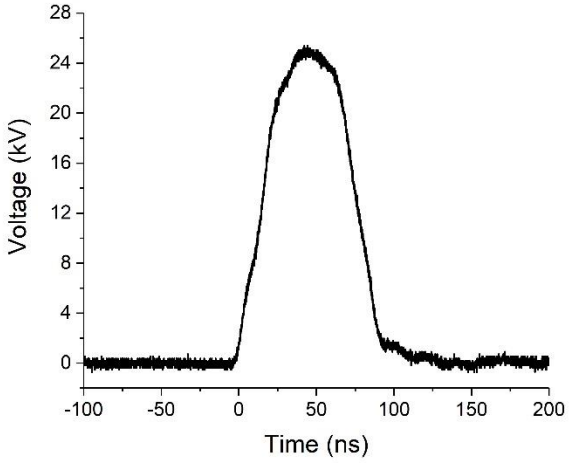

Fig 2-1. Voltage pulse applied to the electrodes without breakdown of the electrode gap.

A Rayleigh Microwave Scattering (RMS) system was constructed for measurement of the time-resolved plasma electron density. The RMS system utilizes a homodyne detection scheme for measurement of microwave signal scattered from the plasma volume. The system can be used to determine the total number of electrons inside of the plasma volume by analyzing the scattering of linearly polarized microwave radiation from the collinearly-oriented plasma channel. A schematic of the RMS system and its location in the overall experimental setup are shown in Fig 2-2. The microwave signal is radiated onto the testing object through a 10 dB horn antenna. The detected signal is received by another horn antenna and processed by an I/Q mixer outputting two signals: *I* and *Q*. The final output signal can be expressed as $U_{out} = \sqrt{I^2 + Q^2}$. The frequency of the microwave was set to be 10.9 GHz which minimized the noise level produced by the circuitry and surroundings.

Absolute calibration of the RMS system is accomplished using dielectric scatterers with known physical properties. A Teflon bullet (ε = 2.1) in the shape of a cylinder with a diameter of 0.32 cm and length of 1 cm was used in this work. The output U_{out} of the RMS system can be related to properties of a dielectric scatterer and plasma as follows [34]:

$$\boldsymbol{U_{out}} = \begin{cases} \boldsymbol{A\frac{e^2}{mv}N_e,} & \boldsymbol{for\ plasma} \\ \boldsymbol{AV\varepsilon_0(\varepsilon - 1)\omega,} & \boldsymbol{for\ dielectric\ scatterers} \end{cases} \qquad (1)$$

where *A* is the proportionality coefficient, *e* is the electron charge, *v* is the electron-gas collision frequency which was estimated to be $1.46 \cdot 10^{12}$ sec^{-1} in this case [34] [58], *V* is the volume of the dielectric scatterer, ε_0 is the vacuum permittivity, ε is the relative permittivity of the dielectric material and ω is the angular frequency of the microwaves. Using the output measured for the Teflon bullet in the bottom relation in Eq. 1 the proportionality factor *A* was found to be 85.3 $kV\Omega/m^2$. As a result, the top relation of Eqn 1 can be re-written as:

$$\boldsymbol{N_e} = \frac{\boldsymbol{U_{out}[V]}}{\boldsymbol{1.643 \cdot 10^{-15}}} \qquad (2)$$

and the total number of electrons can be calculated directly using the RMS output signal. The distance between both the radiating and receiving horn antennae and the testing object was kept at 6 cm to ensure flatness of the microwave front when hitting the plasma and to maintain the

scattered signal within the Rayleigh scattering regime. More details on the RMS system can be found in [36].

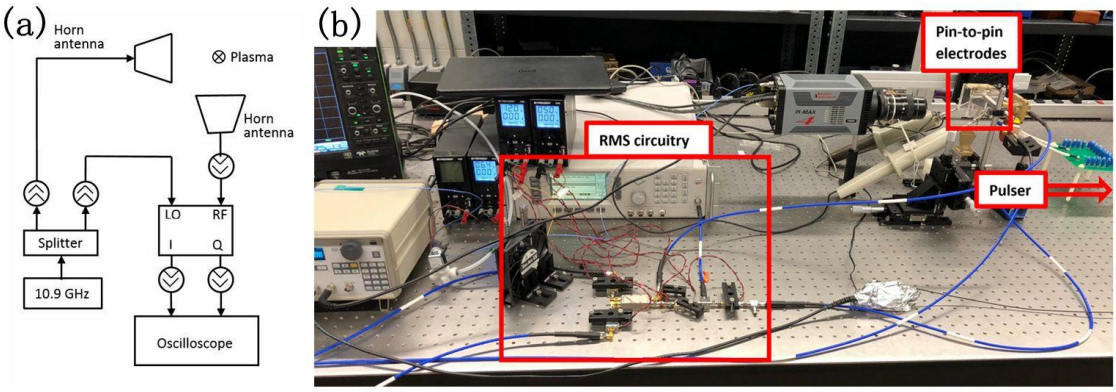

Fig 2-2. (a) Schematic of the RMS system. (b) Entire experimental setup.

2.1.4 Results and Discussion

Fig 2-3 shows the images of the NRP discharge for three different gap distances at different times after the breakdown (each image was taken at a different breakdown event). Analysis of the intensity distribution of ICCD images of the plasma column indicated that the plasma diameter was about 330 μm for all experimental conditions. Then, the volume of the plasma column was determined by assuming a cylindrical shape with height equal to gap distance L and diameter of 330 μm as $V_0[cm^3] = 8.6 \cdot 10^{-5} \cdot L[mm]$ and thus spatially averaged electron number density n_e can be calculated as: $n_e = \frac{N_e}{V_0}$

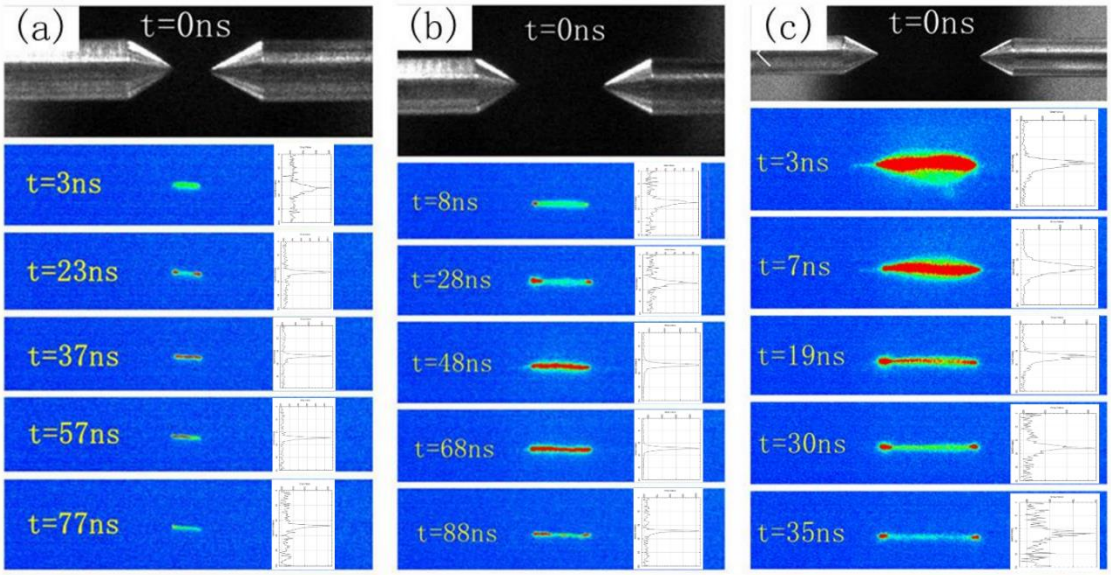

Fig 2-3. Images of an NRP discharge plasma in a pin-to-pin electrode configuration with varying gap distances L at different moments of time after breakdown. The distribution of intensities for each case is plotted on the right-hand side of each ICCD image. (a) L = 2mm; (b) L = 5mm; (c) L = 8 mm. Exposure time = 3 ns.

The temporal evolution of the average electron density n_e determined from RMS measurements and the discharge voltage and current L = 5 mm are plotted in Fig 2-4. Fig 2-4(a) shows the temporal evolution of n_e on the microsecond timescale. The density reached its peak value of about $7 \cdot 10^{15}$ cm^{-3} at the time of breakdown and then decayed in approximately 2 μs after the discharge initiation. Fig 2-4(b) shows the evolution of N_e on a sub-microsecond timescale plotted along with the discharge voltage and current waveforms. Prior to electrical breakdown between the electrodes, the applied voltage increased until it reached the threshold value for breakdown at about 15 kV. Then the voltage rapidly decreased and current increased due to the breakdown and formation of a highly conductive plasma channel between the electrodes. Note, I_d measurements show the discharge current only (obtained by subtraction of the displacement current from the total current measured by the current probe). The current reached a peak value of 15 A immediately after the breakdown and dropped down to zero at the end of the driving voltage pulse. Note that measurements of V_d are presented for times before the breakdown only since limited bandwidth of the voltage probe (75 MHz) does not allow it to realistically capture the rapid drop of the voltage near the breakdown event. One can also see that n_e decayed at a much slower rate compared to I_d. This indicates that plasma lifetime extends significantly longer than the

duration of the discharge-driving pulse. The plasma decay is governed by the number of competing plasma-chemical processes including dissociative recombination, three-body attachment and formation of cluster ions [32] [59].

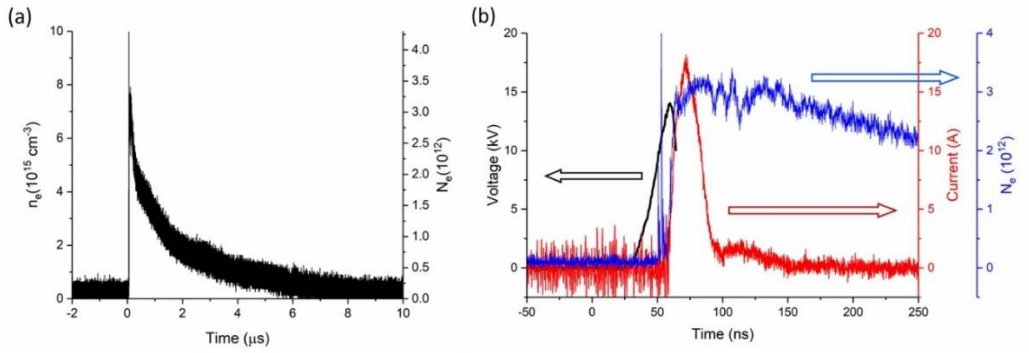

Fig 2-4. (a) Temporal evolution of ne and Ne on the μs time scale. (b) Temporal evolution of voltage, current, and Ne on the ns time scale.

Fig 2-5 shows the relationship between the peak value of electron density and total number of electrons in plasma volume versus gap distance L. As L increases, n_e and N_e decreases, which can be possibly explained by a transition between discharge regimes similar to that discussed in Ref. [53].

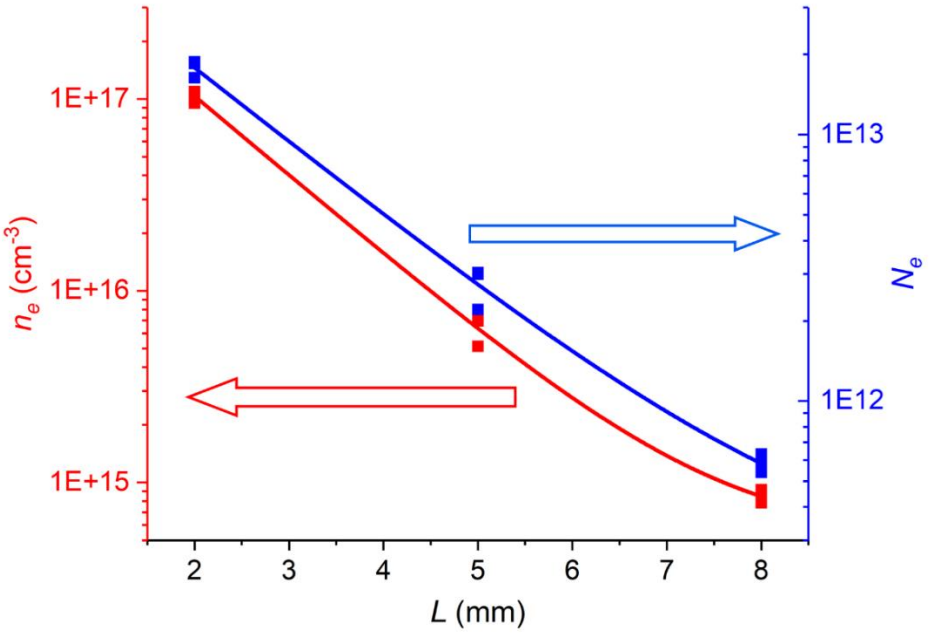

Fig 2-5. peak value of ne and Ne vs gap distance L

2.1.5 Conclusion

To conclude, in this work, time-resolved measurement of electron number density in the plasma produced by nanosecond repetitive HV pulses using Rayleigh Microwave Scattering was demonstrated. The peak electron number density increased from $8 \cdot 10^{14}$ to $1 \cdot 10^{17}$ cm^{-3} with value with decrease of inter-electrode gap distance from 8 to 2 mm (N_e increased from $5 \cdot 10^{11}$ to $2 \cdot 10^{13}$, respectively). Efforts to determine the effect of pulse parameters and electrode geometry on the plasma regime and characteristics using RMS measurements are currently underway.

2.2 Gas thermometry by optical emission spectroscopy enhanced with probing nanosecond plasma pulse

Xingxing Wang, Alexey Shashurin
Purdue University, School of Aeronautics and Astronautics, West Lafayette, IN 47907, USA

Portions of this chapter have previously been published in AIAA Journal
DOI: 10.2514/1.J059511

2.2.1 Introduction

In recent years, Nanosecond Repetitive Pulsed (NRP) discharges have been found of great use for combustion related applications such as increasing flame speed [38] [39], enhancing flame stabilization at low fuel/oxidizer ratio [52] [9] [10] [11], and mitigating combustion instability [41] [42] [44] [43]. In addition, NRP discharges have been applied for aerodynamic flow controls. Surface dielectric barrier discharge (DBD) plasmas driven by NRP discharges have been explored for controlling boundary layers at realistic flight conditions [45] [14], and for shock wave modification in supersonic flow [60] [61]. NRP spark plasmas have also been shown to be effective at inducing flow instabilities by generating pressure waves [48] [49] [50].

Comprehensive temporally resolved measurements of the NRP plasma properties are critical for understanding the nature of the plasmas and practical applications. Two of the most important parameters of theses discharges are total electron number/electron number density and rotational/vibrational temperatures. Electron number density is a measure of the total electron produced during discharge which implies the amount of reactive species produced. In previous works, studies of the total electron numbers of the plasma produced in a high-voltage NRP discharge in a pin-to-pin configuration were conducted at atmospheric pressure and room

temperature [62] [63] where a HV pulses with peak value of 26 kV and pulse width of 100 ns were applied to the pin electrodes at a frequency of 1 kHz. The total electron number was measured by Rayleigh Microwave Scattering (RMS) technique [22]. It was found that for the spark discharge, the amount of total electron produced ranged from $2.4 \cdot 10^{12}$ to $1.2 \cdot 10^{13}$ and spatially-averaged electron number density from $0.9 \cdot 10^{14}$ to $1.0 \cdot 10^{17}$ cm^{-3} respectively, when the gap distance between the pin electrodes was changed from 3 mm to 9 mm [63].

Rotational temperature is often used as a measure of bulk gas temperature for the NRP discharges at atmospheric pressure based on fast rotational-translational relaxation and predominant creation of $N_2(C)$ by electron-impact excitation of $N_2(X)$ [64] [65] [66] [67] [68]. Vibrational temperatures are typically substantially higher than the rotational which is indicative of high degree non-equilibrium inherent to the NRP discharges. In our previous work, both rotational and vibrational temperatures of the NRP plasmas were measured with 5 ns temporal resolution [62]. However, these measurements were limited to only first approximately 20 ns of the discharge due to the following reason. Rotational and vibrational temperatures were determined from the measurements of the nitrogen second positive system with $\Delta v = -2$ based on the classical Optical Emission Spectroscopy (OES) approach to fit that measured spectra with the synthetic one generated numerically. It was observed that the second positive system of nitrogen only existed for the first 20 ns of the discharge event and, therefore, rotational and vibrational temperatures were only determined during that initial stage of the discharge. Afterwards, the emission of the N_2 2^{nd} positive system disappeared due to the decrease of the reduced field *E/N* below the favorable range of about 10^{-16}-10^{-15} $V \cdot cm^2$ as the dense plasma channel was forming between the discharge electrodes [18].

Therefore, measurements of gas temperature in atmospheric pressure NRP discharges using OES technique are limited to only initial 20 ns after the breakdown (several previous works have evaluated OES measurements on later times, but have not proven that these measurements provide actual unperturbed values of the gas temperature [67] [68]). However, gas temperature data on a significantly longer time scale than that initial time period (microseconds to milliseconds after the breakdown) are crucial for analysis of flow induced effects by the NRP actuators and their further applications in combustion systems [69]. This obvious research gap has created the initial motivation for the current work to expand applicability of the simple OES approach beyond the initial 20 ns after the breakdown. This initial motivation had expanded into the broader question

of how standard OES procedure can be utilized for the temporally-resolved gas thermometry in general even if the gas under test is not emitting photons required for the spectra collection.

In this work, we present a novel method of air temperature measurements with 5 ns temporal resolution which can be used for a great variety of applications as a thermometer, e.g., in combustion. The method is based on the classical rotational/vibrational temperature measurements utilizing optical emission spectroscopy of the 2^{nd} positive system of nitrogen used in conjunction with probing nanosecond plasma pulse. The probing pulse is used in order to excite the emission of the 2^{nd} positive system at the desired moment of time. We demonstrate that it is physically feasible to establish pulsing probe parameters so that gas heating by the probing pulse itself is negligible, while the emission of the 2^{nd} positive system of nitrogen is sufficient to conduct the OES measurements. The spectrum is acquired during first 5 ns after the probing pulse initiation in order to eliminate the effect of the probing pulse gas heating on the measured temperature. The method is further applied in this work to conduct the gas temperature measurements in the wake of atmospheric NRP discharge from the moment of discharge initiation to 5 ms after the breakdown.

2.2.2 Methods and Equipment

The nanosecond plasma pulses were generated between two pin tungsten electrodes. Each tungsten electrode had a tip diameter of approximately 200 μm and was connected to one output arm of the Eagle Harbor nanosecond pulse generator (NSP-3300-20-F) where the gap distance between the electrodes *d* was kept at 5 mm. A pulse with peak voltage value of 26 kV and width of 120 ns was used. The pulse generator was operating in the differential mode such that each output arm of the pulser generated a ns-pulse of the same amplitude but opposite polarity with respect to the ground. The voltage was measured by two 30 kV rated high voltage probes (Tektronix P6015A) connected to each electrode and the actual voltage applied to the electrodes was calculated as the difference between two probe readings. The current was measured by a current transformer probe (Bergoz FCT-028-0.5-WB) hooked on the positive arm of the pulse generator.

Optical Emission Spectroscopy system was implemented as shown in Fig 2-6. Light emission signal was first collected by a parabolic mirror system (with focal length of 4 inches), projected 1:1 onto the input plane of an optic fiber, and then transferred to a spectrometer (Princeton Instrument Acton SpectraPro SP-2750). The converted spectrum data was recorded by

an ICCD camera (Princeton Instrument PI-MAX 1024i) mounted onto the spectrometer. Nitrogen second positive system (C→B) with spectral band of $\Delta\nu = \nu' - \nu'' = -2$ was captured for further fitting with the synthetic spectra simulated in SPECAIR.

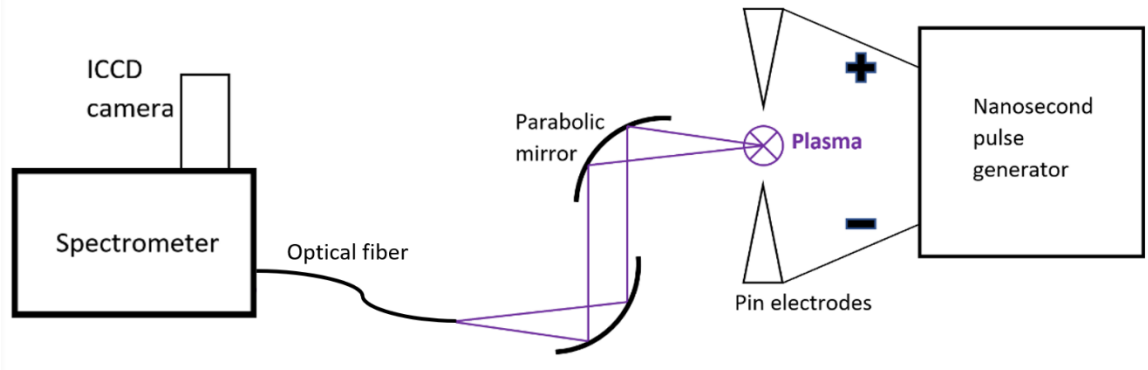

Fig 2-6. Schematics of the OES measurement system

For the temperature measurements in the initial 20 ns of the discharge, the procedure was the same as in our previous work [62]. Specifically, the gate width of the ICCD camera was set at 5 ns and a time step at 5 ns. Approximately 50-200 samples were accumulated to achieve an adequate signal-to-noise ratio for further spectrum fitting depending on the intensity of the emission. For the temperature measurements after the NRP discharge, a second HV probing pulse was applied to the electrodes with the controlled delay in order to initiate additional breakdown and re-ignite the emission of the 2nd positive system of N_2. The spectrum at the very first 5 ns of the probing pulse was recorded in order to eliminate the effect of gas heating due to the probing pulse on the measured temperature (see details below). 500 spectrum samples were accumulated on the ICCD chip to improve the signal-to-noise ratio of the spectrum. The time interval between the NRP discharge and the probing pulse was chosen to be 20, 50, 100, 200, 500, 1000, 2000 and 5000 μs (20 μs was the earliest time at which we were able to create the probing breakdown with currently available HV pulse generator). The sample waveform illustrating NRP discharge pulse and subsequent probing pulse is shown below in Fig 2-7 with delay Δt = 20 μs. The NRP discharges operated at the repetition frequency of 1 Hz to ensure the temperature relaxation to the room temperature prior to the each next NRP pulse.

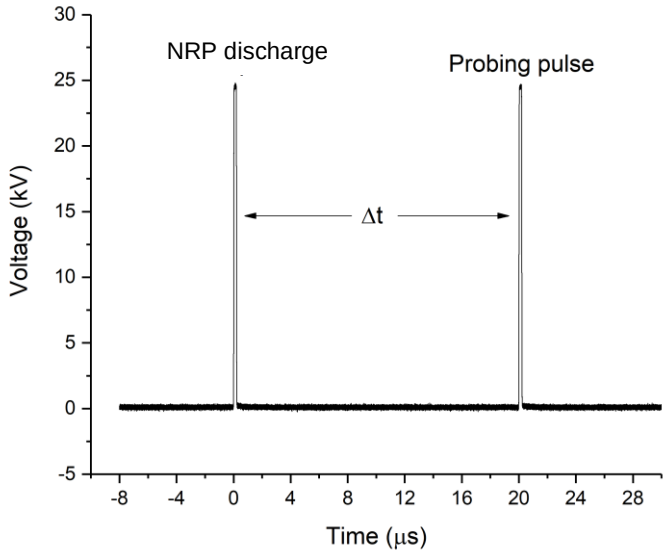

Fig 2-7. Sample waveform illustrating NRP discharge pulse and subsequent probing pulse applied with delay Δt = 20 μs.

2.2.3 Results and Discussion

Firstly, the temporal evolution of *V, I, T_{rot}* and *T_{vib}* for the initial 20 ns of the NRP discharge has been measured as shown in Fig 2-8. One can see the breakdown voltage (approx. 17 kV) was reached at *t*=35 ns and followed by the discharge current peak of 22 A. Rotational and vibrational temperatures were measured within the time interval of *t* =35-55 ns with 5 ns temporal resolution using OES technique. Within this time interval, *T_{rot}* increases from 300 to 600 K, and *T_{vib}* increases from 3900 K to 5020 K. It was observed that 2nd positive system of N_2 presented in the emitted spectrum during only first 20 ns after the breakdown and disappeared thereafter. The example of the spectra obtained in the first 20 ns after the breakdown (*t* = 35-55 ns) and subsequent 20 ns (*t* = 55-75 ns) are shown in Fig 2-9. One can see that multiple spectral bands including the 2nd positive system are clearly detectable only in the spectrum acquired in in the first 20 ns. Therefore, *T_{rot}* and *T_{vib}* were determined by OES during the time interval *t* = 35-55 ns only. Vanishing of the N_2 2nd positive system in the emission spectrum can be explained by the quenching of the corresponding excited vibrational and rotational levels and absence of the new excitations. Indeed, according to Raizer, the reduced electric field $E/N \geq 10^{-15}$ V·cm^{-2} is required for the efficient pumping of the electronic excitations, vibrations and ionization of O_2 and N_2, while efficiency of these transitions decreases for the lower reduced fields. [18] Rough estimations of the reduced electric field based

on the discharge voltage experimental data shown in Fig 2-8 confirms that the reduced electric field was about 10^{-15} V·cm^{-2} for the initial 20 ns after the breakdown and then dropped significantly due to creation of highly-conductive spark channel between the electrodes and associated decrease of the discharge voltage.

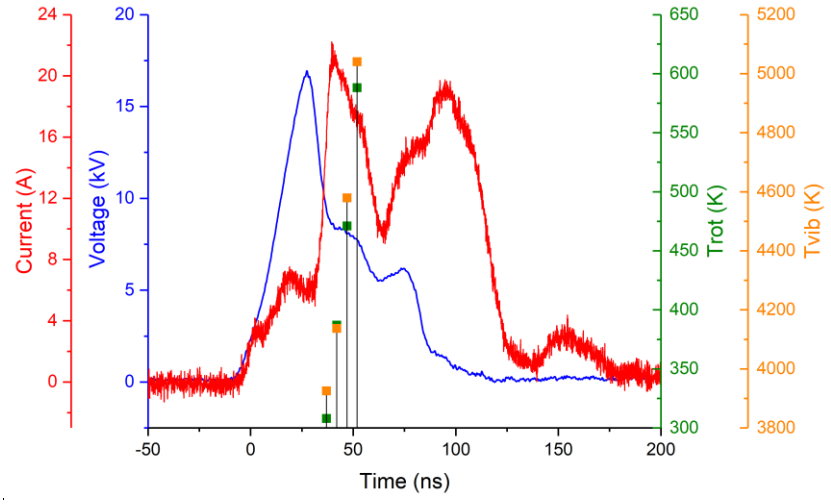

Fig 2-8. Temporal evolution of V, I, T_{rot} and T_{vib} for NRP discharge

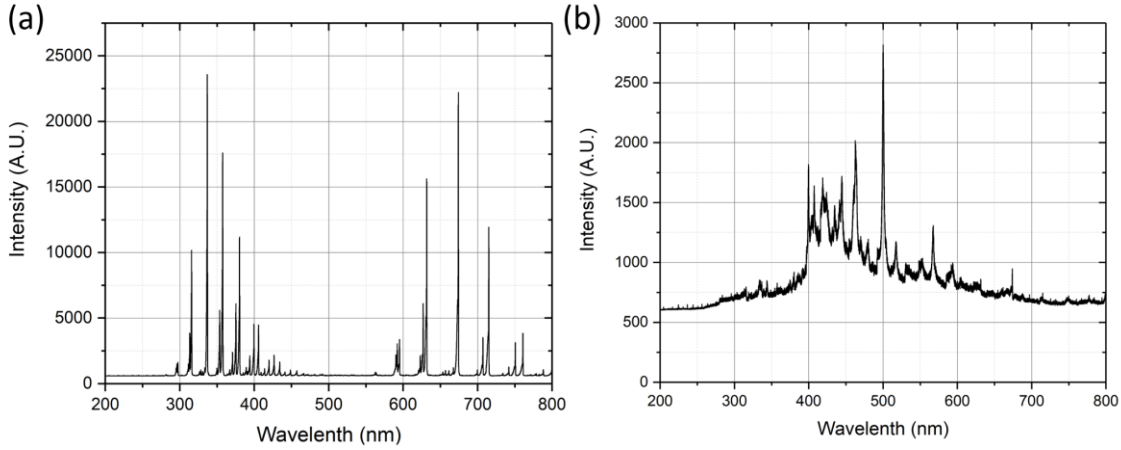

Fig 2-9. Full spectrum from 200 nm to 800 nm of the light emission of the discharge. (a) initial 20 ns after the breakdown, (b) 20-40 ns after the breakdown.

Fig 2-10 shows typical voltage/current waveforms of the probing pulse applied with delay of Δt=20 μs after the NRP discharge. Application of the probing pulse caused additional breakdown of the gas and "re-illumination" of the 2nd positive system in the spectrum. The shaded

area represents the time window (5 ns) when the spectrum was acquired by the spectrometer. Note, *V/I* waveforms look very differently from that of the NRP pulse shown in Fig 2-8 due to the better impedance matching with the pulser caused by presence of decaying the plasma and heated gas in the gap. As the delay time Δt was increased to several ms, shape of the *V/I* waveforms became similar to that shown in Fig 2-8 due to the completion of the plasma decay.

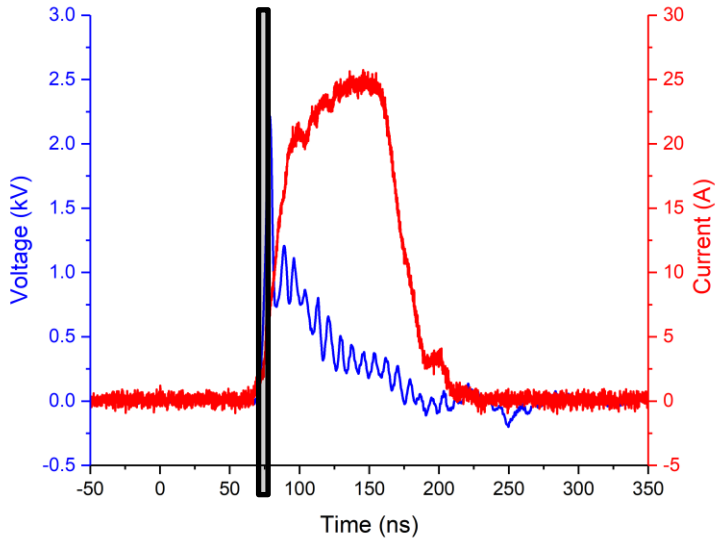

Fig 2-10. Voltage/current waveform of the probing pulse with $\Delta t = 20$ μs. The shaded square represents the duration when the ICCD camera gate was open. The waveform of the probing pulse was different from that of the NRP discharge pulse in Fig 3 due to the impedance change between the electrodes in the wake of the NRP discharge.

The gas temperature evolution after the NRP discharge was determined using this method for probing pulse delays 20, 50, 100, 200, 500, 1000, 2000 and 5000 μs as shown in Fig 2-11. The error bars correspond to the temperature range required to keep the SPECAIR-simulated spectra within the limits of the experimental data spread. Time zero implies the NRP discharge event (same as in Fig 2-8). One can see from the Fig 2-11 that the gas temperature was measured to be approximately 2600 K at 20 μs after the NRP discharge, decreased to around 650 K at 500 μs and finally reached 300 K at 5 ms after the discharge.

It is critical for the method considered here to confirm that gas heating due to the probing pulse itself is negligible as long as the spectrum of the N_2 2^{nd} positive system is acquired during the first 5 ns of the probing pulse only. Several previous works have assumed that heating by the

probing pulse during first several ns after its onset is negligible [67] [25]. However, this is not a universal fact and requires further proof as the temperature rise is clearly depending on the probing pulse parameters (amplitude, *dV/dt*) and substantial rise of the rotational temperature can be observed even during the first 5 ns period of the pulse [68]. Therefore, probing pulse parameters should be customized for each specific experiment to make sure that the heating by the probing pulse is negligible, while the emission of the 2nd positive system of nitrogen is sufficient to conduct the OES measurements. In this work, the temperature measured at first 5 ns of the NRP discharge and at 5 ms after it agrees with the true unperturbed room temperature of 300 K. Thus, it can be concluded that gas heating by the specific probing pulse used in this work is negligible on the timescale of 5 ns. Note, the total electrical energy deposition during first 5 ns of the probing pulse was about 4-5 times smaller if the probing pulse was applied with 20 μs delay rather than one applied with 5 ms delay (see *V/I* waveforms shown in Fig 2-8 and Fig 2-10); specifically, 0.06 mJ for Δt = 20 μs and 2.6 mJ for Δt = 5 ms. And, therefore, the gas heating by the probing pulse applied with 20 □s delay is expected to be even less pronounced.

The approach proposed here can be utilized for the temporally-resolved gas thermometry in various applications. Specifically, it can be used for combustion thermometry in various gas mixtures and pressure ranges in case Boltzmann distribution of rotational levels in $N_2(C)$ state can be experimentally confirmed. Proposed method is particularly fitted for the temperature measurements in plasma-assisted ignition/combustion systems which are already equipped with electrodes that can be used for application of the probing pulses. Full spectra of other applications, impact, and potential limitations of the current approach are subject of future works. In comparison with traditional means of temperature measurement such as thermocouple, the proposed method is characterized by better temporal resolution (about 5 ns). Spatial resolution of the temperature measurements (down to about 1 mm) can be achieved by appropriate positioning of the electrodes and choosing the gap size. In addition, non-electrode systems utilizing laser-induced plasma as a probing pulse can be potentially used if insertion of the physical pin electrodes is not possible. Current approach is associated similar degree of complexity as spontaneous Raman scattering diagnostics while possess significantly easier implementation in comparison with CARS technique [70] [71] [72] [73].

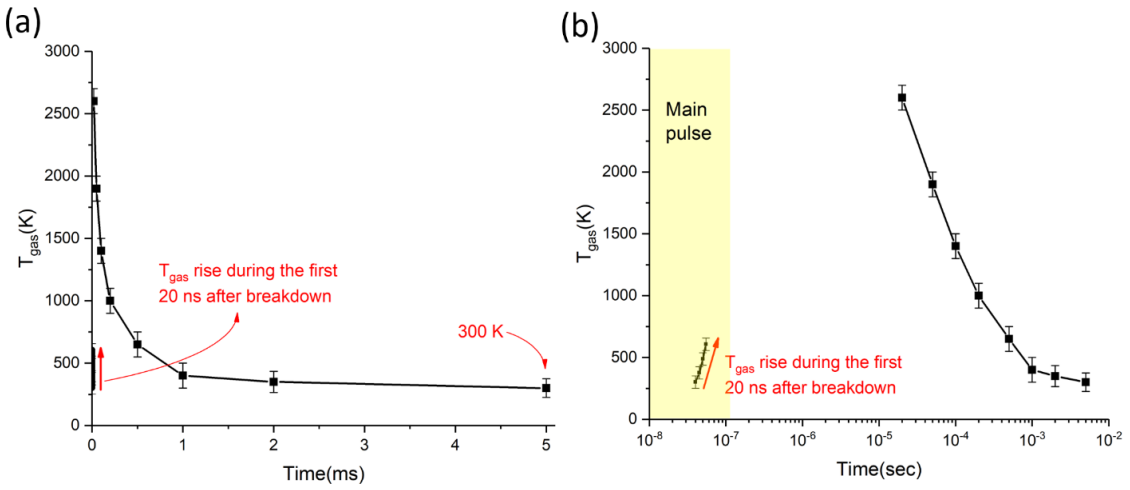

Fig 2-11. Temporal evolution of the rotational temperature measured using OES technique enhanced by nanosecond probing pulse. (a) in linear time scale, (b) in log time scale.

Temperature measurements immediately after the NRP pulse by choosing higher pulse repetition frequency or using separate HV pulser for creating probing pulses along with appropriate synchronization, and measurements of the gas temperature profiles across the spark channel by means of imaging the discharge directly onto the slit of the spectrometer are planned for the future work. Additionally, this method is to be tested with different gas mixtures at various pressures as a thermometer.

2.2.4 Conclusion

In this work, the novel method of gas temperature measurement utilizing optical emission spectroscopy enhanced with probing nanosecond plasma pulse is proposed. The method was applied to measure gas temperature evolution up to 5 ms after the NRP discharge. Specifically, for the NRP discharge in a pin-to-pin configuration, the temperature of gas peaked at a value of 2600 K about 20 μs after the discharge and cool down to about 650 K at 500 μs after the NRP discharge. The proposed method can also be applied for spatially (controlled by the interelectrode gap size) and temporally (down to 5 ns) resolved gas thermometry in various kinds of gas mixtures, e.g., in combustion.

2.3 Combined microwave and laser Rayleigh scattering diagnostics for pin-to-pin nanosecond discharge

Xingxing Wang, Adam Patel, and Alexey Shashurin
Purdue University, School of Aeronautics and Astronautics, West Lafayette, IN 47907, USA

This chapter has previously been published in J. Appl. Phys.
DOI: 10.1063/5.0054202

2.3.1 Abstract

In this work, the temporal decay of electrons produced by an atmospheric pin-to-pin nanosecond discharge operating in the spark regime was measured via a combination of microwave Rayleigh scattering (MRS) and laser Rayleigh scattering (LRS). Due to the initial energy deposition of the nanosecond pulse, a variance in local gas density occurs on the timescale of electron decay. Thus, the assumption of a constant collisional frequency is no longer applicable when electron number data is extracted from the MRS measurements. To recalibrate the MRS measurements throughout the electron decay period, temporally-resolved LRS measurements of the local gas density were performed over the event duration. Local gas density was measured to be 30% of the ambient level during the later stages of electron decay and recovers at about 1 ms after the discharge. A shock front traveling approximately 500 m/s was additionally observed. Coupled with plasma volume calibration via temporally-resolved ICCD imaging, the corrected decay curves of the electron number and electron number density are presented with a measured peak electron number density of 4.5×10^{15} cm^{-3} and decay rate of ~ $0.1\text{-}0.35\times10^{7}$ s^{-1}. A hybrid MRS and LRS diagnostic technique can be applied for a broad spectrum of atmospheric-pressure microplasmas where a variation in number gas density is expected due to an energy deposition in the discharge.

2.3.2 Introduction

Microwave Rayleigh scattering (MRS), or Rayleigh microwave scattering (RMS), has been proven as a powerful diagnostic for measuring total electron number (and number density) of microplasmas at atmospheric conditions - including helium plasma jets [22] [74] and laser induced plasmas [75]. The idea of MRS was first proposed by Shneider as a method for measuring total electron numbers in microplasmas [56]. The concept of the approach is based on the coherent

scattering of microwave radiation by a small plasma volume in the quasi-Rayleigh regime. When the prolonged plasma object is oriented along the linearly-polarized microwave electric field, electrons in the filament are polarized and consequently emit radiation in a Hertzian-dipole fashion. The electric-field amplitude of the scattered radiation detected is thus proportional to the total number of electrons inside the plasma volume.

Studies on nanosecond discharges with a pin-to-pin geometry have been conducted utilizing the MRS technique [76] [77]. Nanosecond discharge plasmas have been employed in a variety of situations which require rapid gas heating or efficient production of metastable and active species. Namely, in applications ranging from boundary layer control [45] [14] to the improvement of flame stability [52] [9]. It is thus crucial to conduct detailed diagnostics of ns-discharge plasmas under various operating conditions. In previous MRS studies, the full temporal evolution of total electron number (and density) was measured for pin-to-pin discharges at different discharge conditions (gap distance, energy deposition, repetition frequency, etc.). In those studies, it was assumed that the signal from the MRS system was solely a function of the total electron number - where the local gas density, and consequently collisional frequency, can be considered constant throughout the entire decay process.

However, this assumption is only valid when 1.) the plasma decay process is fast so that the time frame of interest is too short for any gas density variation to be realized or 2.) the energy deposition from the discharge is sufficiently small such that any gas density disturbance is negligible. From our previous measurements, we observed that the overall total electron decay lasts for several microseconds and is thus susceptible to thermo/hydrodynamic influence (sound in air at standard atmospheric conditions travels about 0.3 mm within 1 μs which is comparable with a typical diameter of the discharge column [76]). In addition, the energy deposition per pulse is typically several millijoules, which results in a local gas temperature rise of several-thousand Kelvin [78]. As a result, the assumption of a constant collisional frequency must be validated and assessed through local bulk gas density measurements.

Laser Rayleigh scattering (LRS) is one potential means of determining collisional frequency through non-intrusive measurements of local gas density. The technique is well-established for structure, flow field, and gas density measurements in the study of aerodynamics, combustion, and plasma physics [79] [80] [81] [82]. In collective random-phase LRS, induced electric dipole radiation is scattered in an incoherent multi-body fashion in the non-forward

direction – and is thus proportional to the gas density (number of scatterers). Scattering features additionally reflect perturbations in pressure, temperature, and internal energy states of the gas [79]. For atmospheric pressure plasmas where the ionization degree is relatively low, incoherent neutral Rayleigh scattering is expected to dominate over Thomson scattering on plasma electrons [21].

In this work, the MRS signal from a pin-to-pin discharge is recorded at atmospheric conditions. A laser Rayleigh scattering technique is then adopted to investigate local gas density variations throughout electron decay. The corrected total electron decay curve is correspondingly acquired utilizing a hybrid of the MRS and LRS techniques. With additional measurements of the plasma volume via an ICCD imaging technique, the temporal evolution of spatially-averaged electron number density is finally presented. The results of this study suggest the necessity of accurate local gas number density measurements for the correct correlation between MRS data and plasma electron number density.

2.3.3 Experimental details

A high voltage (HV) nanosecond pulse was applied to two tungsten pin electrodes separated by a gap distance d = 5 mm at atmospheric conditions (T = 298 K, p = 1 atm). The HV pulse was produced by an Eagle Harbor NSP-3300-20-F – with a peak value of 24 ± 0.1 kV and a pulse width of 90 ± 3 ns. The pulser was operated in single pulse mode at a maximum repetition frequency of 1 Hz to eliminate any memory effects between the adjacent pulses. Under these conditions, the discharge operates in the spark regime [77] [83] [32]. The corresponding average energy deposition per pulse is approximately 5 ± 0.2 mJ, calculated through numerical integration of the product between voltage and current. The voltage was measured by two high voltage probes (Tektronix P6015A), each connected to respective output legs of the pulser. The pulser was operated in a floated mode such that the voltage pulse applied to the electrodes was calculated as the difference between the two probe measurements. The discharge current was measured by a high-frequency current transformer (Bergoz FCT-028-0.5-WB). A schematic of the discharge setup and diagnostics is illustrated in *Figure 2-12* below and outlined in the color blue. Electric signals of various diagnostic equipment were interpreted through an oscilloscope (Lecroy HDO3904, 3 GHz bandwidth, 40 GS/s sampling rate).

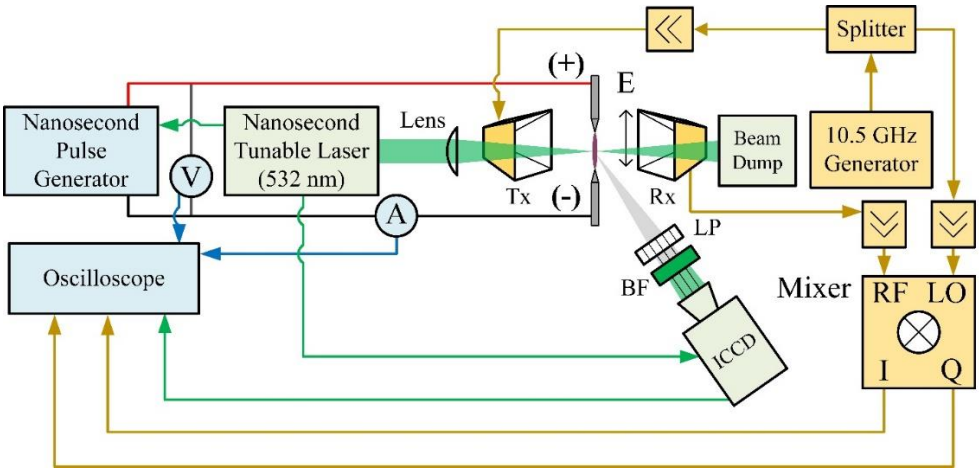

Figure 2-12. Schematic of the ns-discharge setup (blue), MRS diagnostic equipment (gold), and LRS diagnostic equipment (green).

The total electron number (N_e) and electron number density (n_e) is measured by the microwave Rayleigh scattering (MRS) technique and ICCD (Princeton Instruments PI-MAX 1024i) volume imaging. A 10.5 GHz MRS homodyne detection system was built and utilized for the absolute measurement of electron number density - after calibration with a dielectric material with known properties by Equation (1) below. The schematic of the MRS system circuitry is additionally depicted in **Figure *2-12*** in yellow [56]. In this setup, the microwave horn antennas have a gain of 10 dB with a corresponding Tx output power of ~38 dBm.

$$U_{out} = \begin{cases} A\frac{e^2}{mv}N_e = A\frac{e^2}{mv}n_e V - & \text{for plasma} \\ AV\varepsilon_0(\varepsilon - 1)\omega & - \text{ for dielectric bullet scatterer} \end{cases} \quad (1)$$

where e: electron charge

m: electron mass

ε_0: dielectric permittivity of vacuum

ε: relative permittivity of dielectric material

ω: microwave frequency

v: collisional frequency

A: proportionality factor

V: volume of the plasma/dielectric scatterer

U_{out}: signal detected by the MRS system

The proportionality factor A is determined from the second expression in Equation (1) by applying the MRS system to a dielectric scatterer with known properties. It can then be applied to upper Equation 1 for the evaluation of the total electron number, N_e, in plasmas. The electron number density, n_e, can then be calculated using ICCD plasma volume measurements. It is important to note that there exists an upper limit on the plasma density that an MRS system can measure. In order for Equation 1 to be valid, the plasma diameter needs to be smaller than the skin layer depth - which is governed by the electron number density. For instance, for a skin layer depth of 300 μm, the soft upper limit of n_e that a 10 GHz MRS system is applicable with is 10^{16} cm^{-3}.

In addition to the aforementioned diagnostic techniques, a laser Rayleigh scattering system was utilized for the measurement of the local gas density, n_g, and determination of collisional frequency. As LRS is an incoherent scattering process, the intensity of the scattered signal is linearly proportional to the local gas density. It should be noted that the sensitivity of the laser Rayleigh scattering system is also affected by the cross section of the molecules, which is partially governed by the gas temperature. However, this dependence is relatively weak (~ 1% per 1000 K) [84]. Given that the temperature variation for the pin-to-pin ns-discharge is less than 5000 K, we thus assume that the change of the scattering signal is solely determined by the local gas density. A ~5 ns, 1 ± 0.1 mJ laser pulse at 532 ± 0.5 nm was produced by a broadly-tunable Nd:YAG laser (EKSPLA NT342) with Pellin-Broca spectral cleaning filter. The output laser pulse was found to be a linearly-polarized 7 mm dia. top hat profile – which was then focused to the center of the ns-discharge via a 175 mm plano-convex lens. The scattered signal was finally captured by the aforementioned ICCD camera, with an additional 532 ± 10 nm band pass filter, film polarizer, sufficiently short camera gate width, and broad spectra absorbing backdrop for LRS signal isolation (mitigate reflection, straylight, and fluorescence). 532 nm was selected as the central wavelength due to low absorption by neutral and ion species. It will be shown below that even though the LRS signal overlaps with Thomson and Raman scattering [16], the contribution of Rayleigh scattering is dominant for the experiemntal conditions in this work. In experiment, averaging of the scattering event at consistent timestamps was performed to mitigate variance in laser and ns-discharge features. Timing of LRS was achieved through external triggering of the nanosecond pulser and ICCD camera from the laser (laser jitter ± 0.5ns) and confirmed via a combination of the ICCD monitor and oscilloscope signals. A detailed schematic of the LRS system is additionally depicted in Figure *2-12* in green. Gas density n_g is measured from 150 ns to

1 ms after the initiation of the HV pulse where the local density finally returns to ambient conditions.

2.3.4 Results and discussion

A typical temporal evolution of the voltage (*V*) and current (*I*) waveforms are presented below in Figure *2-13*. One can see that the breakdown occurs at a voltage level of approximately 20 kV with a corresponding peak current of ~18 A. Note, the double peaks seen on the current waveform can be explained by output variations of the pulser. The sudden drop of resistance between the electrodes caused by the breakdown prevents creation of an ideal boxcar voltage waveform by the pulser and leads to appearance of the second current peak. The peak is associated with the discharge stage when highly conductive plasma channel connects the electrodes, leading correspondingly to high discharge current and low discharge voltages (typical for arcs and sparks) [83] [18].

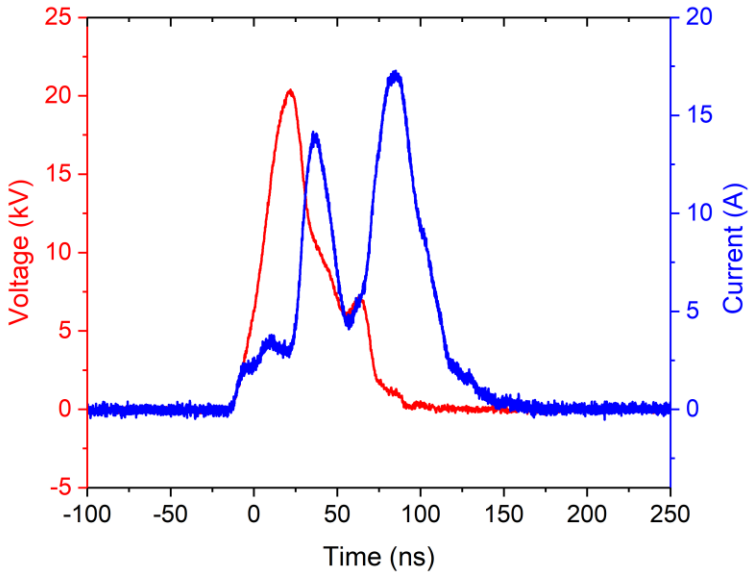

Figure 2-13. Voltage (red) and current (blue) waveforms of the nanosecond HV pulse.

The volume of the post-discharge plasma channel is approximated from ICCD imaging, and the temporal evolution of the column diameter and volume is plotted in Figure *2-14*(a). One can see that the volume of the plasma expands for 0.5-9 μs [31]. A smoothed line connecting datapoints will be utilized below for the evaluation of n_e from the microwave scattering signal.

Figure *2-14*(b) presents a sample of ICCD images used for the evaluation of the plasma diameter. Note, some recent works utilize Abel inversion in order to evaluate the actual plasma size [27] [85]. However, spatial distribution of the photon emission might be not representative of the plasma electron spatial distribution since various sources (species) contribute to the total emission pattern. Additionally, plasma size estimated based on line-of-sight integrated images and Abel inverted ones are comparable (within 10%) [85]. Therefore, in this work we estimated the plasma volume directly from the ICCD images without Abel inversion.

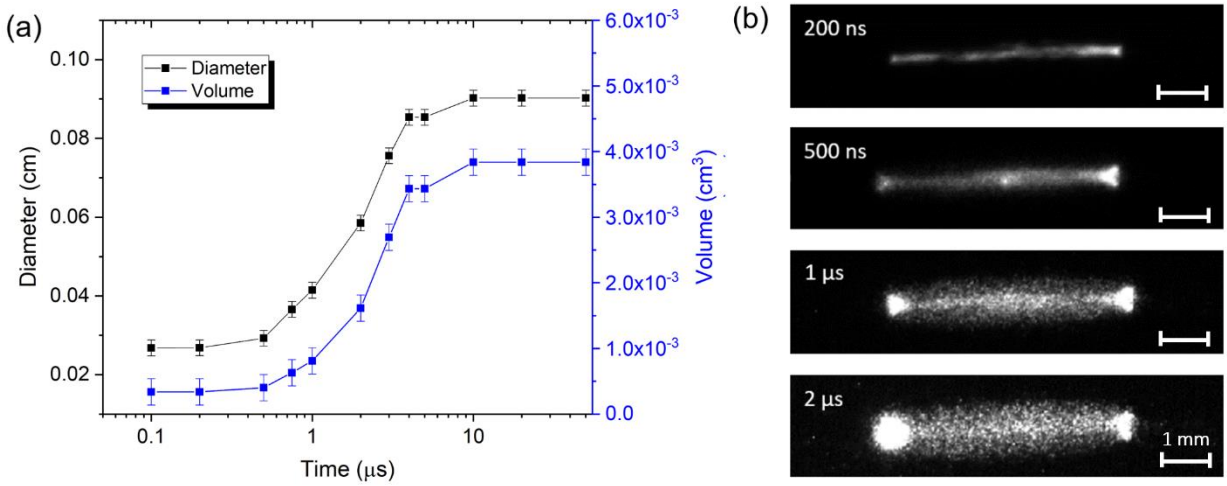

Figure 2-14. (a) Temporal evolution of the plasma diameter and volume. Black line + scatter: visual measurement for diameter; Blue line + scatter: calculated plasma volume. (b) Sample ICCD images of the plasma dimensions.

The temporal evolution of the microwave scattering signal U_{out} is depicted below in Figure *2-15*. It can be observed that the curve is composed of three distinct regions: 1.) fast signal decay for a duration of ~ 50 ns; 2.) a 'plateau' region for a duration of ~ 500 ns; 3.) slow signal decay for a duration of ~ 4 μs. This may appear unphysical if the decay curve for n_e shares a similar pattern to U_{out}.

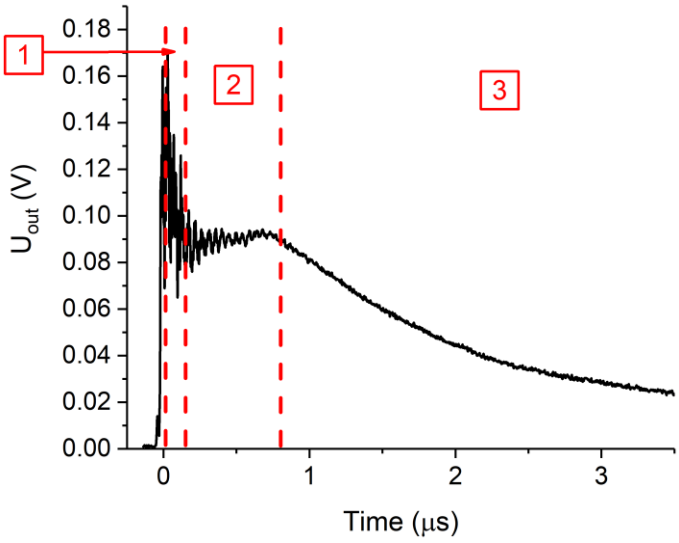

Figure 2-15. Temporal evolution of U_{out} measured by the MRS system. Three distinct regions of microwave scattering behavior are distinguished by the dashed red lines.

To qualitatively understand the decay behavior of U_{out}, dynamics of gas density must be considered. The collisional frequency in Equation (1) can be determined as follows [18]:

$$\nu[s^{-1}] = n_g \sigma_{e-g} v_{Te} = 1.95 \times 10^{-10} \times n_g[cm^{-3}] \times \sqrt{T_e[K]} \qquad (2)$$

Thus, the scaling between U_{out}, n_g, n_e, and V can be acquired using Equations (1) and (2):

$$U_{out} \propto \frac{n_e V}{n_g} \propto \frac{N_e}{n_g} \qquad (3)$$

In cases where collisional frequency cannot be assumed constant and T_e is invariant, U_{out} is a direct measurement of the ratio between the total electron number and local gas density. If the volume is additionally constant throughout the decay process, U_{out} is then the measurement of the ratio of electron number density over local bulk gas density, which is the ionization degree (for weakly ionized plasmas).

Let us start with a qualitative interpretation of the temporal evolution of U_{out} observed in Figure *2-15*. For the discharge event shown in Figure *2-15*, no significant changes in gas density and plasma volume are expected for the fast timescale of region 1 (t < 50 ns) – thus n_e is governing change of U_{out} in expression (3) and the two share a similar profile. For t > 50 ns, due to the energy deposition by the discharge, air is heated at the core and forms a shock/sonic wave that expands

outwards - resulting in a local density drop. The plateau of U_{out} observed for 50 ns < t < 700 ns (region 2) can thus be explained by a decrease in gas density and increase in plasma volume. Indeed, as shown in expression (3), a drop in n_g and increase in V can compensate for the drop in n_e - resulting in the plateau. The slow decay rate observed within region 3 can also be explained by a decrease in local gas density, which will be later discussed in detail. A similar dynamic change in local gas density post-discharge can be observed in others' work: namely, in a ns-discharge with pin-to-plane geometry at atmospheric condition, simulations show that local gas density drops up to 2-times 700 ns after the discharge, which is consistent with the time period of region 2 observed. After reaching the minimum value, the gas density slowly recovers and remains approximately constant for the next few microseconds [31].

Let us now conduct quantitative studies of the local gas number density and determine N_e and n_e. The local relative gas density (n_g/n_{g0}, where n_{g0} is gas number density at standard atmospheric conditions -2.5×10^{19} cm^{-3}) was acquired by Laser Rayleigh scattering from 150 ns up to 1 ms after the discharge. The resulting temporal evolution of the local relative gas density at the core of the discharge is presented in Figure *2-16*(a) below. One can see that for ~ 1 μs after the discharge, local n_g quickly drops to 30% of the ambient level and stays constant until about 50 μs. It then slowly recovers to the ambient level within the next ~900 μs. Figure *2-16*(b) shows some example profiles of the gas density distribution at the mid-point between the electrodes along the radial direction for 1-5 μs post-discharge. A shock/sonic wave that propagates outwards at a velocity of approximately 500 m/s can also be observed. A smoothed line connecting data points for the first 5 μs was implemented for the determination of N_e and n_e from the MRS measurements.

Note that the LRS signal is typically intricate and entangled with straylight, reflection, fluorescence, Thomson scattering, and Raman scattering. However, straylight, reflection, and fluorescence are mitigated through the aforementioned polarizer, bandpass filter, spectra absorbing backdrop, and short ICCD gate – as confirmed by negligible signals off the main illumination line and without the laser. Further, Thomson scattering is low in comparison with the pure LRS signal due to a low ionization degree ($\alpha < 10^{-3}$ and $n_e < 5\times10^{15}$ cm^{-3}) used in this study. Indeed, by estimating intensity of both Thomson and Rayleigh laser scattering based on known cross-sections and experimentally determined number densities, and by reviewing experimental results reported previously, it can be inferred that contribution of Thomson scattering signal is important only when $n_e \geq 10^{16}$ cm^{-3} [21] [85]. Raman scattering is also distinguishably weaker than Rayleigh scattering

as justified through a smaller cross section (~ 2 orders of magnitude) [21]. Such estimates are consistent with efforts to disentangle these events and have been consequently considered via an uncertainty bar. Additionally, the effect of oxygen dissociation on the measurements conducted in this work was considered. This is motivated by the recent findings reporting O_2 dissociation degrees up to 50% for nanosecond repetitively pulsed discharges in preheated air (preheated to 1000 K, pulse energy 0.67 mJ, repetition frequency 10 kHz) [27], and up to 30% in discharge conditions more comparable to the current work (no preheating, pulse energy 20 mJ, repetition frequency 10 Hz) [86] [87]. Specifically, we estimated how the final values of n_g and n_e, determined from LRS and MRS measurements, would change between the full O_2 dissociation (FD) and no O_2 dissociation (ND) cases. For LRS, the effect is governed by the corresponding laser Rayleigh scattering cross-sections (σ_{LRS}) as $\frac{n_{g,FD}}{n_{g,ND}} = \frac{2(0.22)\sigma_{LRS,O}+(0.78)\sigma_{LRS,N_2}}{(0.22)\sigma_{LRS,O_2}+(0.78)\sigma_{LRS,N_2}} = 0.886$ [84]. For MRS, the electron number density is proportional to the electron-neutral collision frequency $n_e \propto \nu = n_g\sigma_{e-g}v_{Te}$ (see the first expression in Eq.1; all other parameters will be considered the same for our estimate). The change in the final determined n_e-value is then governed by the corresponding cross-sections of electron-gas collisions (σ_{e-g}) and the neutral densities determined from LRS as $\frac{n_{e,FD}}{n_{e,ND}} = \frac{\nu_{m,FD}}{\nu_{m,ND}} = \frac{2(0.22)\sigma_{e-O}+(0.78)\sigma_{e-N_2}}{(0.22)\sigma_{e-O_2}+(0.78)\sigma_{e-N_2}} \cdot \frac{n_{g,FD}}{n_{g,ND}} \approx 0.964 \cdot 0.886 = 0.853$ [88] [89] [90]. Given that the effect of oxygen dissociation on the final results is weak (within 15%) in this work, we have neglected the dissociation as a zero-order approximation and accounted for its potential variations via uncertainty bars for n_g and n_e.

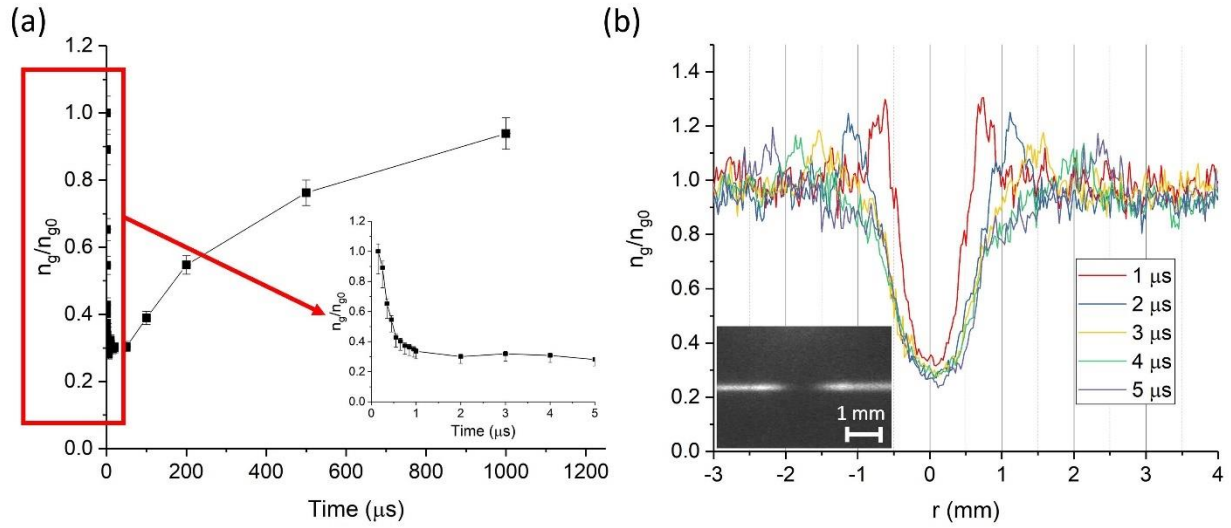

Figure 2-16. (a) Temporal evolution of local gas density measured by LRS. (b) Example profiles of the density distribution along the radial direction of plasma filament for 1-5 μs after discharge. A sample of the LRS raw image is displayed on the left-bottom corner at t = 3 μs.

With the measured temporal evolution of local gas density, one can calculate the collisional frequency ν with equation (2) and finally determine N_e and n_e from the MRS measurements. (The electron temperature T_e was assumed to be decaying from 10000 K down to 2000 K within the initial 1 μs and stays constant at 2000 K [91]) The calculated ν is substituted into equation (1) to acquire the temporal evolution of N_e and the corresponding result is shown below in Figure 2-17(a). One can see from Figure 2-17(a) that the maximum number of electrons produced is approximately 1.0×10^{12}. The correction performed with LRS 'smooths' the 'plateau' observed in Figure 2-15 – supporting the previous physical explanation. It additionally lowers the relative values in region 3 of Figure *2-15*, reducing the decay time of N_e to around 1 μs. Finally, after substituting the ICCD-measured volume of the plasma, one can acquire the corrected temporal evolution of n_e which is additionally illustrated in Figure 2-17(b). One can see that the peak value of n_e reaches approximately 4.3×10^{15} cm^{-3} and decays around ~500 ns. In comparison with decay curve of N_e, the decay of n_e is faster. This is due to the factor of plasma volume expansion which further enhances the reduction of electron number density.

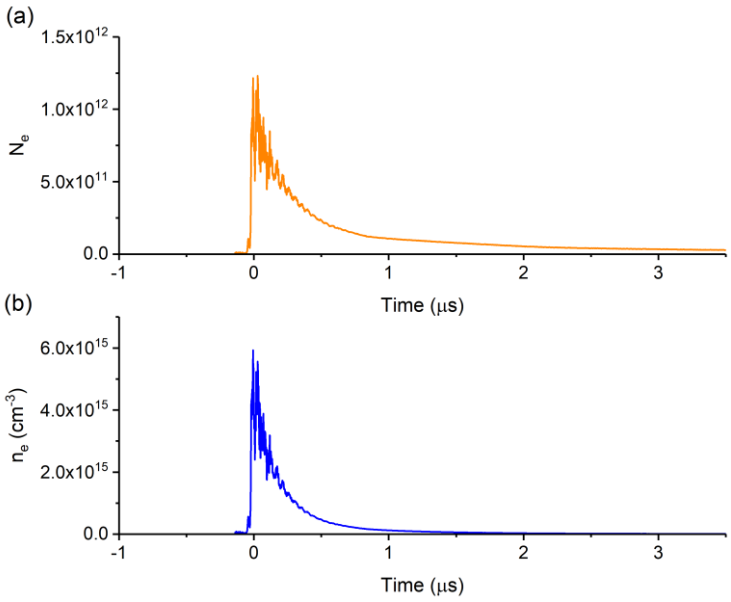

Figure 2-17. Temporal evolution of (a) N_e and (b) n_e.

Let us now examine the experimental decay curve with theoretical predictions. Two mechanisms can contribute to the decay of n_e: ion-electron recombination (β as the recombination rate) and three-body attachment (ν_{att} as the attachment rate). One can see that the peak value of n_e was found to be $n_e \sim 4.3\times10^{15}$ cm^{-3}. Since three-body attachment is expected to be dominant when $n_e < 10^{16}$ cm^{-3} (where $\beta \cdot n_e < \nu_{att}$), the governing decay mechanism in our case can be determined to be three-body attachment: $n_e(t) = n_{e_0} e^{-\nu_{att} t}$, where $\nu_{att.}$ can be expressed as $\nu_{att} = k_1 n_{N_2} n_{O_2} + k_2 n_{O_2}^2$ [92] [93] [94]. With attachment coefficient k_1 and k_2 being inversely proportional to T_e, one can calculate the attachment rate by:

$$\nu_{att}[s^{-1}] = 0.78 \times 10^8 \times \left(\frac{n_g[cm^{-3}]}{2.5\cdot10^{19}}\right)^2 \times \left(\frac{300}{T_e[K]}\right) \qquad (4)$$

The resulting attachment rate ν_{att} was calculated to be in the range from 0.35×10^7 s^{-1} down to 0.1×10^7 s^{-1} as decay progresses. The corresponding characteristic decay time is around 100s of ns which is consistent with the experimental results. Further, in comparison with the value at standard atmospheric conditions (0.78×10^8 s^{-1}), the decay rate in our case is lower by 20-70 times due to local reduction of neutral gas density at the discharge location.

Finally, errors in n_e-measurements conducted by the proposed MRS-LRS method are governed by the corresponding measurement errors of microwave scattering signals (U_{out}), gas number densities

(n_g), the microwave system calibration factor (A), and the plasma volume (V). The contribution of various error sources has to be considered specifically in each experiment. In the current experiment, n_e-measurement error was around 25% dominated by the measurement errors of n_g and V.

2.3.5 Conclusion

In our recent studies of pin-to-pin ns-discharges utilizing Rayleigh microwave scattering diagnostics, we encountered cases where the MRS signal cannot be directly interpreted into electron number density. This is attributed to a dynamic change in local air properties – such as gas density and electron temperature. Through the application of laser Rayleigh scattering, local gas density was measured and utilized to 're-calibrate' the MRS system. The electron number density was then re-evaluated. For the ns-discharge plasma studied in this case, it is shown that energy deposition by the discharge reduces local gas density by as much as 30% of ambient conditions. This leads to a reduction of the three-body attachment rate by as much 70 times in magnitude. It can then be concluded that there is a necessity for local gas density and electron temperature measurements in order to fully calibrate MRS electron number/density measurements for high energy deposition discharges. A hybrid MRS and LRS diagnostic technique demonstrated in this work can be utilized for a broad spectrum of atmospheric-pressure microplasmas where a variation in number gas density is expected due to an energy deposition in the discharge such as atmospheric pressure plasma jets and laser-induced plasmas [95] [96] [97].

3 STUDY OF THE NRP PIN-TO-PIN DISCHARGES

3.1 Experimental study of atmospheric pressure nanosecond discharge in pin-to-pin configuration

Xingxing Wang, Adam Patel, Sally Bane and Alexey Shashurin

This chapter has been submitted for publication and is currently under review

3.1.1 Abstract

In this work, we present an experimental study of the nanosecond high-voltage discharges in a pin-to-pin configuration at atmospheric conditions operating in single-pulse mode (no memory effects). Various discharge parameters, including voltage, current, gas density, rotational/vibrational/gas temperature, and electron number density, were measured. Diagnostic complex including microwave Rayleigh scattering, laser Rayleigh scattering, optical emission spectroscopy enhanced with nanosecond probing pulse, fast photography and electrical parameter measurements was utilized. Spark and corona discharge regimes were studied with discharge pulse duration of 90 ns and gap sizes 2-10 mm. The spark regime was observed for gaps < 6 mm at tested range of discharge pulse energies 0.6-1 mJ per mm of the gap size. Higher electron number density, total electron number per gap size, discharge current, and gap temperature were observed at smaller gaps and larger pulse energy reaching maximal values of about 7.5×10^{15} cm^{-3}, 3.5×10^{11} electrons per mm of gap, 22 A, and 4,000 K (at 10μs after the discharge), respectively, for 2 mm gap and 1 mJ/mm discharge pulse energy. Initial breakdown was followed by a secondary breakdown occurring about 30-70 ns after the first one and was associated with ignition of cathode spot and transition of the discharge to cathodic arc. Majority of the discharge pulse energy was deposited into gas before the secondary breakdown (around 85-89%). Electron number density after the ns-discharge pulse decayed at characteristic time scale of 150-200 ns governed by dissociate recombination and attachment to oxygen mechanisms. For corona regime, substantially lower pulse energies (~0.1 mJ/mm), conductivity current peak (1-2 A), and electron numbers ($3\text{-}5\times10^{10}$ electrons per mm of gap), and gas temperatures (360 K) were observed.

3.1.2 Introduction

Nanosecond discharges (ns-discharges) has recently been proven valuable over a wide range of applications in the fields of combustion, aerodynamic, medicine, and others. The nanosecond-scale rise time of the voltage pulse up to high-kV values enables the local electric field to increase rapidly before breakdown, energizing electrons to very high energy levels. [23] This enables a production of variety of reactive species (ozone, NO_x, OH, O, etc.). During the relaxation of excited and ionized species, a large amount heat can further be released leading to fast gas heating. [25] [24] Additionally, fast gas heating generates strong pressure gradients generating a shock wave and inducing vortexes that can be further used to fulfill a particular aerodynamic purpose.

Ns-discharges have been widely applied in the field of combustion for multiple purposes. They have been utilized for sustaining fuel-lean combustion by providing a substantial amount of active species (O, H, OH, etc.) as well as for additional gas heating. [9] [10] [11] Other relevant combustion applications include increasing of flame speed, and mitigating flame instabilities. [38] [39] [41] [42] [44] [43] In the field of aerodynamics, ns-discharge have been utilized in the form of dielectric barrier discharges (DBDs) on the surface of an airfoil which are known as plasma actuators. The boundary layer is modified through gas heating which leads to a delay of the flow separation, and ultimately results in a reduction of drag. [45] [14] Other aerodynamic applications of ns-discharges include shock wave modification and instability-induced flow manipulation. [48] [49] [50] Furthermore, ns-discharges operating at atmospheric conditions has also found merit in a diverse range of fields such as medicine, nanotechnology, material processing and sterilization. [1]

A comprehensive study of properties of ns-discharges is crucial to tailor the plasma to particular application. A logical first step in conducting that study would be to analyze a single-pulse ns-discharge before accessing the more complicated regime of nanosecond repetitively pulsed (NRP) discharges where memory effect between the adjacent pulses is present (when perturbations induced by an individual HV pulse would not decay fully before the subsequent pulse). In contrast, vast majority of current studies have been conducted for the NRP discharges with high repetition frequencies (~ 10 kHz) by implementing multiple diagnostic techniques including optical emission spectroscopy (OES), Stark broadening, laser Thomson/Rayleigh scattering, LIF, microwave Rayleigh scattering, estimation of plasma conductivity based on

measuring resistance of plasma column, etc. [26] [51] [28] [29] [30] [31] [32] [76] Whereas a comprehensive study of the single-pulse ns-discharge is still lacking in the meantime.

For the single-pulse pin-to-pin ns-discharges, Lo [98] studied 3 mm interelectrode gap energized by 25 ns and 54 mJ high voltage pulses. The electron number density until 320 ns after the initiation of discharge and electron temperature until 40 ns were determined using Stark broadening, which yielded a peak value of about $9.2 \cdot 10^{18}$ cm^{-3} and 45,000 K, respectively. The measurements were taken at the core of the plasma filament with a spatial resolution of approximately 10 μm and temporal resolution of 5 ns. Additionally, gas temperature of up to 1,200 K at 15 ns after the initiation was measured using OES of 2nd positive system of N_2. In another work by Miles, [33] 2 mm interelectrode gap, 8 mJ pulse energy, and 55 ns pulse duration was studied. The resulted electron number density and electron temperature were measured by laser Thomson scattering peaking at approximately 10^{17} cm^{-3} and 3.2 eV, respectively, at 500 ns after the pulse initiation at a spatial resolution of 150 μm.

In this work, a comprehensive, multi-parametric study of the single-pulse ns-discharges in pin-to-pin configuration at atmospheric conditions was conducted for the interelectrode gap sizes in the range 2-10 mm. Discharge voltage, current, rotational/vibrational temperatures, local gas density, and electron number density were determined and analyzed under different discharge conditions including gap distance between electrodes, level of energy deposition.

3.1.3 Methodology and Experimental Setup

A detailed schematic of the experimental setup is illustrated in Figure 3-1. The electrodes, HV power supply, and traditional voltage/current probes are drawn in the color blue. The nanosecond HV pulse was produced by an Eagle Harbor NSP-3300-20-F, where the peak voltage was set to be approximately 25 kV and the pulse width to about 90 ns. Two leads representing the positive and negative polarity outputs are each connected to tungsten pin electrodes with a tip radius of curvature of around 100 μm. Since the pulser is generating a floating output signal, the actual voltage applied to the electrode assembly was measured by two HV probes where each of the probes was connected to the corresponding output line and shared same ground. The voltage probe model utilized in this experiment is a high voltage Tektronix P6015A with a maximum rating of 30 kV and a bandwidth of 60 MHz. The current was recorded by a high-frequency current transformer (Bergoz FCT-028-0.5-WB) with a bandwidth of 1.2 GHz connected on the positive

lead of the pulser near electrodes. All signals were recorded by high bandwidth oscilloscopes (Lecroy HDO3904, 3 GHz bandwidth, 40 GS/s sampling rate: Lecroy WavePro 735Zi, 3.5 GHz bandwidth, 40 GS/s sampling rate). The HV pulses were sent to the electrodes at a maximum pulsing frequency of 1 Hz to ensure no memory effects from the previous discharge pulses. To improve the pulser impedance matching during the discharge, an additional matching resistor stage (a 5 kΩ resistor connected in parallel and two 260 Ω resistors connected in series) was utilized. Gap distance between electrodes was adjusted in the range 2-10 mm and measured by a caliper. To adjust energy deposition into the discharge, additional resistor *R* of 200 or 400 Ω were added in series with each discharge electrode.

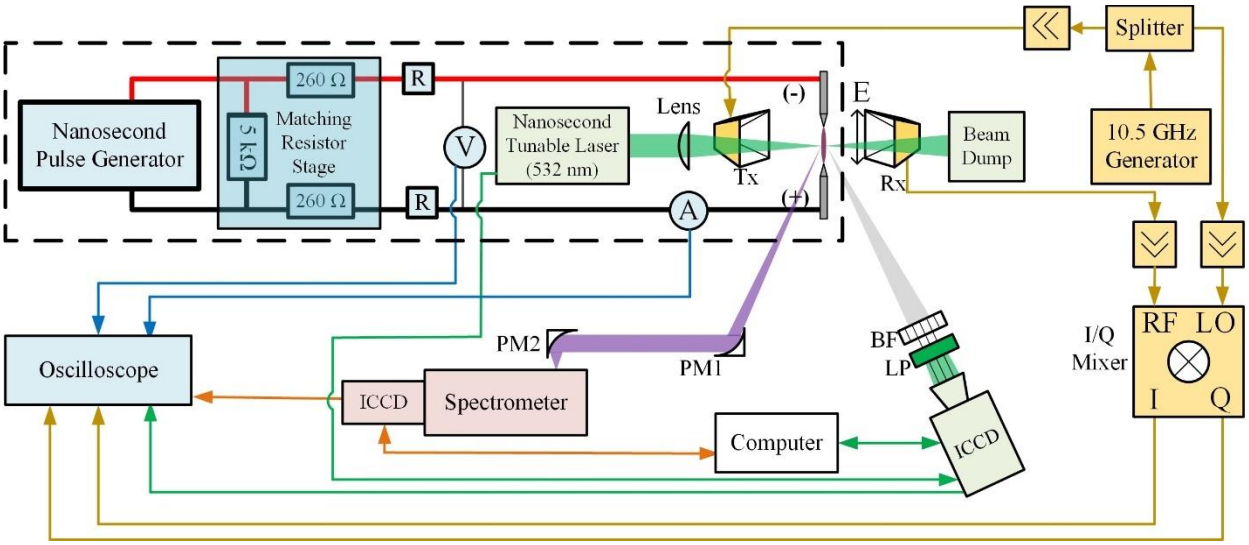

Figure 3-1. Schematic of the experimental setup. (Blue) Pulse generator and voltage/current diagnostics. (Green) Laser Rayleigh scattering equipment. (Red/Orange) OES equipment. (Yellow) Microwave Rayleigh scattering equipment.

The OES temperature measurement portion of the experimental setup is shown in Figure 3-1 and highlighted in red. In this measurement, emission of the 2nd positive system (SPS) of nitrogen with $\Delta\nu = \nu' - \nu'' = -2$ (corresponding to the relaxation of excited nitrogen molecules C to B-state) was recorded and fitted in SPECAIR to evaluate the rotational, T_{rot}, and vibrational, T_{vib}, temperatures of the gas. SPS has been widely used previously for the determination of temperatures for air and N_2 plasmas. [98] [99] [100] [101] [74] T_{gas} was taken to be equal to T_{rot} in these measurements based on fast rotational–translational relaxation and the predominant

creation of nitrogen $N_2(C)$ by electron-impact excitation of $N_2(X)$. [78] It has to be noted that the T_{vib} measured and presented in this work is the vibrational temperature for N_2 in the C state rather than the X ground state. From the recorded spectrum, one can estimate $T_{vib}(X)$ from $T_{vib}(C)$ through the Franck-Condon coefficients - assuming that the majority of $N_2(C)$ is excited from $N_2(X)$. [102] The emission spectra at the mid-point between electrodes were captured by a dual-parabolic-mirror system with a probing volume of approximately 0.05 mm^3, sent to a spectrometer (Princeton Instruments SP-2750i) and was then recorded by an ICCD camera (Princeton Instruments PI-MAX4). For measurements during the ns-discharge, a gate width of 5 ns and a time step of 5 ns was used. For measurement of gas temperature after the discharge, OES enhanced with a probing ns-pulse was utilized. [78] The idea of the method is based on utilization of the probing pulse in order to excite the emission of the SPS at the desired moment of time while ensuring that heating by the probing pulse itself is negligible. 50-200 accumulations were taken to enhance signal-to-noise ratio for all OES spectra. A detailed description of the method can be found elsewhere. [78]

For visualization of the plasma discharge, the ICCD camera was placed directly in front of the discharge to record the broadband light emission. The diameters of the plasma channels (D) were estimated from the recorded images.

For the evaluation of local bulk gas density n_g, Laser Rayleigh scattering (LRS) was utilized. LRS is a widely-used technique for the determination of gas density with notable prominence in the fields of aerodynamics and combustion. [79] [80] [81] [82] [21] After applying a laser beam into a gaseous object of interest, the incoherent scattered signal of gas particles can be collected for the measurement of local gas density - as the signal intensity is proportional to the amount of gas particles within the probe volume. The intensity of the LRS signal is also a function of local gas temperature. However, the dependence between signal intensity and temperature is not strong in comparison (~1% per 1000 K). [84] As the bulk gas temperature measured in this study will be shown to be no more than 5000 K, it is assumed that LRS signal is solely a linear function of local gas density. This portion of the experimental setup is depicted in Figure 3-1 and highlighted in green. A broadly-tunable Nd:YAG laser with Pellin-Broca spectral cleaning filter (EKSPLA NT342) was utilized to produce a 5 ns, 1±0.1 mJ laser pulse at 532±0.5 nm. The linearly-polarized beam was then focused to the plasma centroid and the scattered signal was captured by an ICCD camera. A 532±10 nm band pass filter and film polarizer was installed at an angle perpendicular to the laser beam/plasma filament for improved LRS signal isolation. Even

though the LRS signal overlaps with Thomson and Raman scattering, the contribution of Rayleigh scattering was dominant for the experimental conditions in this work when $n_e < 10^{16}$ cm^{-3} as described in [103]. Scattered laser signals were recorded for a range of times (100 ns to 1 ms) after the discharge. Accumulations of 10 events were taken to improve the signal-to-noise ratio and mitigate laser variance. The measurement of n_g through LRS was further applied to equation (2) below for the evaluation of collisional frequency ν, and ultimately for the evaluation of n_e by microwave Rayleigh scattering which will be discussed in detail in the following paragraphs.

For microwave Rayleigh scattering (MRS) measurements of total electron number N_e and electron number density n_e, a homodyne microwave scattering system at 10.5 GHz was constructed for this experiment. The schematic is shown in Figure 3-1 and highlighted in yellow. MRS is a non-intrusive diagnostic technique first proposed by M. N. Shneider and R. B. Miles for the measurement of electron number density of microplasmas at atmospheric conditions. [56] The technique is principally based on elastic microwave-plasma scattering in the quasi-Rayleigh regime. It depicts the irradiation of a plasma channel by a uniformly distributed, parallel microwave field - resulting in a linearly-polarized filament with Hertzian dipole radiation characteristics. The scattered microwave intensity from the collisional-bound electrons can thus be a measure of the total number of electrons inside the plasma body – as the scattered E-field is proportional to the electron count. This method has been successfully applied to a variety of microplasmas including laser induced plasmas, helium plasma jets, and pin-to-pin NRP discharges. [36] [22] [76] [74] [97] The expressions for output signals of the MRS system are as follow: [56]

$$U_{out} = \begin{cases} A\frac{e^2}{m\nu}N_e = A\frac{e^2}{m\nu}n_e V - & \text{for plasma} \\ AV\varepsilon_0(\varepsilon - 1)\omega \quad - & \text{for dielectric bullet scatterer} \end{cases} \tag{1}$$

where e: electron charge
m: electron mass
ε_0: dielectric permittivity of vacuum
ε: relative permittivity of the dielectric bullet
ω: microwave frequency
ν: collisional frequency
A: proportionality factor
V: volume of the plasma/dielectric scatterer
U_{out}: signal detected by the MRS system
N_e: total number of electrons
n_e: electron number density

For a ns-discharge in air with relatively low degree of ionization, the collisional frequency v can be calculated as: [18]

$$\nu[s^{-1}] = n_g \sigma v_{Te} = 1.95 \cdot 10^{-10} \cdot n_g[cm^{-3}] \cdot \sqrt{T_e[K]} \qquad (2)$$

For the evaluation of collisional frequency, T_e was assumed to be decaying from 10000 K down to 2000 K within the first 1 μs – where it stays constant for the remainder of the plasma lifetime. [33] [104] For the duration of ns-pulse, n_g can be assumed constant throughout the discharge. However, it has been demonstrated that the pin-to-pin nanosecond discharges considered in this study have energy depositions on the order of ~5 mJ and a corresponding temperature rise of multiple thousands of Kelvins are expected. [78] It is thus necessary to treat n_g as a variable after the ns-discharge when calculating n_e – hence, the temporal measurement of gas density is required and was provided by laser Rayleigh scattering (LRS) measurements. More details about the necessity to account for n_g variation from the unperturbed atmospheric level due to ns-discharge and validation of combined MRS-LRS diagnostics can be found elsewhere in [103].

Finally, the output signal U_{out} of the MRS signal was calculated from the outputs of the I/Q mixer utilized in the detection circuit: $U_{out} = \sqrt{\delta I^2 + \delta Q^2}$. A calibration process was firstly done with a Teflon cylinder (1/8'' diameter, 1 cm length) with known dielectric property to evaluate coefficient A based on the bottom expression in the equation (1). The calibrated MRS system was then applied to the ns-discharge plasma. The corresponding U_{out} signal was utilized accompanied with v derived from LRS measurement to calculate N_e by top expression in the equation (1). With estimated diameter of the plasma based on ICCD image, one can estimate the spatially-averaged electron number density n_e as: $n_e = \frac{N_e}{\frac{\pi}{4}D^2 d}$.

Note, certain limitations apply for the MRS technique. Firstly, the plasma object needs to be placed far enough from the radiating horn antenna to ensure phase-free electric field radiation along the length of plasma. Specifically, the plasma object needs to be placed at least $\frac{d^2}{\lambda}$ (≈ 0.3 cm at maximum in this study) away from the radiating horn antenna, where d is the gap distance between electrodes and λ is the microwave wavelength. Secondly, the receiving horn needs to be put at least 2λ away from the plasma object to ensure far field radiation (~ 6 cm). In this study, both radiating and receiving horn antennas were placed 10 cm away from the plasma sample to meet the requirements above. Furthermore, the plasma diameter needs to be smaller than the skin layer depth to prevent shielding and ensure a uniform E-field distribution across the plasma

channel. For conditions of this experiment (plasma channel with ~300 μm diameter), the upper limit of the n_e that a 10 GHz RMS system can measure is around 10^{16} cm^{-3}. Lastly, the elongated shape of the plasma channel eliminates depolarization effects and allows considering E-field inside the plasma channel to be equal to that in the incident wave. [36]

3.1.4 Results and Discussion

3.1.4.1 Discharge Regimes

Two different discharge regimes were observed in this work: spark and corona. The experiments were conducted in ambient air at p=1 atm and transition between the spark and corona regime was observed by adjusting the gap distance between electrodes d. Smaller discharge gaps (d < 6 mm) were associated with spark regime, while larger ones (d > 8 mm) – with corona regime. Discharges at the gap distance of 7 mm were unrepeatable, occurring either as spark or corona and, therefore, experimental data for d = 7 mm was excluded from the analysis.

One can distinguish between the two regimes evaluating discharge voltage(V), current(I), energy deposition, total electron production, visual images from ICCD camera, etc. Figure 3-2 is an example of the *V-I* waveforms for corona, spark, and no-discharge case. One can see that the *V-I* waveforms of the corona discharge are very similar to the one without any discharge. This is due to the fact that electron number density of the plasma created is relatively low in corona regime, and conductivity of the gas between the electrodes is fairly small. This results in a current (< 2A) almost the same as displacement current flowing through the capacitor formed by the discharge electrodes without any discharge. Whereas for spark discharge, a highly conductive plasma channel is built, resulting in a sudden drop of the voltage between electrode, as well as a very high level of discharge current (> 10 A).

Visual observation of the discharge reveals the following difference between the discharge regimes. It was observed that the corona (d > 8 mm) consists of multiple transient streamers that are constantly igniting, dying out, and randomly moving between the electrodes. Set of initial ICCD images exposing first few nanoseconds after the breakdown is indicative of cathode-directed streamer initiated from the anode with ionization front propagating at about 1 mm/ns. Note, for corona discharge of stronger intensity (observed at smaller gap ~8 mm), one may observe with a naked eye (or if photographed with long exposure time) the discharge appearance similar to that

of the glow discharge. [26] Temporally-resolved photography indicates that plasma volume is still comprised of the large number temporally and spatially evolving streamers. On the contrary, one can see from the ICCD photography in Figure 3-2(c) that plasma channel in spark regime (d < 6 mm) was a single, thin, and highly-luminous (about 6 times more intense than corona) filament connecting the electrodes. The breakdown with d < 6 mm gaps was occurring almost instantly, faster than 3 ns (maximal temporal resolution of the ICCD camera used in this work), which suggests involvement of a very fast breakdown mechanism (substantially faster than a streamer breakdown observed at larger gaps d > 8 mm). (Note, for plane-parallel geometry, range of $p \cdot d$ < 200 Torr·cm is associated with Townsend breakdown mechanism of avalanche multiplication, while $p \cdot d$ > 4000 Torr·cm is corresponding to streamer breakdown mechanism. [18]) In this work the streamer breakdown was observed for the gap distance above ~ 7 mm ($p \cdot d \geq 500$ Torr·cm), while smaller $p \cdot d$-values were associated with even faster breakdown mechanism than streamer or Townsend breakdown. Those extremely fast breakdowns can be referred to the mechanisms described in more details in Refs. [18] [105] [106].

Table 1 below summarizes main discharge properties of the two regimes observed in this work and each of them is described in detail in the sections below.

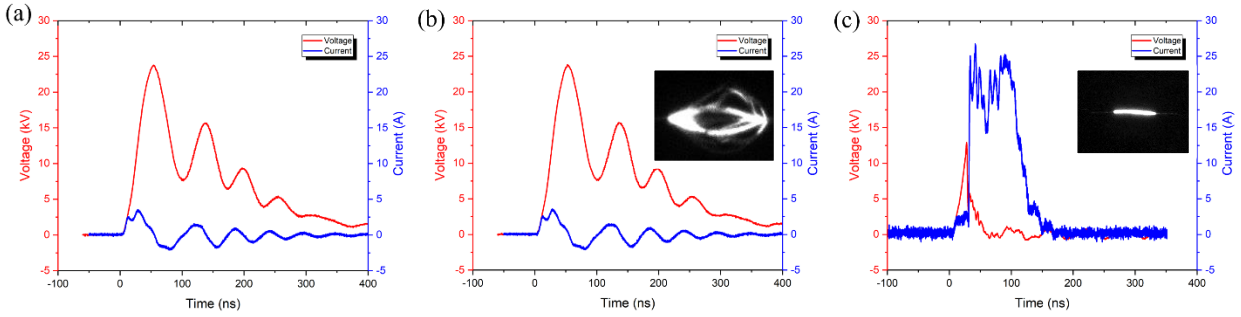

Figure 3-2. V-I waveform of a pulse: (a)without breakdown with dielectric between electrodes; (b) in corona regime at 10 mm; (c) in spark regime at 2mm. ICCD images for corona and spark regime are also presented to the side of the V-I curve for each regime.

Table 1. Summary of the discharge properties in the two regimes observed in this work: spark ($d \leq 6$ mm) and corona ($d \geq 8$ mm).

Regime	Gap distance d, mm	Breakdown voltage V_{br}, kV	Peak current I_{peak}, A	Energy deposition, mJ	Total electron production, $(N_e)_{max}$	Gas temperature T_{gas}, K	Light emission
Spark	2 - 6	< 22	> 10	> 2	$> 1 \cdot 10^{12}$	> 1000	Single thin plasma channel; intense light emission
Corona	≥ 8	~ 25	< 2	< 1.5	$< 3 \cdot 10^{11}$	< 100	Multiple streamers; weak light emission (6x weaker than spark)

3.1.4.2 Spark Regime

3.1.4.2.1 Typical discharge parameters

Figure 3-3 is an example of the temporal evolution of voltage V, current I, n_e, T_{rot}, T_{vib} of a spark discharge at d = 5 mm. One can see that spark breakdown occurred at a voltage of around 19 kV and $t \approx 26$ ns as indicated by a quick drop of the interelectrode voltage to 5-10 kV range, current peak of approximately 17 A, and creation of electrons in the gap with average number density to about $n_e = 1.5 \times 10^{15}$ cm^{-3}. Additionally, one can observe the second breakdown event (BD2) occurs at around $t \approx 70$ ns. It is indicated by a further quick drop of the voltage to less than 1000 V, second current peak of about 17 A, and additional increase of n_e to about 5×10^{15} cm^{-3}. BD2 is likely triggered by the increase of electric field in cathode vicinity which is expected due to constant removal of electrons to anode to support the discharge current conduction and corresponding buildup of positive ion charge on the cathode-facing side of plasma column. Thus, BD2 is potentially associated with cathode sheath breakdown, ignition of a cathode spot, and transition of the discharge to cathodic arc regime. [18] [107] This stage of the discharge is expected to be destructive for the electrode assembly due to erosion of cathode material from the cathode spots.

Figure 3-3 also shows temporal evolution of $T_{rot}(=T_{gas})$ and T_{vib}. One can see that T_{gas} increased from room temperature to around 1750 K at the time of 80 ns. T_{vib} increased from 4000 K to 10000 K within the same time frame. The temperatures cannot be measured by OES technique beyond t = 80 ns due to the lack of the SPS emission at these times. This can be explained by reduction of local reduced field E/n_g (where E - electric field strength; n_g –gas number density). Specifically, the reduced fields $E/n_g > 10^{-15}$ V·cm^{-2} are required for the efficient pumping of the

electronic excitations, vibrations, and ionization of O_2 and N_2, whereas efficiency of these transitions decreases for the lower reduced fields. [18] A quick estimation of the reduced field in current experiment indicates that E/n_g drops below 10^{-15} V·cm^{-2} already 20 ns after the discharge initiation (neglecting voltage drop in the cathode sheath).

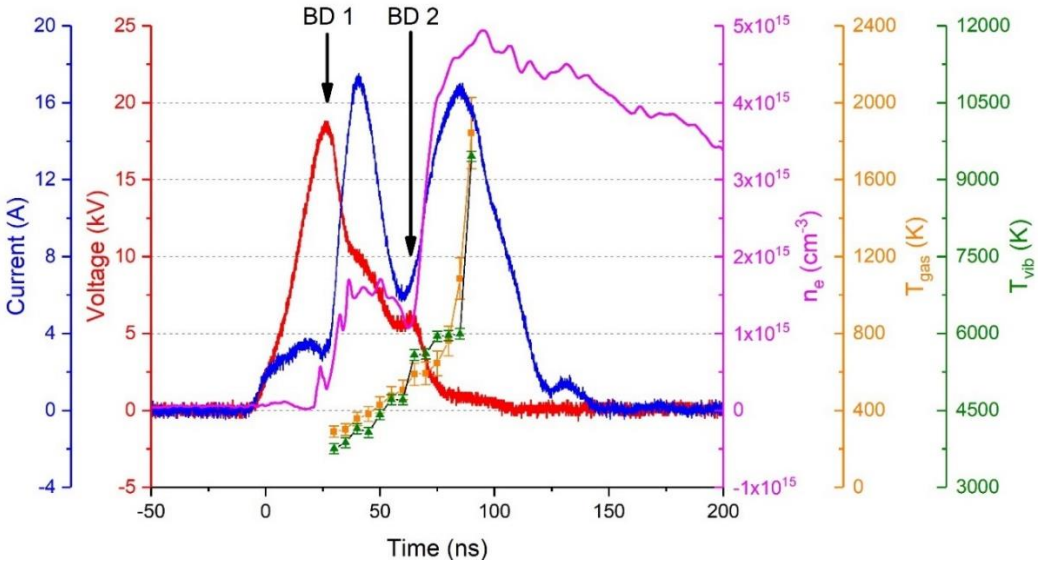

Figure 3-3. Temporal measurement of discharge parameters within the pulse at d = 5 mm. Moments of two breakdowns (BD) events are also labeled.

The temporal evolution of gas temperature after the ns-discharge was measured by implementing the probing pulse method [78] and presented in Figure 3-4. Note, the earliest measurement of T_{gas} was conducted at t =10 μs which is limited by the highest repetition frequency of 100 kHz that the pulser can produce. The gas temperature measured at t=10 μs is significantly higher than the maximum temperature during the pulse (3500 K vs. 1750 K as shown in Figure 3-3), indicating that the gas underwent further heating after t>100ns. This additional heating is mainly due to the vibrational relaxation of excited species (mainly N_2) which lasts for several microseconds. [24] T_{gas} reduces to the room temperature in about 1 ms after the ns-discharge.

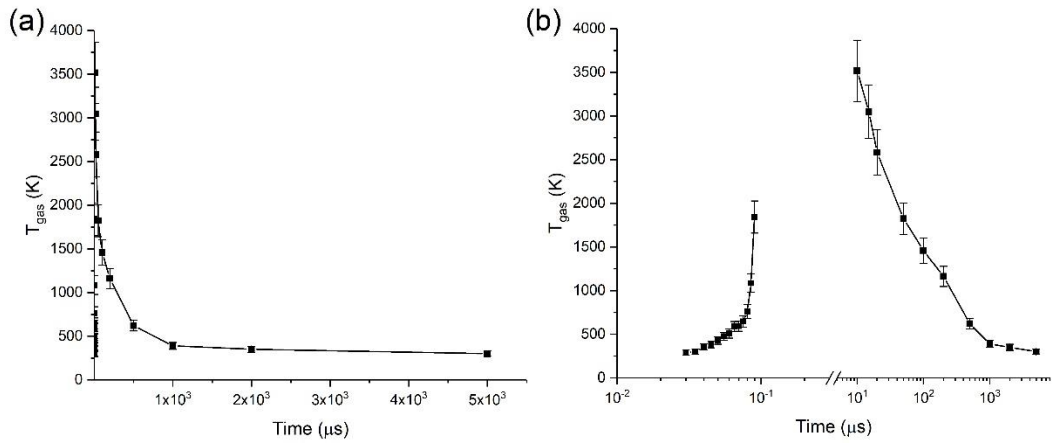

Figure 3-4. Temporal evolution of gas temperature T_{gas} within the pulse and post-discharge. (a) linear scale; (b) log scale

Temporal evolution of relative gas density n_g/n_{g0} measured at the center of electrode gap (where n_{g0} represents the gas density at standard atmospheric condition ~2.5×10^{19} cm^{-3}) is plotted in Figure 3-5(a). Figure 3-5(b) and (c) presents n_g/n_{g0} profiles measured by LRS in the radial direction at the midpoint between electrodes (1-5 μs, and up to 1 ms post-discharge, respectively). It can be seen that n_g drops to 30% of ambient level within approximately the initial 1μs post-discharge, stays constant for about 50 μs, and recovers to ambient level in the next 1 ms. Additionally, one can observe a pressure wave propagating outward at a speed of approximately 500 m/s according to Figure 3-5(b).

Note, LRS signal is overlapped with Thomson and Raman scattering; however, their contribution to the total signal is expected to be small in comparison with Rayleigh signal if plasma ionization degree is low ($n_e < 5\times10^{15}$ cm^{-3}). [103] Additionally, interpretation of measured scattered signal may be affected by dissociation of oxygen. [85] [88] [89] [90] Considering an extreme case of complete oxygen dissociation, one may expect LRS measurement error of about 15%, [103] and, in this work, we have accounted for the possibility of oxygen dissociation via corresponding error bar. It has to be noted, that one should expect a substantially lower dissociation degree in conditions of our experiments given that 30% dissociation was reported for ns-discharges with significantly larger discharge pulse energy of 20 mJ. [87]

The temporal evolution of the plasma diameter/volume was estimated visually from line-of-sight ICCD images, and the results are shown in Figure 3-6. One can see that the diameter of the plasma channel increases from around 250 μm up to 0.9 mm within the first 10 μs and then

stays approximately constant until fully decays. The separation of the shock wave front and the expansion of heated plasma core was thus observed according to different velocity estimated from Figure 3-5 and Figure 3-6. [31] A curve smoothly connecting data points for n_g and plasma diameter were used as an input for evaluating N_e and n_e using equation (1). Abel inversion was also done for multiple raw ICCD images, which have shown very minor effect (within 5%) on the plasma diameter estimation. Finally, plasma diameter was evaluated from raw line-of-sight ICCD images and potential error were accounted via corresponding uncertainty bars shown in Figure 3-6(a).

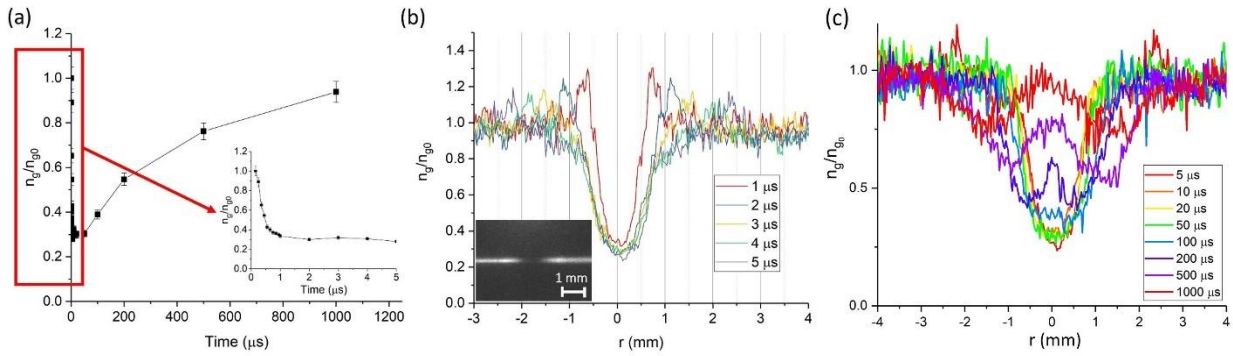

Figure 3-5. (a) Temporal evolution of ng measured by LRS. Radial profile of the relative density perpendicular to the plasma filament for (b) t = 1-5 μs after discharge, (c) 5-1000 μs after discharge.

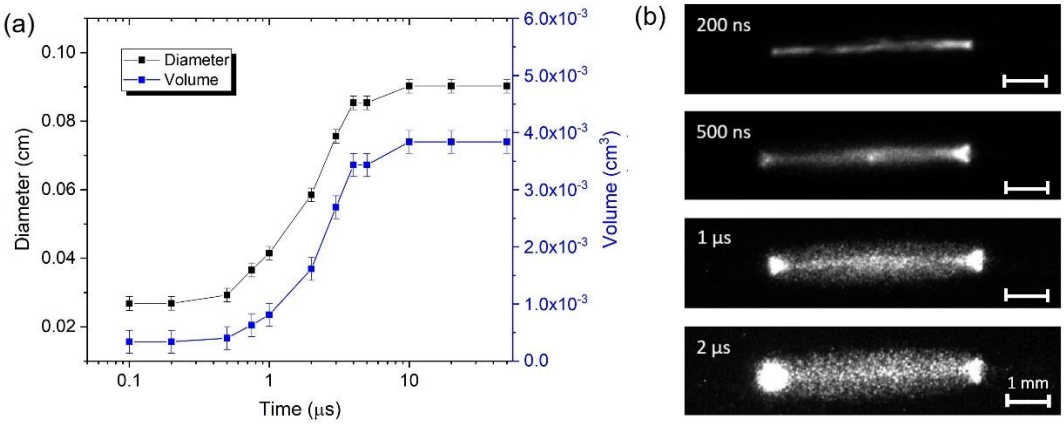

Figure 3-6. (a) Temporal evolution of plasma diameter and volume. Black: diameter; blue: volume. (b)ICCD image of the plasma.

The temporal evolution of N_e and n_e is presented in Figure 3-7. The results are calculated using equation (1) with the input data of U_{out}, v, and V using procedure outlined in more details in Ref. [103]. (The collisional frequency v was determined via local gas density n_g measured by LRS.) As one can see in Figure 3-7, the characteristic decay time of n_e was about 150-200 ns. This corresponds to decay rate obtained is approximately (0.5-0.7) $\times 10^7$ s^{-1} which is about order of magnitude smaller than that reported for atmospheric pressure conditions earlier (0.76×10^8 s^{-1}). [92] [18] To understand this discrepancy we will analyze the decay using simplest model considering dissociative recombination and three-body attachment to oxygen reactions as follows: $\frac{\partial n_e}{\partial t} = -\beta n_e^2 - \nu n_e$. This equation was modeled numerically using measured n_g evolution, dissociative recombination of oxygen ions ($e + O_2^+ \rightarrow O + O$) and three-body attachment to oxygen ($e + O_2 + O_2 \rightarrow O_2^- + O_2$ and $e + O_2 + N_2 \rightarrow O_2^- + N_2$) reactions with the following rate coefficients: $\beta = 2 \times 10^{-7} \times \frac{300}{T_e}$ [cm^3s^{-1}]; $k_1 = 1.4 \times 10^{-29} \times \frac{300}{T_e} \times \exp\left(-\frac{600}{T_{gas}}\right) \times \exp\left(\frac{700\times(T_e - T_{gas})}{T_e \times T_{gas}}\right)$ [cm^6s^{-1}], $k_2 = 1.07 \times 10^{-31} \times \left(\frac{300}{T_e}\right)^2 \times \exp\left(-\frac{70}{T_{gas}}\right) \times \exp\left(\frac{1500\times(T_e - T_{gas})}{T_e \times T_{gas}}\right)$ [cm^6s^{-1}] , and $\nu = k_1 n_{O_2}^2 + k_2 n_{O_2} n_{N_2}$. [108] A very important parameter of this modeling is electron temperature (T_e). The electron temperature is expected to be close to vibrational temperature of nitrogen in the afterglow phase, suggesting T_e ~ several thousand K during first few microseconds right after the discharge pulse [87]. At the same time, a reasonable agreement between the model and measurements for the initial portion of the electron decay (t < 500 ns) requires assuming higher values of T_e (gas temperature in the range T_{gas}=2000-4000 K was utilized based on the measurements). Specifically, T_e =1 eV and 3 eV yield decay times of 30 ns and 80 ns, respectively. The observed discrepancy in the electron decay time can be potentially attributed to inaccuracies in rate coefficient approximations (note, the above approximations for the reaction rate coefficients were proposed for cold vibrationally unexcited gas T_{gas} < 500 K [108]) and inability to spatially resolve the decay of the dense spark core by the MRS technique. (It is also worth noting, that recent measurements conducted using laser Thomson scattering technique indicate anomalously slow T_e decay from ~ 3 eV right after the discharge pulse to ~ 1 eV at 1 μs after the discharge pulse, for 55 ns FWHM and 8 mJ discharge pulse [91].) Additionally, the obtained results indicate that the initial stage of the decay (up to t ~ 1-2 μs) is likely to be governed by comparable contributions of both dissociative recombination and attachment to oxygen

mechanisms, while the later stage of the decay is expected to be dominated by the attachment to oxygen.

To summarize, the reduction of local gas number density at the spark location right after the ns-discharge pulse is an important factor contributing to the anomalously slow electron decay observed in the experiments (~150 ns). Precise knowledge of electron temperature dynamics along with exact reaction rate coefficients are also required for correct decay interpretation.

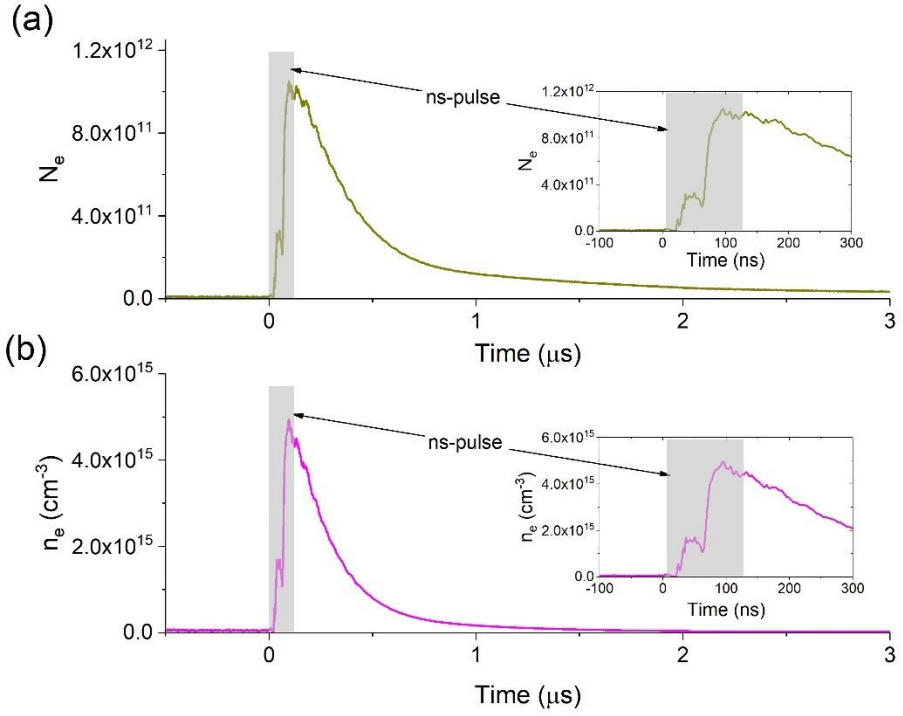

Figure 3-7. Temporal evolution of N_e (top) and n_e (bottom). The insert images indicate first 300 ns of the discharge in detail. The grey area represents the duration of the ns-pulse.

3.1.4.2.2 Effect of pulse energy on discharge parameters

Let us now investigate how the ns-pulse energy affects the discharge parameters in the spark regime (d=5 mm). In this study, the amount of energy deposition to the discharge was controlled by adding current-limiting resistors in series to each discharge electrode. The energy per pulse was calculated by integrating the product of voltage measured across the interelectrode gap and current over the whole pulse time. By adjusting the current-limiting resistors between R_{CL}=0, 200, and 400 Ohm, the energy deposition per pulse was measured to be $\mathscr{E}_{tot}$=5.04 (± 0.14), 3.76(± 0.10), and 3.07 (± 0.08) mJ, respectively. Temporal evolution of discharge parameters

including voltage, reduced field (neglecting voltage in cathode sheath), current, energy, temperatures (gas/rotational, vibrational), N_e, and n_e are presented in Figure 3-8 for the duration of the ns-pulse. Note, temporal evolution of gas density n_g was not presented but assumed to be the same as ambient level for the first 150 ns of the discharge as suggested by the LRS measurement which will be shown later.

One can see from Figure 3-8(a) that, the initial breakdown voltage is approximately the same for all three cases at around 18 kV. This is due to the fact that prior to breakdown the capacitive impedance of air gap between the electrodes is substantially larger ($\sim\tau$/C=2.5 kΩ, where $\tau\approx$10 ns – characteristic time of voltage rise and $C\approx$4 pF- capacitance of the electrode) than the resistance of the current-limiting resistors used. Thus, before the breakdown, the impedance seen by the pulser is not changing significantly by introducing different current-limiting resistors. Therefore, similar voltage rise (within 10% of difference) is generated by the pulser regardless of the R_{CL} value and the voltage is applied almost entirely to the interelectrode gap. Correspondingly, energy stored in the capacitor formed by the electrode assembly prior to the breakdown (until t~26-30 ns) is very similar for all three R_{CL} values used, ~0.64±0.03 mJ, as seen from Figure 3-8(d).

On the contrary, the shape of the voltage pulse differs more substantially after the breakdown (at t~26-30 ns) for different discharge pulse energies used. This is caused by the more comparable range of impedances of the plasma and current-limiting resistors. Indeed, after the breakdown, a highly-conductive/low-resistive plasma channel is formed filling up the gap between the electrodes (~600-1000 Ohm after the initial breakdown and then dropping to <120 Ohm after the second breakdown based on the waveforms shown in Figure 3-8(a) & (c)). Clearly, comparable range of utilized R_{CL} to that of the plasma channel is achieved after the breakdown. This makes adjustment of R_{CL} an efficient way to redistribute the ns-pulse energy between the discharge and the current-limiting resistors. Specifically, utilization of larger R_{CL} causing larger fraction of the energy to be deposited in the current-limiting resistor and less in the discharge.

One can also observe in Figure 3-8(a)(b) &(c) a substantially delayed BD2 moment for lower pulse energies while interelectrode voltage just prior to BD2 was very similar level ~6 kV regardless of the discharge pulse energy. Specifically, BD2 occurred at 65 ns, 75 ns, and 82 ns for the pulse energies 3.07mJ, 3.76 and 5.04 mJ, respectively. This can be explained by larger discharge currents generated at lager pulse energies and, therefore, faster removal of electron charge from the plasma column. This in turn causes corresponding quicker buildup of ion charge

on the cathode-facing side of the plasma column and growth of electric field to the level sufficient for breakdown of the cathode sheath.

Figure 3-8(e)&(f) show the temporal evolution of T_{gas} (= T_{rot}) within the nanosecond pulse. It can be seen that gas heating is more rapid and more substantial with the increase of discharge pulse energy. Indeed, T_{gas} reached 1000 K in 70 ns, 95 ns and 100 ns for the pulse energies 3.07 mJ, 3.76 mJ and 5.04 mJ, respectively. Maximal temperature measured within the pulse is also higher for higher discharge pulse energy. Note, the window of detectable SPS spectrum within the pulse expanded for lower discharge pulse energy which allowed extending T_{gas} measurements longer in the ns-pulse.

Temporal evolutions of N_e and n_e within the duration of ns-pulse are presented in Figure 3-8(g)&(h). One can see that number of electrons in the gap after the initial breakdown BD1 (at t~26-30 ns) increased with ns-pulse energy. Specifically, deposition of approximately 1.5 mJ (observed for $\mathscr{E}_{tot}$ =3.07 and 3.76 mJ) led to establishment of quasi-steady-state electron number N_e=1.9×10^{11} and electron number density n_e=1×10^{15} cm^{-3} (at t ~ 40-60 ns) while energy deposition of ~2 mJ ($\mathscr{E}_{tot}$=5.04 mJ) yielded N_e=3.0×10^{11} and n_e=1.6×10^{15} cm^{-3}. This of quasi-steady-state period of the discharge (t ~ 40-60 ns) is likely associated with balance between the electron production in the discharge volume ($\alpha V_{dr} N_e$, where α – ionization coefficient, V_{dr} – electron drift velocity) and electron removal to the anode ensuring conduction of the discharge current ($I/|e|$; I ~10A at t~50 ns). This balance yields α/n_g~10^{-18}-10^{-19} cm^2 and reduced field of the order of E/n_g~100-150 Td which is fairly consistent with the estimation based on measured discharge voltage. [109] Later breakdown of the cathode sheath (BD2) results in significant (about 5-10 times) drop of voltage (from about 6 kV before BD2 to about 500-1000 V after BD2). Corresponding substantial decrease of E/n_g-value nearly stops the electron production inside the plasma volume due to sharp reduction of ionization coefficient with E/n_g- decrease (e.g., ionization coefficient drops 100 times when E/n_g reduces from 100 to 60 Td). [109] Instead, electron number and electron number density are governed by production of electrons in cathode spot vicinity, their transport through the gap and collection at the anode. This stage of discharge largely resembles conventional cathodic arc and would be converted into DC cathodic arc if voltage is kept at the electrodes.

For all used discharge pulse energies, majority of the energy was deposited to the interelectrode gas at around and right after the time of initial breakdown BD1, while second

breakdown (and transition to cathodic arc) is associated with just incremental further energy deposition. Specifically, around 85-89% of pulse energy was deposited into gas before the BD2, while only 11-15% were deposited after BD2. This shows that fast ns-discharge is substantially more efficient way to deposit energy to the interelectrode gas in comparison with cathodic arc.

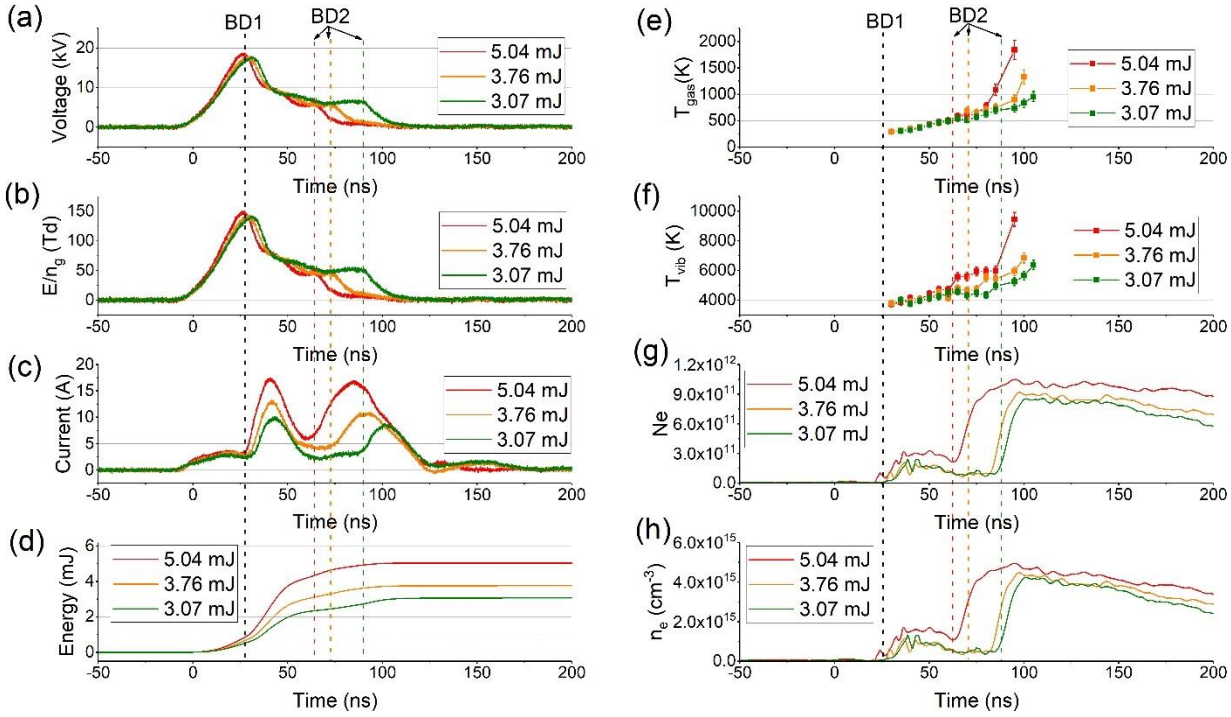

Figure 3-8. Temporal measurement for different energy deposition. (a) voltage; (b) reduced field; (c) current; (d) energy; (e) gas temperature; (f) vibrational temperature; (g) total electron number; (h) electron number density

Complete temporal evolution of gas temperatures measured by OES and OES enhanced with probing pulse for three discharge energy levels are presented in Figure 3-9. It can be seen that the maximal temperature of 3500 K was measured for 5.04 mJ pulse energy in comparison with 3000 K for 3.07 mJ at t =10 μs. In addition, T_{gas} after the ns-pulse reduced faster for higher pulse energies until about 100 μs and then temperature decay curves collapsed to the same one for all discharge pulse energies recovering back to room temperature at about 1 ms. [78] This faster initial temperature decay for higher E_{tot} is potentially due to generation of stronger vortex rings and thus a more intensive air mixing/cooling when larger energy is deposited. [110] [111] [112]

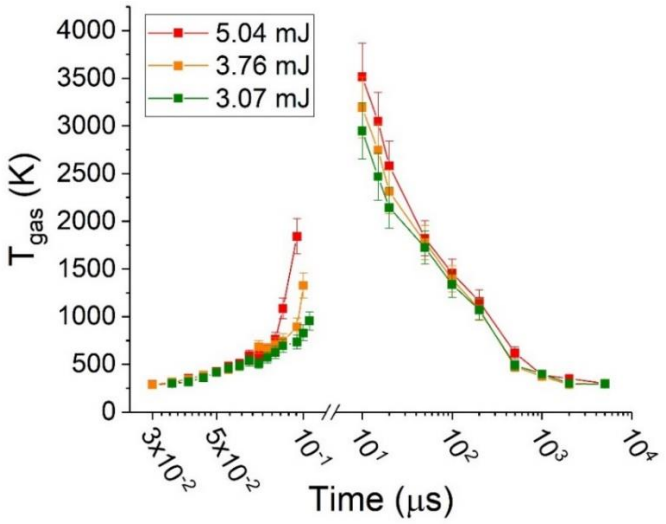

Figure 3-9. Temporal evolution of T_{gas} for different energy deposition within and after the HV pulse.

Temporal evolution of the relative gas density (n_g/n_{g0}) measured by LRS for different discharge pulse energies is presented in Figure 3-10(a). A more detailed plot of the initial dynamics of n_g/n_{g0} (for t < 5 μs) along with the temporal evolution of plasma diameter estimated from ICCD images is shown in Figure 3-10(b). A similar behavior of n_g/n_{g0} for all three discharge pulse energies was observed starting with fast initial drop within 1μs post-discharge, remaining nearly constant for about 10s of μs, and recovering to ambient level in the next 1 ms. More significant reduction of gas density was found for higher discharge pulse energy; specifically, air density dropped to 55%, 50%, 30% of ambient air density level for the discharge pulse energies of 3.07 mJ, 3.76 mJ, 5.04 mJ, respectively. It can be also seen that plasma channel had very similar diameter regardless of the pulse energy level early on (t < 500 ns) while it expanded wider for higher pulse energy (650 μm for 3.07 mJ and 900 μm for 5.04 mJ).

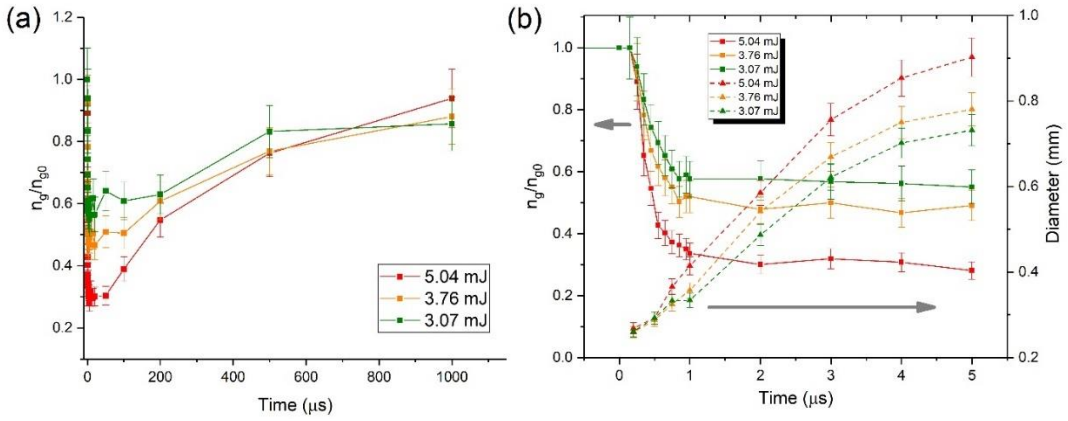

Figure 3-10. (a) Full temporal evolution of relative gas density for different energy deposition. (b)Temporal evolution of gas density and plasma diameter post-discharge for different energy deposition within the first 5 μs. Solid line + square; relative gas density; dash line + triangle: plasma diameter.

Complete temporal evolution of N_e and n_e are plotted in Figure 3-11. It can be observed that, the temporal decay of n_e is elongated with increase of the pulse energy. This is due to higher T_e achieved and more substantial n_g drop with higher pulse energy as described above in section 2.1.

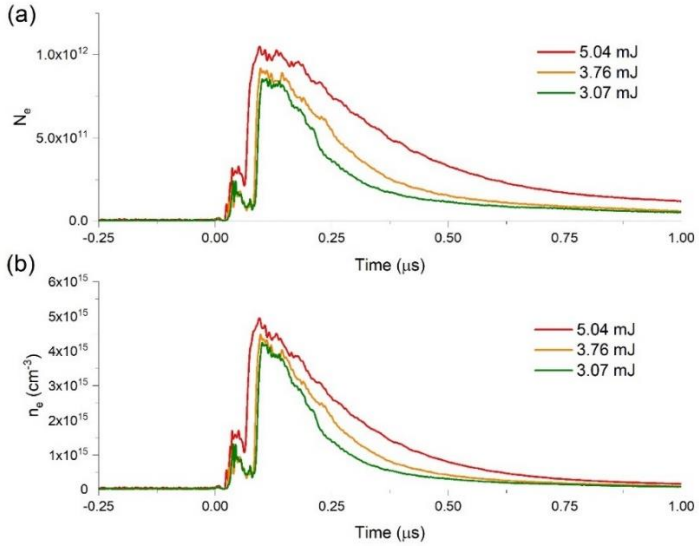

Figure 3-11. Temporal evolution of N_e and n_e for different energy deposition. (a) N_e; (b) n_e

3.1.4.2.3 Effect of gap distance on discharge parameters

Let us now investigate the effect of interelectrode gap distance d on the discharge properties in spark regime. Temporal evolutions of discharge properties for d = 2, 4, 6 mm are presented in Figure 3-12 including voltage, reduced field - E/n_g (neglecting voltage in cathode sheath), current, discharge pulse energy per unit gap - E/d, T_{gas}, T_{vib}, N_e, and n_e. As one can see from Figure 3-12(a), the initial breakdown (BD1) of smaller gaps occurred at a lower voltage, while at higher reduced field. Indeed, as shown in Figure 3-12(b), E/n_g at the moment of breakdown were 140, 160 and 260 Td for d =6, 4 and 2 mm, respectively. Additionally, the breakdown in smaller gaps occurred in more abrupt fashion generating higher discharge peak currents as shown in Figure 3-12(c). This correspondingly led to faster energy deposition per unit gap distance (E/d) as shown in Figure 3-12(d) and caused faster gas heating which is confirmed by T_{gas} measurements in Figure 3-12(e). Higher discharge currents in smaller gaps led to earlier breakdown BD2 associated with ignition of cathodic spot which is consistent with the results reported in the previous section. Interestingly, the total energy input per gap $\mathscr{E}_{tot}/d$ was rather consistent 1 mJ/mm for all tested gap sizes. Larger E/n_g observed in the smaller gaps resulted in shifting the balance conditions (between electron production in the discharge volume and electron removal to the anode to support current conduction) toward production of higher electron number density and higher discharge current which agrees with the experiment. The effect of gap distance on V_{br}, $(E/n_g)_{br}$, I_{peak}, $\mathscr{E}_{tot}$, $\mathscr{E}_{tot}/d$, n_e, N_e (quasi-steady-state values after BD1 are provided) is summarized in Figure 3-13.

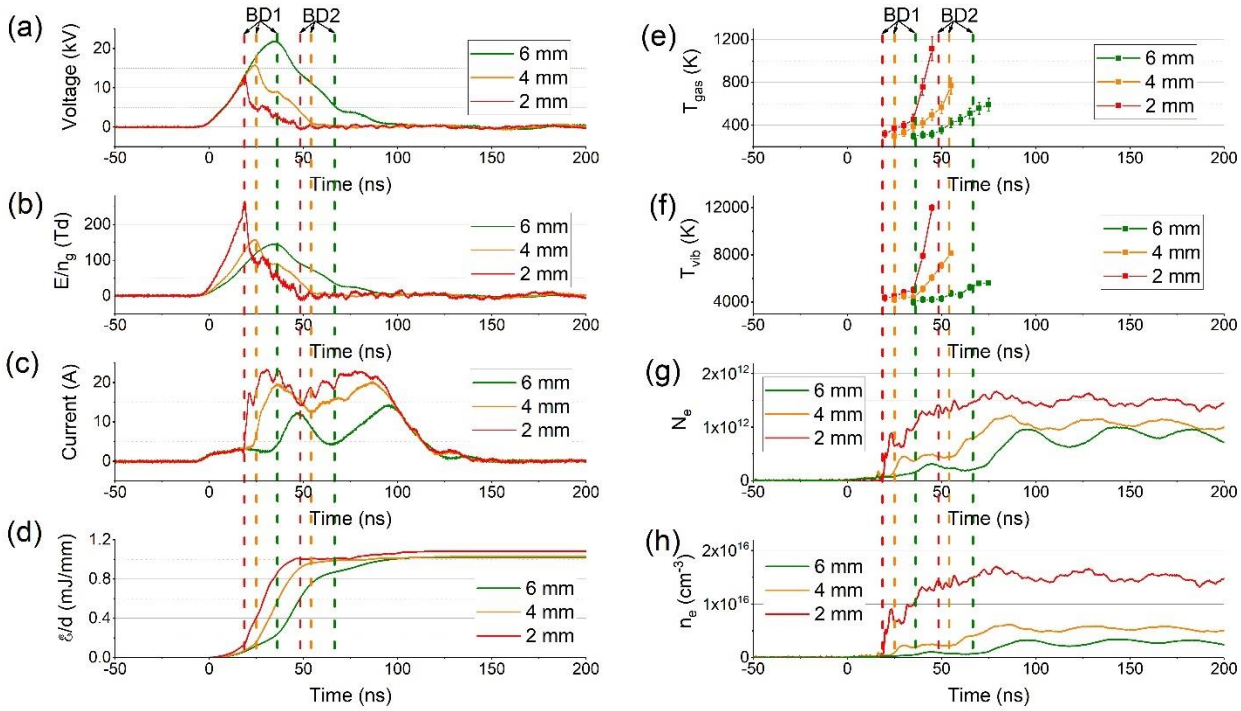

Figure 3-12. Temporal evolution of (a) voltage; (b) reduced field; (c) current; (d) energy; (e) gas temperature; (f) vibrational temperature; (g) total electron number; (h) electron number density for d = 2, 4, 6 mm

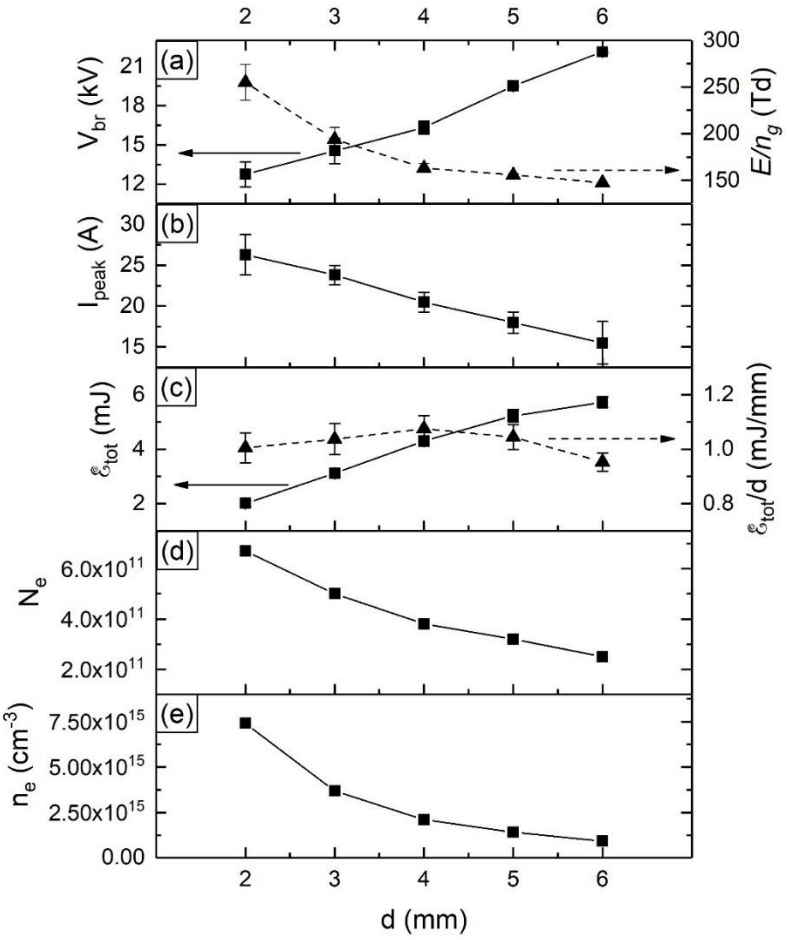

Figure 3-13. (a) voltage and reduced field at breakdown, (b) Peak value of current, (c) Energy input and energy input per unit length with respect to gap distance from 2 to 6 mm. (d) N_e after BD1, (e) n_e after BD1 with respect to gap distance from 2 to 6 mm.

The complete temporal evolutions of T_{gas} for d = 2, 4, 6 mm are presented in Figure 3-14. One can see that the cooling rate of T_{gas} at smaller gaps was faster than for the larger gaps. This can be potentially explained by a faster removal of hot gas between the electrodes when stronger vortex rings are formed in smaller gaps. [110] [111] [112]

Summarizing measurements of plasma parameters after ns-discharge pulse for tested pulse energies (0.6-1 mJ/mm) and gap sizes (2-6 mm), we conclude that complete recovery of parameters to their unperturbed pre-discharge values occurs at ~ 1 ms after the discharge pulse (see Figure 3-4, Figure 3-5, Figure 3-9, Figure 3-10 and Figure 3-14). One can thus expect memory effects to occur at a repetition frequency >1 kHz. Note, the 'cut-off' frequency indicating onset of memory effects and transition from single pulse ns-discharge regime to NRP operational regime depends

on many factors, including ambient temperature, pressure, pulse energy and shape, gas composition, electrode geometry. Study of NRP regime using the diagnostics complex created in this work will be subject of future work.

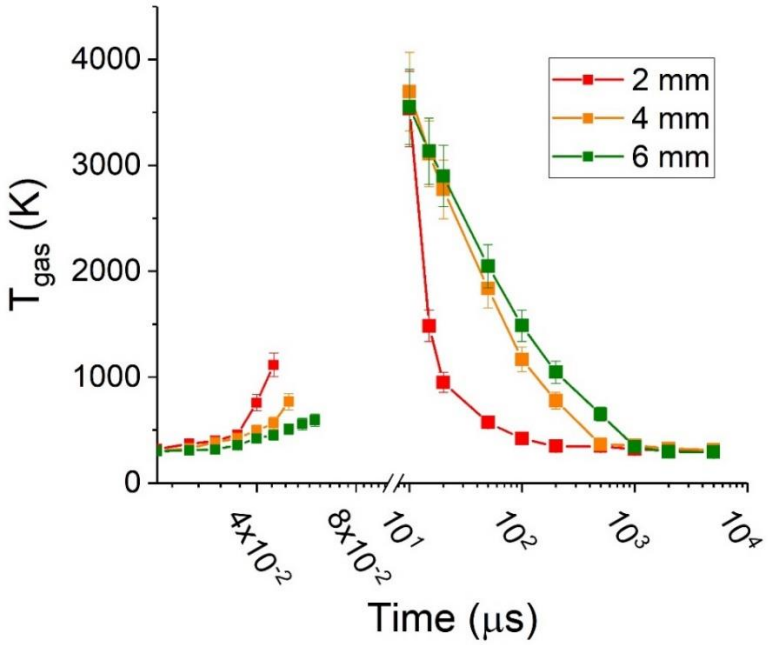

Figure 3-14. Temporal evolution of T_{gas} for d = 2, 4, 6 mm

3.1.4.3 Corona Regime and Comparison with Spark

Corona regime was studied for gap distances of 8, 9, and 10 mm. Voltage and current waveforms for d = 8 mm are shown in Figure 3-15. In comparison to *V-I* waveforms for the spark regime, it is noticeable that ignition of corona was not associated substantial voltage drops. On the contrary, voltage waveform was similar to one observed without breakdown (see Figure 3-2) with pulse duration larger than that set on the pulser (90 ns) and with voltage oscillations. This indicates that corona does not affect impedance of the interelectrode space substantially and pulser operates the entire time in mismatched conditions being loaded on 5 kOhm active resistance of the matching resistor stage shown in Figure 3-1. Total measured current (I) consists of two components - displacement and conduction currents. Displacement current can be calculated from $I_{disp} = C \cdot \frac{dV}{dt}$ using known capacitance of interelectrode assembly C=3.9 pF (determined from the experiments without breakdown). Finally, the conduction current can be determined as $I_{cond} =$

$I - I_{disp}$ and the results are shown in Figure 3-15(b). One can see that corona discharge current reached peak value of approximately 1.7 A at *t*~50-70 ns.

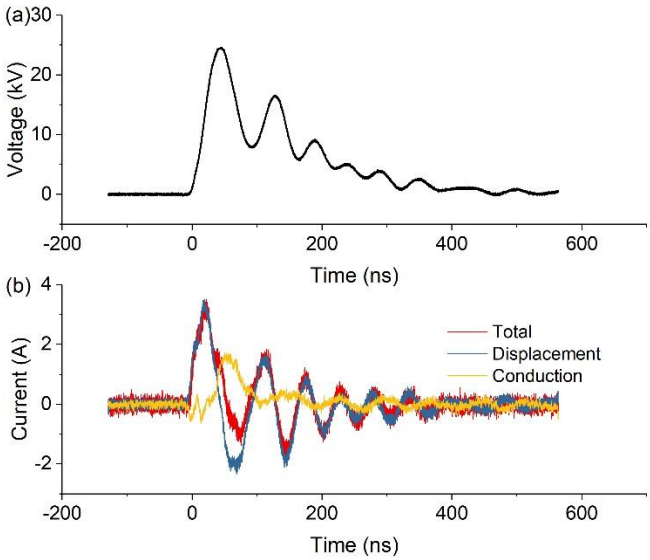

Figure 3-15. Temporal evolution of (a) voltage and (b) current for corona regime at *d* = 8 mm

The peak number of electrons ($N_{e,max}$) for *d*=8-10 mm are plotted in Figure 3-16 along with the corresponding peak values of I_{cond}. One can see that as *d* increases, the level of current decreases while the number of electrons produced increases. Both trends can be explained by the longer associated streamer path, and correspondingly larger resistance and number of electrons. Note, due to generation of multiple streamers between the electrodes and random path of each individual streamer confirmed using ICCD photography as shown in Figure 3-2(b), it was impossible to quantify the exact volume of the plasma channel, and, therefore, the value of n_e was not calculated. T_{gas} and T_{vib} temporally averaged over the discharge pulse duration were also measured over the ns-pulse using OES, and the results were 360 ± 20 K and 3700 ± 100 K, respectively for all three gap distances.

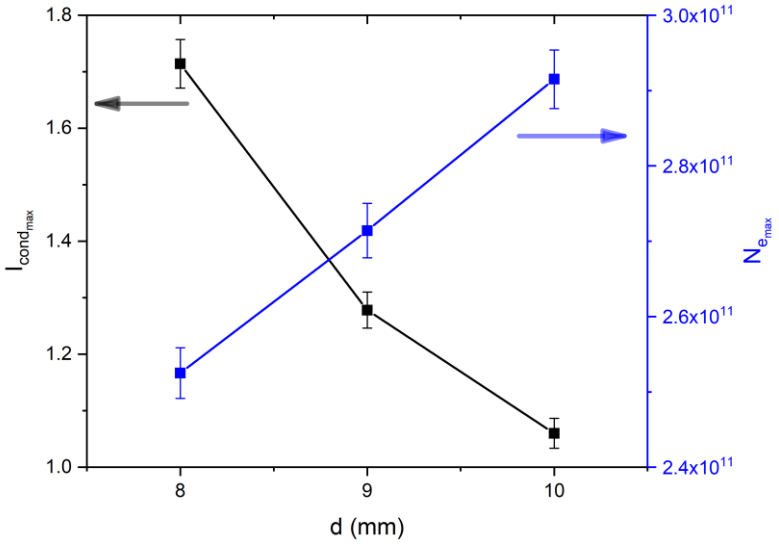

Figure 3-16. Dependence of conducting current and peak N_e on d for corona regime

Discharge parameters in two discharge regimes were further compared in Figure 3-17, including breakdown voltage, conductivity current peak current values, discharge pulse energy, and maximum number of electrons produced (during BD1 for spark regime). As opposed to spark discharges accompanied with abrupt and loud breakdowns, corona discharge was associated with milder and quieter operation. V_{br} increased up to nearly 25 kV for gaps d =8-10 mm as shown in Figure 3-17(a). Corona discharge was correspondingly associated with substantially lower conductivity current peaks and discharge pulse energies as shown in Figure 3-17(b) and (c). The discharge pulse energy unit gap distance was relatively constant within each regime: ~1mJ/mm for spark and ~0.1 mJ/mm for corona. One can see in Figure 3-17(d) that electron production increased for smaller gaps indicating higher ionization degree for lower gap distances.

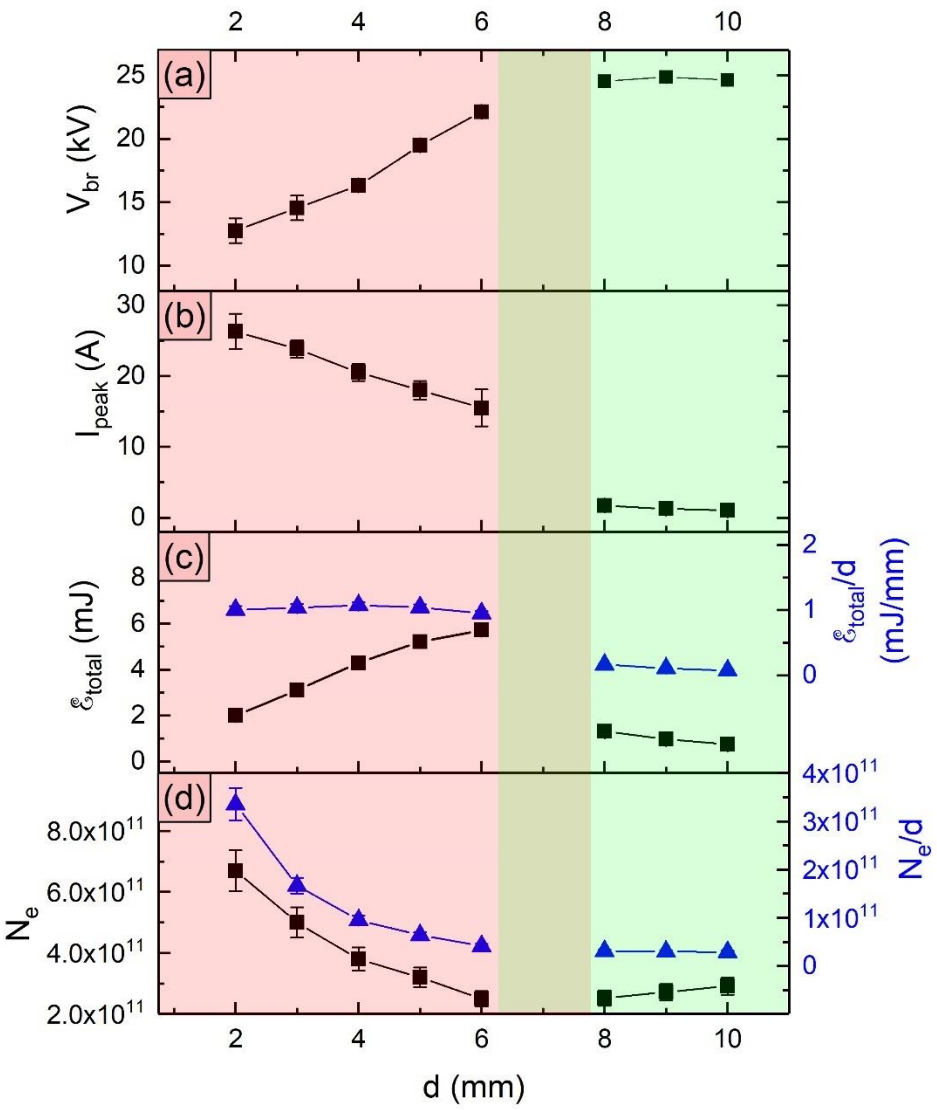

Figure 3-17. Discharge parameters vs d: (a) breakdown voltage. (b) peak current. (c) total energy input and energy input per gap distance. (d) total electron and electron per gap distance. Regime of spark and corona are colored by red and green background, respectively.

3.1.5 Conclusion

A comprehensive study of pin-to-pin nanosecond high-voltage discharge operating in single-pulse mode at atmospheric pressure indicate presence of spark and corona regimes. The spark discharge was associated with shorter gap sizes of (<6mm) and larger discharge pulse energy per mm of gap size (0.6-1 mJ/mm) in comparison with corona discharge observed at gaps (>8mm) and discharge pulse energy (~0.1 mJ/mm). Ultimate discharge parameters (e.g., highest electron

number density, gas temperature) can be achieved in spark regime using smaller electrode gaps and larger pulse energy. Conditions of the spark discharge after the breakdown are consistent with the balance between the electron production in the discharge volume and electron removal to the anode ensuring conduction of the discharge current and correspond to reduced field range ~100-150 Td. Limitation of the discharge pulse duration to 30-70 ns is necessary in order to prevent transition to cathodic arc regime. Comparison of experimentally measured and numerically simulated electron decay indicate that initial decay (up to t ~ 1-2 μs) is governed by comparable contributions of dissociative recombination and attachment to oxygen, while later stage is expected to be dominated by the attachment to oxygen. Based on the measured temporal evolution (and recovery) of gas number density and temperature, the onset of memory effects and associated transition to nanosecond repetitively pulsed (NRP) regime can be expected for repetition frequencies >1 kHz.

3.2 Experimental study of pin-to-pin nanosecond pulsed (NRP) discharges at atmospheric conditions with different pulsing frequency.

3.2.1 Abstract

In this work, nanosecond repetitively pulsed (NRP) discharges with pin-to-pin configuration at atmospheric condition were studied. The effect of repetition on the discharge parameters was investigated focusing on the transition process from single-pulse discharge to steady-state NRP operation. Repetition frequency from 1 kHz to 100 kHz was utilized. There has been shown no detectable memory effect at 1 kHz. For repetition frequency of 10 kHz, local gas temperature was measured above 1000 K and gas density drops to lower than 50% of ambient level. The electron number density was peaked at approximately 1.5×10^{15} cm^{-3} after 5 pulses however an optimal steady state operation was never reached due to the unstable pulse energy input from the pulser. For repetition frequency of 100 kHz, gas temperature was heated up to 5000 K and local gas density drops to lower than 10% of ambient value. The electron number density peaks at around 1.0×10^{15} cm^{-3} during steady state NRP operation after two pulses. A slower decay rate of electrons was also observed during the steady state operation in comparison with single-pulse condition, and the change of governing electron decay mechanism from a combination of dissociative recombination and three-body attachment to solely recombination was also expected.

3.2.2 Introduction

Nanosecond discharges (ns-discharges) have drawn great interest from people for its potential in a wide variety of applications. The ns-scale rise time allows the voltage to quickly increase beyond the required breakdown voltage (over-voltage), which enables a large production of active species as well as efficient energy deposition into a small volume [23]. Sending a series of ns-discharges at high repetition frequencies, which is defined as nanosecond repetitively pulsed (NRP) discharges, can thus be utilized as a source of certain kinds of gas species in applications such as assisting combustion (O, H, OH, etc.) [9] [10] [11]. Moreover, NRP discharges find its value in the field of aerodynamics as plasma actuator. The local heat-up on the airfoil surface caused by NRP dielectric barrier discharges (DBD) delays the separation of flow and ultimately reduces drag [13] [14]. NRP discharges have been also utilized in many other fields including medicine, nanotechnology, material processing, sterilization, etc. [1]

In the previous work [REF-single pulsed (SP)], ns-discharge with pin-to-pin configuration was studied at atmospheric conditions. For single-pulse ns-discharges, two discharge regimes were defined: spark and corona. Within the spark regime, the effect of different pulse energy and gap distance was further investigated, during which parameters such as gas density, temperature, electron number density were measured. It has been shown that single-pulse discharges with 5mm gap, 5 mJ energy deposition produce plasmas with electron number density of approximately 5×10^{15} cm^{-3} and characteristic decay time of approximately 150-200 ns. In addition, gas temperature was measured to be 3500 K at 10μs after the discharge; gas density was measured to be at a minimum of 30% of ambient value 5 μs after the discharge under the same condition. Both temperature and density recover to ambient condition within about 1 ms.

In that work, pulsing frequency was deliberately kept at 1 Hz to eliminate memory effect. For ns-discharges at high enough repetition frequencies, the change of air properties between electrodes may survive until the subsequent pulses and make the corresponding discharge's outcome very different. Conditions that may change include gas temperature/density, amount metastable/dissociated molecules, and even existing electron/ions. Accumulation of these changes of the properties finally reaches equilibrium with the rate of decay/recovery to ambient condition after certain number of pulses, and NRP discharge thereafter is operating at a steady-state. In the testing condition studied before [REF-SP], where both temperature and density recover in about 1 ms, one should expect memory effect to be prominent at repetition frequency higher than 1 kHz.

On the other hand, NRP pin-to-pin discharges operating at repetition frequency in the range of kHz have been studied by many groups. In the work by Pai and Rusterholtz et al. [32] [26] [27], NRP pin-to-pin discharges at 10-30 kHz was studied in a preheated air at 1000 K where the gap distance between electrodes was kept at 4-5 mm. With an energy input of <1 mJ, gas temperature was measured to be up to 5000 K, and the electron number density was on the order of 10^{15} cm^{-3}. In the work by Horst et al. [28], pin-to-pin NRP discharge was studied in N_2 and 0.9% humidified N_2. The discharge was set at a repetition frequency of 1 kHz at atmospheric temperature/pressure with a gap distance of 2 mm. The gas temperature was measured to be up to 750 K and the electron number density was measured to be on the order of 10^{18} cm^{-3} when the energy input per pulse is around 1 mJ. Moreover, an electron number density on the order of 10^{18} cm^{-3} was measured by Zhu et al. [30], where pin-to-pin discharge was operating in atmospheric pressure Argon (with 5% Neon) at 1 kHz with a gap distance of ~100 μm.

However, the works mentioned above are only focusing on the NRP discharges operating at steady state at certain frequencies. The dynamics of NRP discharge from pulse #1 until steady state were barely studied. In this work, the effect of the repetition frequency on the NRP pin-to-pin discharge at atmospheric conditions is investigated, focusing on the accumulation of memory effect during which the transient change of the discharge properties from single pulsed condition to the steady state operation of NRP is taking place. Properties such as gas density, temperature, pulse energy input, electron number density are traced from the initial pulse till steady state to provide insights on the pin-to-pin NRP discharges at various repetition frequencies.

3.2.3 Experimental setup

The experimental setup includes: HV nanosecond pulse (25 kV peak, 90 ns width) supply by a pulser (Eagle Harbor NSP-3300-20-F); voltage(V)/current(I) measurement by traditional voltage probes (Tektronix P6015A) and current transformer (Bergoz FCT-028-0.5-WB); gas temperature T_{gas} (= rotational temperature T_{rot} [78]) measurement by spectrometer (Princeton Instruments SP-2750i) and ICCD camera (Princeton Instruments PI-MAX 1024i) based on optical emission spectroscopy (OES) with nitrogen second positive system (SPS) spectra; gas density n_g measurement by laser Rayleigh scattering (LRS) (nanosecond laser pulses at 532 nm were supplied by EKSPLA NT342); and electron number density measurement based on microwave Rayleigh scattering (MRS) as well as LRS data. The detailed experimental setup is identical to the previous

work and can be referred in [REF-SP]. The gap distance between electrodes was kept at 5mm so that every single discharge is in the spark regime.

In addition, the pulsing frequency of the pulser *f* was controlled by an additional waveform generator. A standard TTL signal was sent from the waveform generator to the pulser through an optical fiber as the trigger signal. A jitter of approximately 250±100 ns was measured between the receiving of the trigger signal and generation of HV nanosecond pulse by the pulser. Although the jitter itself is considerably large and unrepeatable with respect to the nanosecond pulse, it is still within the tolerance on the scale of a burst considering the pulses are sent at minimum of 10 μs apart. A burst of 10-20 pulses were sent in every run of test where the repetition frequency *f* was chosen to be 1, 10 and 100 kHz. Each run of burst was separated at least 2 second for a full restoration of air between electrodes and cooling of the matching resistors of the pulser. Data including voltage, current, and microwave scattering signal was recorded in real time by an oscilloscope (Lecroy WavePro 735Zi, 3.5 GHz bandwidth, 40 GS/s sampling rate) throughout the whole period of the burst.

Two data points of gas temperature T_{gas} and bulk gas density n_g were recorded at certain number of pulses during the burst, which are pulse number 1, 2, 3, 4, 5, 10, and 20. One of the data points for T_{gas} on each pulse was recorded at the beginning of the ns-pulse representing the initial condition of temperature for the corresponding discharge. The second data point was recorded during the last 5 ns of visible SPS of N_2 window within the ns-pulse representing the highest measurable temperature during the discharge. The timing of the ICCD camera gate was controlled by the gate delay setting on its software (Lightfield).

Another waveform generator was utilized to trigger the laser pulse for n_g measurement with LRS technique at the desired moment. Laser pulses were sent: 1) right before the initiation of the ns-pulse for the measurement of initial condition of n_g of each discharge; and 2) 5 μs after the initiation of the ns-pulse which is assumed to be the moment with lowest gas density after discharge [103].

3.2.4 Results and discussion

The voltage and current measurements at three frequencies are shown in Figure 3-18 as 1) a burst of 10-15 pulses and 2) a single pulse at steady-state. As one can see from Figure 3-18a-1 that, breakdowns occurred randomly at voltage between 17 kV and 19 kV; peak current value is

approximately 18 A for every single pulse. The voltage/current waveform of a single discharge (pulse #10) is also shown in Figure 3-18a-2. In comparison with the V/I waveforms presented works [REF-SP] as the single-pulse case, it can be concluded that, from the perspective of discharge voltage/current, no memory effect exists at $f = 1\ kHz$, which is in agreement with our previous prediction. For $f = 10\ kHz$, one can see from Figure 3-18b-1 that, the breakdown voltage of pulse #1 is distinctively higher than the following pulses, peak current of pulse #1 on the other hand is lower than that of the following pulses. The breakdown voltage for the pulses # >2 is oscillating in the range of 6 kV to 13 kV where the peak value of current stays at round 20 A with a fluctuation of approximately 2 A. In comparison with the case $f = 1\ kHz$, one can clearly tell the existence of memory effect. However, the unsteadiness of the breakdown voltage and peak current implies a very random change of the memory effect induced per discharge over the burst. NRP discharge at $f = 10\ kHz$ is thus too random to be defined as an ideal steady-state even after many pulses. It is mainly due to the unsteady energy input at each pulse which will be discussed in more detail in the next paragraph. Figure 3-18b-2 presents a V/I waveform of pulse #12 at $f = 10\ kHz$. Despite the change in magnitudes, one can see that by increasing the repetition frequency, it takes less time till the transition to cathodic arc regime and the highly-conductive plasma channel fully bridging the gap between electrodes, which is presented as an earlier and less pronounced 2nd current peak (t~70ns) and a more boxcar-shape current waveform. Furthermore, for $f = 100\ kHz$, one can see from Figure 3-18c-1 that the breakdown voltage drastically decreases after the initial pulse. Starting from pulse #2, the breakdown voltage slowly increases from around 3 kV until pulse #10 at 5 kV when steady-state was reached. On the other hand, the peak current level increases from 17 A at pulse #1 to 22 A consistently afterwards. The shape of the current pulse further improves towards a box-car shape.

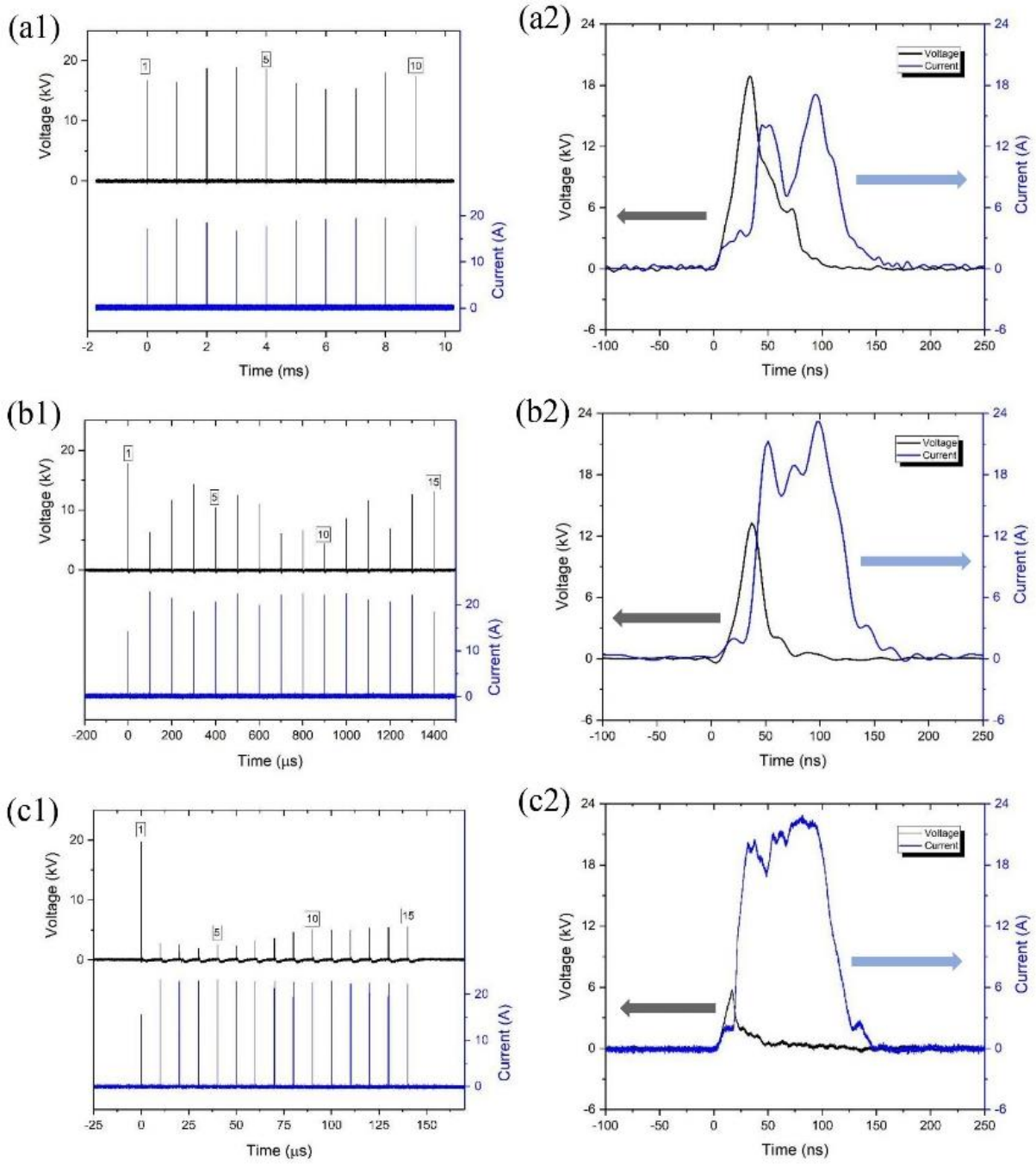

Figure 3-18. Voltage/current waveform. (a1) V-I waveform of a 10-pulse burst at 1 kHz. (a2) V-I waveform of a single pulse at quasi-steady-state at 1 kHz. (b1) V-I waveform of a 15-pulse burst at 10 kHz. (b2) V-I waveform of a single pulse at quasi-steady-state at 10 kHz. (c1) V-I waveform of a 15-pulse burst at 100 kHz. (c2) V-I waveform of a single pulse at steady-state at 100 kHz.

By integrating the product of voltage and current on each single discharge, the pulse energy input with respect to the number of pulses at different frequencies is calculated and the results are shown in Figure 3-19. It has been shown that no memory effect exists at frequency of 1 kHz based on voltage/current profiles, which is further supported by the energy deposition calculation as shown in Figure 3-19 in which, for simplicity, discharge energies for only pulse number 1, 5, 10, 15 were calculated and plotted. In the case of 10 kHz, except for pulse #1, the energy input per pulse oscillates between 2.5 and 3.9 mJ with roughly the same pattern as the breakdown voltage as shown in Figure 3-18b-1. One can see that neither voltage/current nor energy input show that NRP discharges at 10 kHz reaches an ideal steady-state operation. This is due to the unstable energy input from the pulser in response to different impedance between electrodes. Specifically, according to the voltage/current waveform and the corresponding energy input, one can see that a higher breakdown voltage is associated with a higher discharge energy input, which further causes a more intense heating and a higher initial temperature for the subsequent discharge. Assuming ideal gas law and constant pressure, a higher local gas temperature thus translates to a lower gas density which in turn reduces the required voltage for equivalent reduced field for the breakdown. As a result, the breakdown voltage is lowered as well as the energy input of the corresponding discharge. The next discharge will in turn have a higher breakdown voltage and energy input in comparison. As one can predict, discharge parameters will never converge. With additional disturbance during cooling (turbulence), the outcome is thus an unsteady sequence of discharges with energy input randomly at 3.2±0.6 mJ. At $f = 100\ kHz$, one can see that energy per pulse shares very similar pattern with the breakdown voltage vs number of pulses as shown in Figure 3-18c-1. Energy per pulse drops to around 1.1 mJ after the initial pulse and recovers to around 1.4 mJ at pulse number 10 where steady-state was reached.

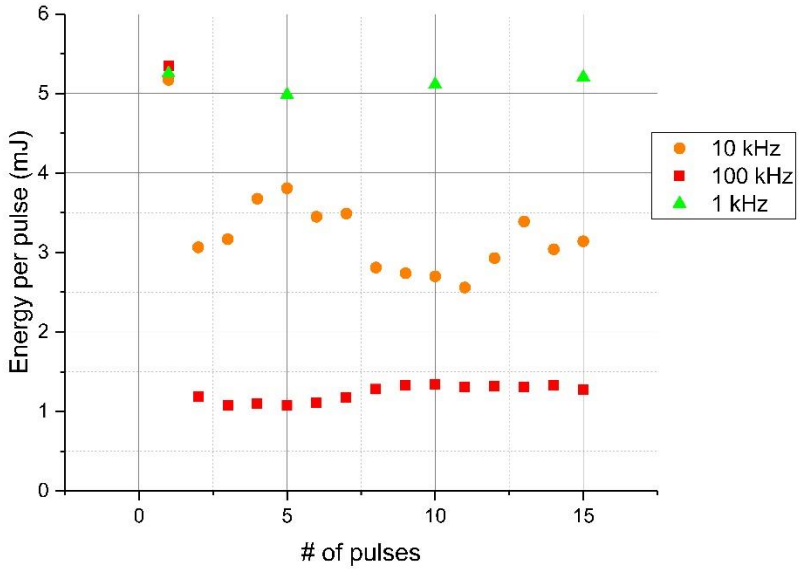

Figure 3-19. Energy deposition per pulse vs. number of pulses for different repetition frequencies

Temperature T_{gas} was also measured at different instances during a discharge at different number of pulses. As described in the previous section, the lower T_{gas} measured at certain pulse represents the initial temperature before the initiation of the pulse ($T_{gas\_initial}$), and the higher value represents the highest temperature measurable during the window of visible SPS spectra (T_{gas_high}). The results are presented in Figure 3-20. For $f = 1\ kHz$, it can be seen that $T_{gas\_initial}$ for all the pulses throughout the burst is around 300 K and heats up by approximately 200 K which resembles the experimental measurements for the single-pulse condition. As for $f = 10\ kHz$, $T_{gas\_initial}$ decreases from 1600 K at pulse #2 to 1100 K at pulse #10 and stays constant for the remainder of the burst. The amount of temperature rise measured within the pulse is approximately 800 K. Note, the unrepeatability observed in voltage/current/energy before is less pronounced in T_{gas} measurement. This is due to the fact that ~100 accumulations were taken when recording the SPS spectra, thus the fluctuation is flattened and averaged. Furthermore, the decrease of $T_{gas\_initial}$ from pulse #2 till steady state can be explained by the lower energy input per pulse after pulse #1 on average, which translates to a lower temperature reached when equilibrium with the reservoir was built. On the contrary, for the case of $f = 100\ kHz$, one can see that T_{gas_inital} increases over the number of pulses, from 4000 K at pulse #2 to 5000 K at steady-state after pulse #5. The short time interval between pulses (10 μs) is in favor of keeping the heat between electrodes until the next pulse energy input thus a higher temperature can be maintained at equilibrium. It is important to

note that, no conclusion could be drawn from the relation between the difference of T_{gas_high} and T_{gas_inital} with the energy input per pulse. This is due to the fact that T_{gas_high} does not represent the absolute highest temperature ever achieved after the discharge.

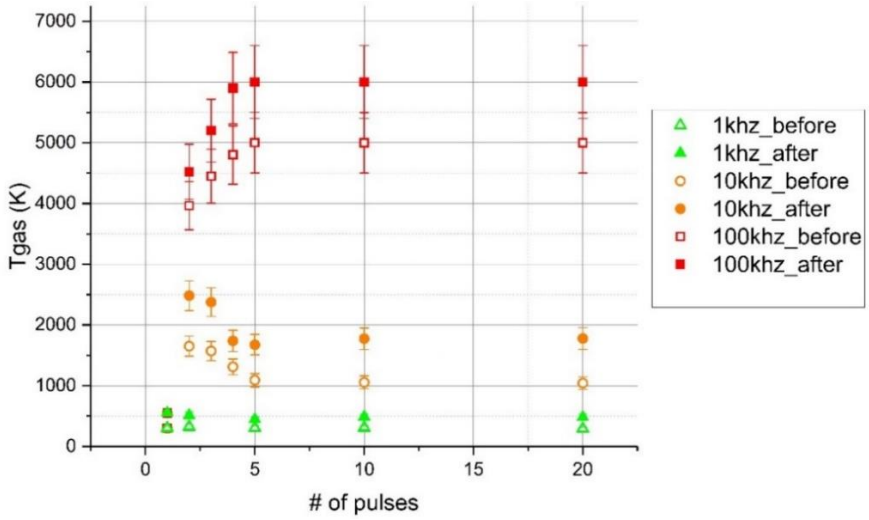

Figure 3-20. Gas temperature vs. number of pulses for different repetition frequencies

Similar study on the gas density n_g by LRS was also conducted and the results of relative density n_g/n_{g0} (n_{g0} is the ambient gas density) at certain pulse for three repetition frequencies are presented in Figure 3-21. Similarly, two measurements of n_g were taken at each pulse: initial n_g of each pulse (n_{g_inital}), and the lowest n_g after discharge which was measured 5 μs after the discharge (n_{g_low}). For $f = 1\ kHz$, only the initial values of n_g at pulse #5, 10, and 20 were recorded to further verify the non-existence of memory effect at $f = 1\ kHz$ as presented in Figure *3-21* as hollow green triangles. As for $f = 10\ kHz$, one can see that n_{g_inital} is fluctuating at around 40% of the ambient level and the amount of density decrease due to the energy input per pulse ranges from 7% to 20% of the ambient value. It takes roughly 10 pulses for n_g to settle to a relative steady-state operation. The unsteadiness of the pulse energy input as shown in Figure 3-18 and Figure 3-19 is more pronounced in the measurement of n_g in comparison with that of T_{gas}, which is caused by the fewer numbers of accumulations taken for LRS measurements (10). In addition, one can also see that a higher $n_{g\_initial}$ is associated with a larger density drop afterwards, resulting in n_{g_low} to be around 32% of ambient level for all pulses measured after pulse #4. Such observation agrees with our previous verdict that a higher initial density (and lower temperature) leads to a higher pulse

energy input which ultimately results in a larger density drop after the corresponding discharge. For the case of $f = 100\ kHz$, n_{g_inital} drops from 30% of ambient on pulse #2 to approximately 8% of ambient on pulse #10. It follows a similar pattern as T_{gas} but in different direction to conserve ideal gas law. It can also be concluded that, the amount of density drop per pulse decreases with the increase of *f*: from 70% of n_{g0} at 1 kHz (equivalent to single pulsed condition [103]), to 1% of n_{g0} at 100 kHz, which can be explained by a less energy input per pulse at higher *f*.

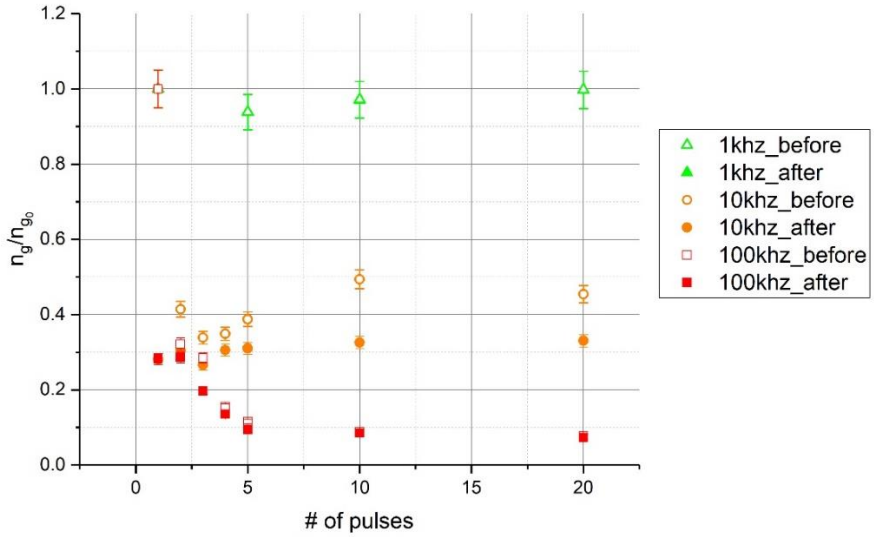

Figure 3-21. Relative gas density vs number of pulses for different repetition frequencies

Temporal evolution of n_e was also investigated. Let us first re-consider the expression for the microwave scattering system. As shown in [113], total power radiated by the plasma dipole Θ, which is proportional to the total scattered signal voltage U_{out} to the power of 2, which can be expressed as:

$$U_{out}^2 \propto \Theta \propto \frac{V^2 \omega_p^4 \omega^4}{\left(\omega_p^2 - \omega^2\right)^2 + (\upsilon_m \omega)^2} \qquad (1)$$

where *V* is the volume of the plasma, ω_p is the plasma frequency which is proportional to n_e to the power of 1/2: $\omega_p \propto \sqrt{n_e}$, ω is the external microwave frequency, ν_m is the momentum-transfer collisional frequency of electron. By assuming: $\nu_m \gg \omega, \omega_p$, one can simplify the equation above and get a relation as [22]:

$$U_{out} = \frac{Ae^2 V n_e}{m\upsilon_m} \propto \frac{V n_e}{\upsilon_m} \propto \sqrt{\frac{V^2 n_e^2 \omega^4}{\left(\omega_p^2 - \omega^2\right)^2 + (\upsilon_m \omega)^2}} \qquad (2)$$

Where A is the proportionality factor representing the sensitivity of the microwave system. e and m are the electron charge and mass, respectively. This is the 'microwave Rayleigh scattering' regime that most weakly-ionized atmospheric plasmas are in [36] [97] [22] [74] [76]. Specifically, ν_m is estimated to be on the order of 10^{12} s^{-1} while microwave frequency is on the order of 10^{10} s^{-1} (~10 GHz) which is much smaller in comparison [18]. However, it has been shown in Figure 3-21 that, by sending ns-pulses in burst with high repetition frequency, local n_g can drop by more than 10 times (at f=100 kHz), resulting in ν_m dropping to a level that is comparable with ω ($\upsilon_m \propto n_g$ [103]). As a result, the microwave scattering off the plasma is no longer in the 'Rayleigh' regime but a transition regime between Rayleigh and Thomson, and the expression between U_{out} and n_e thus needs to be re-written as:

$$U_{out} \propto \frac{V n_e}{\sqrt{\omega^2 + \upsilon_m^2}} = \frac{Ae^2 V n_e}{m\sqrt{\omega^2 + \upsilon_m^2}} \qquad (3)$$

Where ν_m is acquired from the n_g measurements same as in work [103]. Note, the temporal evolution of both T_{gas} and n_g over the burst is simplified as a smoothed line connecting the initial values of every measured pulse. As a result, information of detailed decay waveform of n_e on each discharge was not discussed in this work in detail especially for $f = 10\ kHz$.

With the measurement of n_g as well as raw MRS signal, by implementing the method described in [103] with the updated equation (3), one can now calculate the electron number density n_e and the results are plotted in Figure 3-22. Due to the fact that discharges at 1 kHz have been proven to be free from memory effect, only the temporal evolution of n_e for $f = 10\ \&\ 100\ kHz$ are presented. It can be seen from Figure *3-22*(a) that, for $f = 10\ kHz$, the maximum number of n_e produced reduces from around 5×10^{15} on pulse #1 to $1.5\pm0.2\times10^{15}$ cm^{-3} on pulse #5 and later, with the corresponding total electron number N_e of 1.2×10^{12} and 3.7×10^{11}, respectively. It is important to note that, the electron number density n_e presented in this work is calculated with the assumption of a constant volume of 2.5×10^{-4} cm^3 (a cylinder with height of 5 mm and diameter of 250 μm). And this assumption was held true only during the first few 100s ns of the decay [103]. As a result, only the peak value of N_e&n_e for $f = 10\ kHz$ should be considered accurate in this study.

As for $f = 100\ kHz$, the maximum value of n_e drops to around 1×10^{15} (N_e ~2.5×10^{14}) after pulse #2. In addition, it can be seen from Figure *3-21* that the relative deviation of gas density after each discharge at steady state is much smaller for 100 kHz than 10 kHz (10% vs 50%) after pulse #5. Thus, a constant n_g and volume of plasma was assumed throughout the whole decay process during the steady state operation at $f = 100\ kHz$. It can then be estimated from Figure 3-22(b) that, the decay rate of electrons is slower in the steady-state during the burst (pulse #>6) in comparison with the single-pulse condition: approximately 0.14-0.25×10^7 s^{-1} versus 0.5-0.7×10^7 s^{-1} for the single pulsed condition, with a corresponding characteristic decay time of 400-700 ns and 150-200 ns, respectively. It has been demonstrated in [REF-SP] that, the decay of electrons in the single-pulse ns-discharges is contributed by both dissociative recombination ($X_2^+ + e \rightarrow X + X$, where *X* is *N* or *O*) and three-body attachment to oxygen ($e + O_2 + X_2 \rightarrow O_2^- + X_2$, where *X* is *N* or *O*) with a comparable decay rate in the range of 10^6-10^7 s^{-1}. [108] For NRP discharges at $f = 100\ kHz$, where local gas density dropped by more than 10 times, the decay rate contributed by three-body attachment is expected to drop by more than 100 times to the order of 10^5 s^{-1} [92], making dissociative recombination the dominating decay mechanism. The decay of electrons governed by recombination is thus expressed as: $\frac{dn_e}{dt} = -\beta n_e^2$, where the decay rate can be correlated with electron number density and electron temperature as: $\beta n_e \propto \frac{n_e}{T_e}$, where β is the recombination constant and T_e is the electron temperature [108]. As shown in [33], electron temperature measurement during later pulses is approximately 50% of the value for the initial discharge for repetition frequency of 50-100 kHz. In combine with the 5-time drop of maximum electron number density presented in Figure 3-22(b), the decay rate of the electrons in the steady state at $f = 100\ kHz$ is thus expected to be lower than that for single pulsed condition by about 2.5 times, which is in a good agreement with our experimental measurement.

Furthermore, one can see that a higher *f* leads to a smaller n_e. When combining with the data for n_g, one can also conclude that a higher *f* results in a plasma production with higher ionization degree: from 0.02% for $f = 1\ kHz$ (or single-pulse), to 0.024% for $f = 10\ kHz$, to 0.04% for $f = 100\ kHz$. A higher ionization degree may be caused by a higher density of metastables and higher initial temperatures due to the more intense memory effect at higher *f* with less cooling time between pulses, as well as a more intense over-voltage effect: The reduced field

at breakdown for 100 kHz (500 Td) was approximated to be 3.1 times higher than that for 10 kHz (~160 Td), and 3.5 times higher than the 1 kHz case (144 Td).

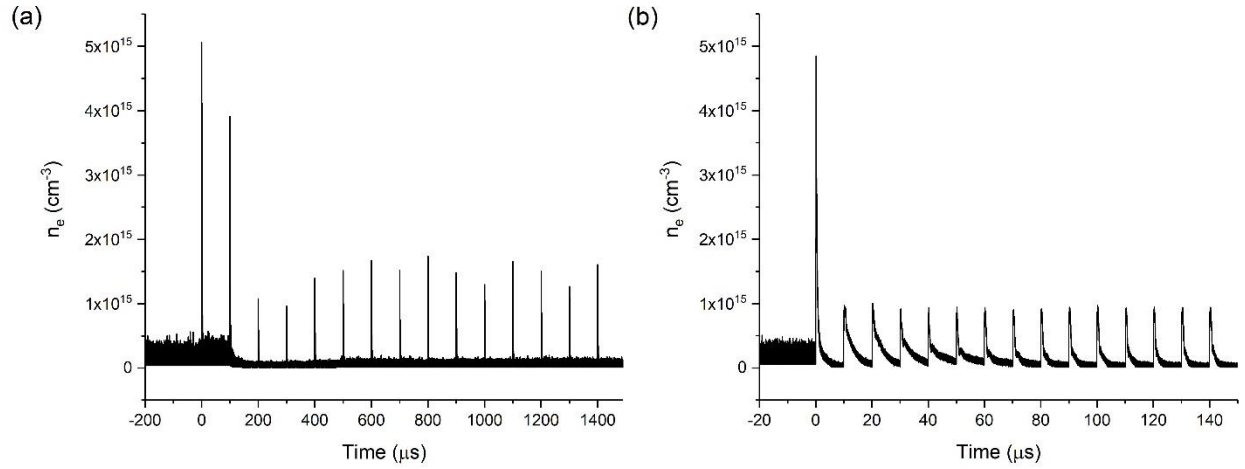

Figure 3-22. Temporal evolution of n_e at (a) 10 kHz; (b) 100 kHz

3.2.5 Conclusion

To conclude, the study of the effect of repetition frequency on the pin-to-pin NRP discharge at atmospheric condition was conducted, in which the transient process of the discharge conditions from single-pulse to steady-state burst operation was emphatically investigated. It has been shown that it takes approximately 10 pulses to reach steady state operation. In addition, it is also demonstrated that higher repetition frequency leads to lower energy input per pulse, higher local temperature, lower gas density, and lower electron number density but higher absolute ionization degree. The necessity of re-adjusting the formula of microwave scattering system due to the comparable collisional frequency and microwave frequency is also expressed. Future work includes the study of NRP discharge over a wider pick of repetition frequencies, as well as to study the decay of plasma over specific discharges to acquire a more quantitative analysis of the decay mechanism.

4 STUDY OF THE DC-DRIVEN HELIUM PLASMA JET

4.1 DC-driven plasma gun: self-oscillatory operation mode of atmospheric-pressure helium plasma jet comprised of repetitive streamer breakdowns

Xingxing Wang, Alexey Shashurin
Purdue University, School of Aeronautics and Astronautics, West Lafayette, IN 47907, USA

Portions of this chapter have been previously published in Plasma Sources Sci. Technol.
DOI: 10.1088/1361-6595/aa52fc

4.1.1 Abstract

This paper presents and studies helium atmospheric pressure plasma jet comprised of series of repetitive streamer breakdowns, which is driven by a pure DC high voltage (self-oscillatory behavior). Repetition frequency of the breakdowns is governed by the geometry of discharge electrodes/surroundings and gas flow rate. Each next streamer is initiated when the electric field on the anode tip recovers after the previous breakdown and reaches the breakdown threshold value of about 2.5 kV/cm. Repetition frequency of the streamer breakdowns excited using this principle can be simply tuned by reconfiguring the discharge electrode geometry. This custom-designed type of the helium plasma jet, which operates on the DC high voltage and is comprised of the series of the repetitive streamer breakdowns at frequency about 13 kHz, is demonstrated.

4.1.2 Introduction

Atmospheric pressure plasma jets (APPJ) are widely used nowadays in the fields of bio-engineering, medicine, food processing etc. [114], [115], [116], [117], [118] Direct sterilization by APPJ of open wounds, ulcers or burns is more efficient compared to ordinary sterilization using chemicals due to the potential extend damage that chemicals may cause to punctured tissues and organs. [119] APPJ can also be used for treatment of various types of cancer including lung, bladder, skin, head and neck, brain, pancreatic tumors etc. [115], [116], [119], [120], [121]

Conventional APPJ are excited in helium (He) flow exhausted from the discharge tube into open air. Multiple parameters of He plasma jets were measured previously including plasma density, temperatures of various species, electrical currents etc. [122] Typically, plasma electron

density n_e is in the range of 10^{12}-10^{13} cm^{-3} while the temperature of heavy species is near the room temperature at 300-350 K. [123]

Conventional APPJ are excited using AC or pulsed DC power supplies operating in kV range and frequencies around 10s of kHz. [123], [124], [125], [126], [127], [128], [129] In those cases, breakdown takes place once every cycle of the applied high voltage (HV) when the voltage applied to the electrode reaches the breakdown threshold. The breakdown is associated with development of streamer tip propagating at characteristic velocities in the range of 10^6 -10^8 cm/s increasing with the high voltage magnitude. [123] The duration of each individual streamer does not exceed the period of time of several μs and stops where the presence of the oxygen in the He jet increases along the jet to about 1 percent. [123], [130], [131] The plasma remaining in the streamer channel decays shortly afterwards (on time scale of about several μs). The next breakdown event occurs on the next cycle of the applied AC high voltage or with the application of the next high voltage pulse. Thus, the repetition frequency of the discharge is fully governed by the discharge driving power supply operation frequency. [129]

Therefore, excitation of the helium APPJ by AC and pulsed DC high voltage was studied previously. However, it is interesting to evaluate excitation of the helium APPJ by means of constant DC high voltage applied to the electrode. Obviously, simultaneously with the initial application of the DC high voltage the first streamer will be initiated similarly to that in DC pulsed excitation. Shortly after the firing, the streamer stops and plasma column decays (about few μs after the firing). [123] [132] [133] [134]. Once plasma decay is complete, the system returns back to the conditions which, from the first glance, are indistinguishable from those existing prior to the shooting of the initial streamer. Then, obvious questions arise: Will the second streamer be fired in the system and what governs the timing of its firing? How can the repetition frequency of these streamers be controlled?

This paper studies the He plasma jet comprised of a series of repetitive streamer breakdowns which is excited by pure DC high voltage and demonstrates the ways to control the frequency of streamer repetition. Cold plasma gun operating on this principle is presented.

4.1.3 Experimental setup

The schematics of the circuitry are shown as Figure 4-1. A DC power supply up to 5 kV was used in the experiments. A mass flow controller (Sierra SmartTrak 100) was used to control

the He supply into the nozzle. The high-voltage electrode on the axis of the nozzle was immersed into the He which flowed through the nozzle into open air. The inner diameter of the nozzle exit was 3.6 mm. A grounded metal sheet was installed outside the nozzle at the distance *d*. The electrical current was measured using a 10 kΩ shunt resistor placed in series in the HV line as shown in Figure 4-1.

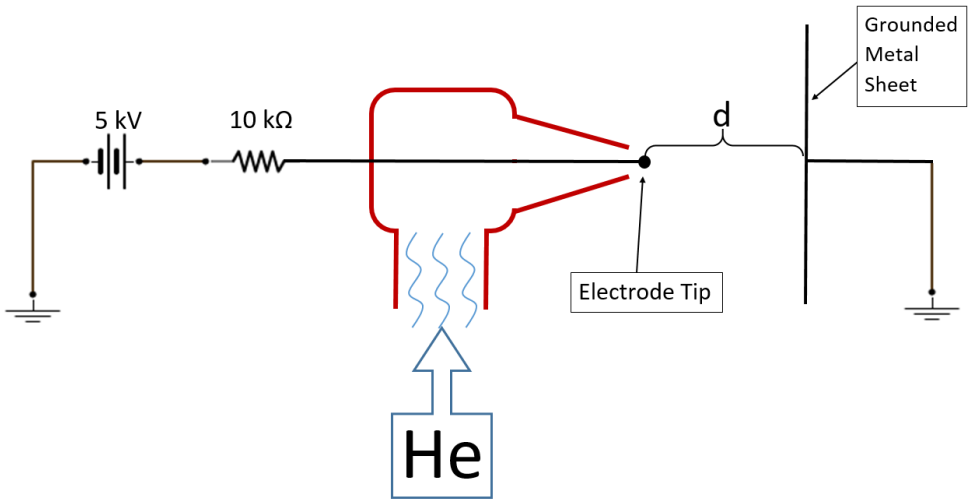

Figure 4-1 Schematics of the experiment setup

4.1.4 Results and Discussion

Series of the streamer breakdowns were observed when 5 kV DC voltage was applied to the electrode as shown in Figure 4-2 (a). The time interval between two adjacent streamer breakdown pulses was 400-750 μs and amplitude of the current pulse was about 0.15-0.25 mA. A close look of the current and voltage waveforms of an individual discharge is shown in Figure 4-2 (b). It is important to note that the applied HV remains constant throughout the entire duration of the experiment including the period of streamer breakdown. In this setup the ground metal sheet was placed far away from the nozzle in order to eliminate its effect on the discharge behavior, whereas the surroundings were considered to provide the ground potential for discharge. Current pulse width was about 1.5 μs. The streamer development was photographed using an intensified charge-coupled device (ICCD) camera as shown in Figure 4-2 (c) for the moments of time *[t1]-[t6]* indicated by the rectangular bars shown in Figure 4-2 (b). Average velocity of streamer front propagation was ~$2.5 \cdot 10^6$ cm/s. Note, repetitive streamer breakdowns presented in Figure 4-2 are

different from self-pulsing atmospheric-pressure plasma jets studied recently [135] [136] [137] [138]. Even though DC high voltage sources were utilized in these works, measurement of voltage and current waveforms revealed dramatic reduction of the electrode voltage every time breakdown occurred, similar to fairly well-studied pulsed DC atmospheric-pressure plasma jets. [123]

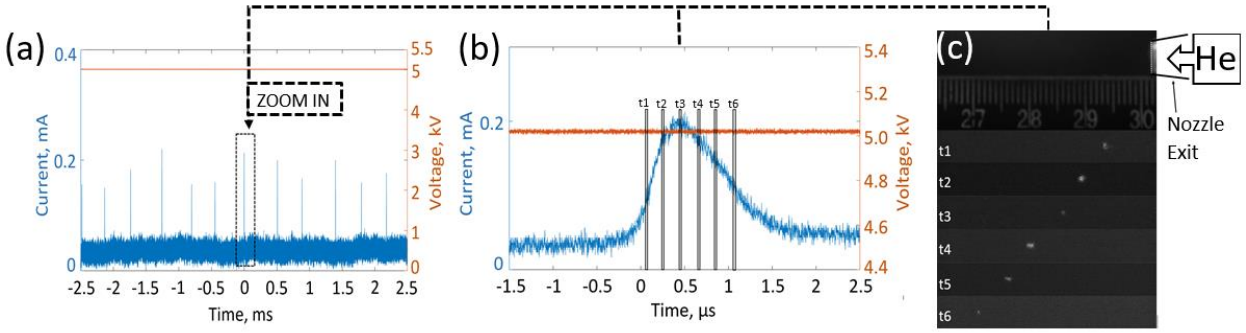

Figure 4-2 (a) Current and voltage waveforms of series of the streamer breakdowns excited by the 5 kV DC voltage supplied to the electrode. (b) Current and voltage waveforms of an individual streamer breakdown. [t1]-[t6] are the time periods when a photograph of the streamer was taken. (c) Photographs of the streamer at certain time from [t1] to [t6]. The grounded electrode was located at $d \approx 0.5$ m. The He flow rate was 1 L/min.

The phenomenon of repetitive streamer pulsations is well-known for streamer corona in air and called flashing streamer corona. [58] Flashing streamer corona happens when low-current streamers periodically generated at HV electrode and decay after a short distance. The frequency of repetitive pulsations of the DC driven streamer corona in air is typically within around 5-10 kHz. [58], [139] For example, the repetitive streamer breakdowns were observed at the frequency < 6.5 kHz when 5 – 9.3 kV DC voltage was applied to a needle electrode of radius 0.17 mm placed 31 mm away from the cathode plate. [58] Control of streamer repetition rate using injection of various types and concentrations of gases into corona region was also studied previously. [140] The repetition frequency is governed by the following process. During each streamer breakdown, electrons which are produced by ionization of air on the streamer path are flowing into the anode electrode. This process can be easily understood by imagining "metallization" of the regions occupied by the streamer channel. The term "metallization" is used here to indicate presence of finite electrical conductivity of plasma along the streamer channel as oppose to the non-conducting air. For example, for ideally conducting streamer channel positive potential of the anode will be establishing along the entire streamer path (of course, in reality the potential along the streamer

channel drops below the anode potential due to finite conductivity of plasma in the streamer channel). Establishing of this positive potential along the streamer path causes removal the excess of the electron charge from the streamer channel to the anode electrode and build-up of the positive space charge along the streamer path. Later, when the streamer growth stops and the plasma in the streamer channel decays, the remaining positive space charge compensates the electric field near the anode, which prevents initiation of the new streamer. However, as far as the positive space charge drifts toward the cathode, the electric field near the anode is restored. New streamer is initiated when the near-anode electric field is reaching the threshold value required for the breakdown.

Therefore, it might be concluded that initiation of each next streamer breakdown occurs when the electric field at the anode recovers after the previous breakdown and exceeds the threshold value E_{th}. Moreover, the value of E_{th} is universal for the fixed gas composition and the pressure. Indeed, geometry of electrodes or other parameters of the system can cause redistribution of the electric field, but cannot affect the E_{th} value. The streamer will fire at the location where E_{th} is reached first. The value of E_{th} was determined experimentally as follows.

Voltage was applied to the spherical electrode immersed in the He flow using the setup shown in Figure 4-1. The voltage was increased from zero up to the value U_{th}, when firing of the first streamer was detected (no space charge remaining from the previous breakdowns). In this case, the electric field (E) in vicinity of the spherical high voltage electrode is related to the tip voltage (U) as $E = \frac{U}{a}$, where a is the radius of the electrode tip sphere. Thus, the threshold electric field (E_{th}) was determined as:

$$E_{th} = \frac{U_{th}}{a}. \qquad (1)$$

Note, the threshold electric field E_{th} is defined as the electric field on the electrode prior to the streamer initiation and thus, governed by the electrode radius a as shown in Eq. (1), [58] while local electric field around the streamer tip during the following streamer growth is governed by the radius of the streamer channel (r_s) and can be written as $\frac{U}{2r_s}$ for ideally conductive streamer channel. [141]

In order to evaluate critical electric field E_{th} required to fire the streamer, we used three spherical HV electrodes of diameters 1.59 mm, 2.38 mm and 3.18mm. The dependence of U_{th} required to fire the first streamer on electrode tip diameter is shown in Figure 4-3. One can see that

the dependence was linear and crosses the origin. This clearly indicates that threshold electric field strength was constant, E_{th} = 2.5 kV/cm, for all cases, which supports the predictions formulated above. Note, wire supporting the spherical electrode in this experiment was electrically insulated (using ceramics tube) from the He flow to ensure that breakdown starts from the spherical electrode. In the following experiments we have used HV electrode in form of insulated wire with bare end, rather than spherical electrode.

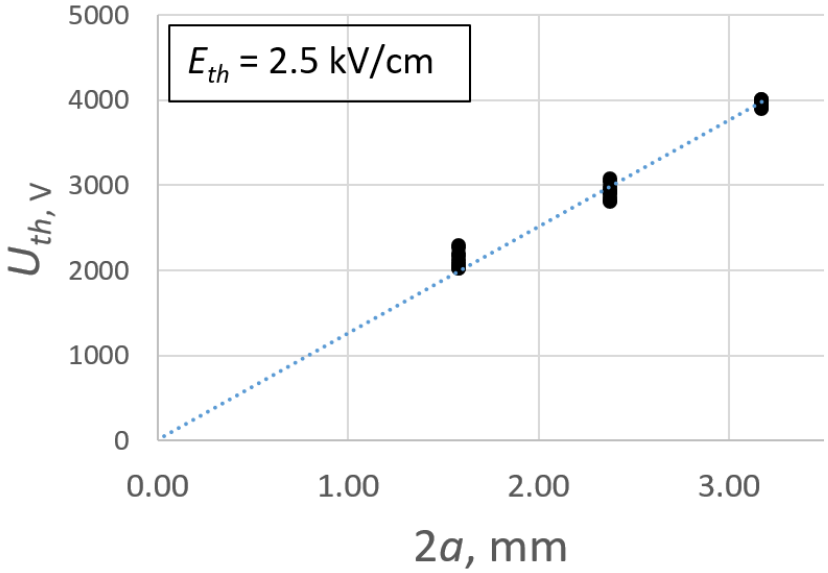

Figure 4-3 Breakdown voltage required for triggering the first streamer for three different sizes of spherical electrodes. Threshold electric field required for the breakdown is about 2.5 kV/cm regardless the electrode size.

Let us now consider the ways how frequency of repetition of streamer breakdowns can be controlled. Figure 4-4 shows the time interval between two adjacent streamer breakdowns (T_{rep}) vs. He flow rate. One can see that the time interval between breakdowns was reduced with the increase of He flow rate. This can be explained by the fact that larger He flow rate leads to faster He flow speed and this in turn results in faster removal of the positive space charge from the vicinity of electrode tip. Thus, electric field in vicinity of the streamer recovered faster to the threshold value E_{th} which led to more frequent pulsations. In addition, it was observed that more frequent streamer pulsations were more repeatable which is seen by decrease of the error bar for higher He flow rates.

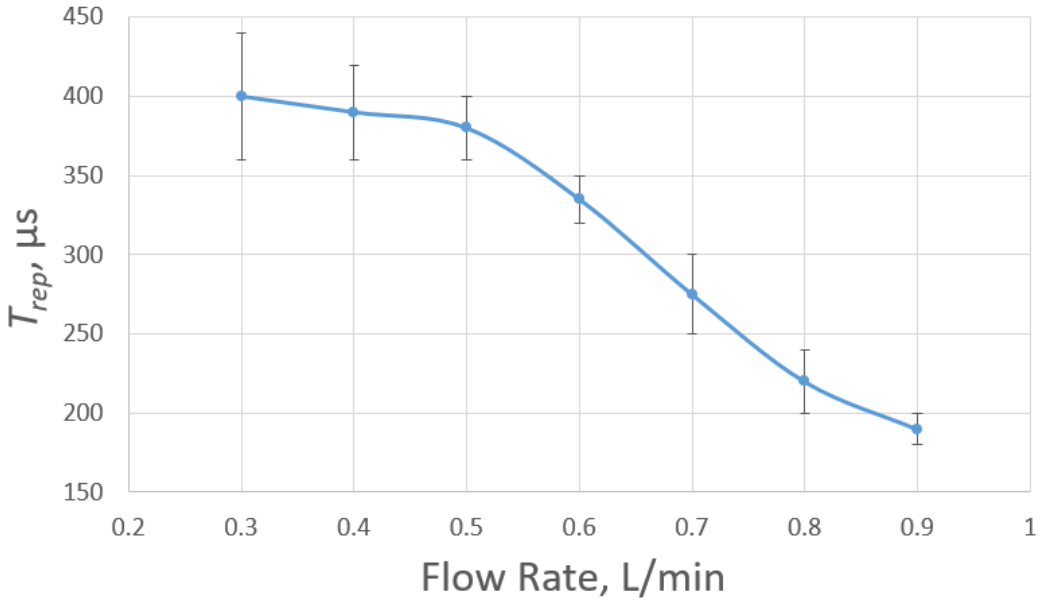

Figure 4-4 Streamer breakdowns vs. He flow rate for d = 5 cm and U = 5000 V.

One important finding of this work is that self-oscillatory behavior of helium APPJ demonstrated here can be controlled by means of reconfiguring the discharge electrode geometry which leads to change of the background potential around the tip electrode. Indeed, electric field near the tip of spherical electrode at potential U immersed in space with background potential U_0 can be written as [141]: $E = \frac{U-U_0}{a}$. The value of background potential can be decreased $U_0 < 0$, for example, by decreasing distance d between the HV electrode tip and grounded metal plate (see Figure 4-1), due to the contribution of 'negative mirror-image charge' behind the plate according to the method of images in electrostatics. [142] The experimental confirmation of this fact is demonstrated in Figure 4-5 showing the relation between the repetition time interval and the distance d. One can see from the plot that the decrease of the distance d caused more frequent streamer firings (period between the streamer firings T_{rep} decreased). More frequent streamer firings were associated with more stable and repeatable operation as indicated by the size of error bars in Figure 4-5.

It has to be noted, the experimental fact that T_{rep} increases for smaller d (Figure 4-4) and for larger flow rate (Figure 4-5) was obtained and confirmed multiple times in single experimental runs consisting in real-time manual adjustment of distance d (or flow rate) in both directions and simultaneous observation of corresponding changes of T_{rep} on oscilloscope. However, spread of

the measured T_{rep} between different experimental runs was quite high (up to 30%) due to high sensitivity of the source to precise geometry of grounded surroundings which is extremely hard to reproduce exactly the same in the different experimental runs. This spread can be traced by comparing of two T_{rep} measurements conducted at close conditions, but obtained in different experimental runs namely, T_{rep}=190 and 250 μs for d=5 cm and very close He flows 0.9 and 1 L/min (see Figure 4-4 and Figure 4-5).

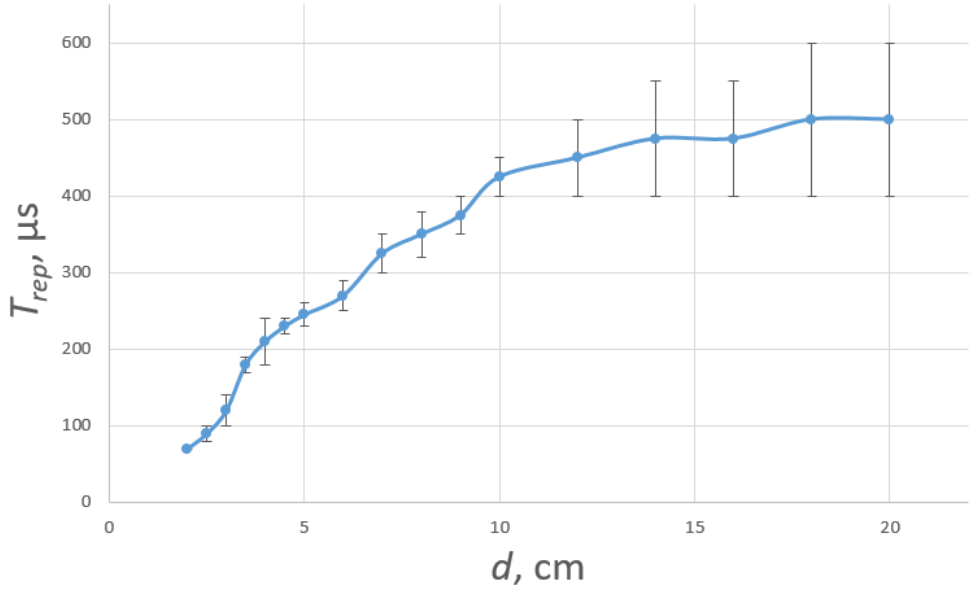

Figure 4-5 Average period between streamer breakdowns vs. distance to the grounding plate d. Flow rate = 1 L/min, U= 5000 VDC.

It is interesting that, the geometrical control of the repetition frequency of the streamer breakdowns can be utilized for creating another type of the helium APPJ as follows. The design shown in Figure 4-6 uses a customized glass pipette and a funnel attached to it. The high voltage electrode (insulated wire with bare end) is inserted into the tube near the nozzle exit while grounded metal ring is fixed on the funnel. The grounded ring was used in order to vary background potential and thus to adjust the repetition frequency of the streamer breakdowns. Helium flow went through the center of the symmetric grounded ring. Several ring sizes and the distances from the pipette exit were tested in order to achieve steady and visible plasma as well as to extend the length of plasma. Within this range, the location of the grounded ring was determined in the design shown in Figure 4-6 in order to fix the repetition frequency at around 15 kHz, which

is typical for conventional APPJ plasma guns. The length of the free plasma jet was approximately 1 cm, while it can be extended to more than 2 cm if a finger is placed in vicinity as shown in in Figure 4-6 (b). The voltage and current during the streamer breakdown are shown in Figure 4-7. One can see that current amplitude was about 0.1 mA and repetition frequency - 13 kHz. APPJ plasma gun presented in Figure 4-6 is a dielectric barrier discharge with central electrode in contact with plasmas and grounded ring electrode is insulated from the direct contact with plasmas. By comparing Figure 2 and Figure 7, one can see that the duration of the discharge increases by approximately factor of 2. This can be explained by the closer proximity of the ground electrode for the case shown in Figure 7 that slows down the streamer front propagation and extend its temporal duration. [143]

In has to be noted that the main difference of the considered here phenomenon of repetitive streamer firing compared to the classical flashing streamer corona in uniform air is that the firing of the streamer occurs strictly along the He jet exhausting from the discharge tube to an ambient air. The streamer propagation is confined to the He jet due to significantly lower avalanche amplification coefficient in the direction perpendicular to the He flow, which is governed by the elevated electron attachment to the ambient oxygen molecules in our case [123] [58] [144] This predetermined streamer path as oppose to the random path of the air steamer and, therefore, enables unique opportunities for geometric control of streamer firing frequency demonstrated in this work.

4.1.5 Conclusion

In conclusion, we have demonstrated mechanism of excitation of helium plasma jet comprised of repetitive streamer breakdowns which is driven by a purely DC high voltage. This type of the plasma source allows control of operation frequency simply by varying the geometry of the discharge electrodes. New type of DC-voltage driven helium plasma jet comprised of pulsed streamer breakdowns is demonstrated. In this paper we have presented a brief experimental demonstration of this phenomenon and some general trends only, while more detailed study is planned for future.

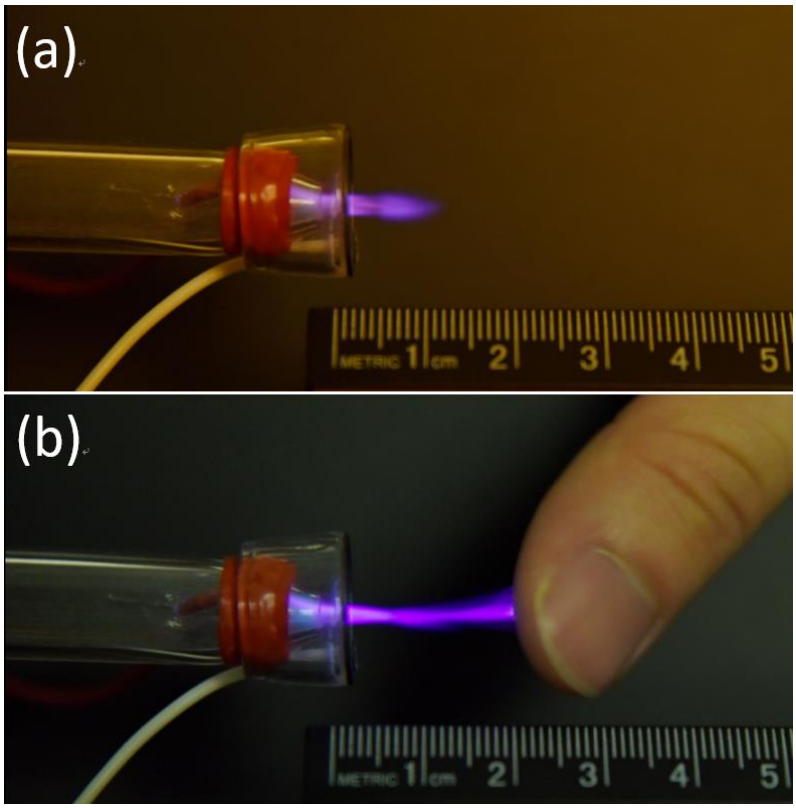

Figure 4-6 Photographs of the APPJ driven by DC high voltage. (a) Length of the free jet is about 1 cm, (b) Length of the plasma jet can be extended to 2 cm if finger is placed nearby. He flow rate is 2 *L*/min and *U* = 3400 V.

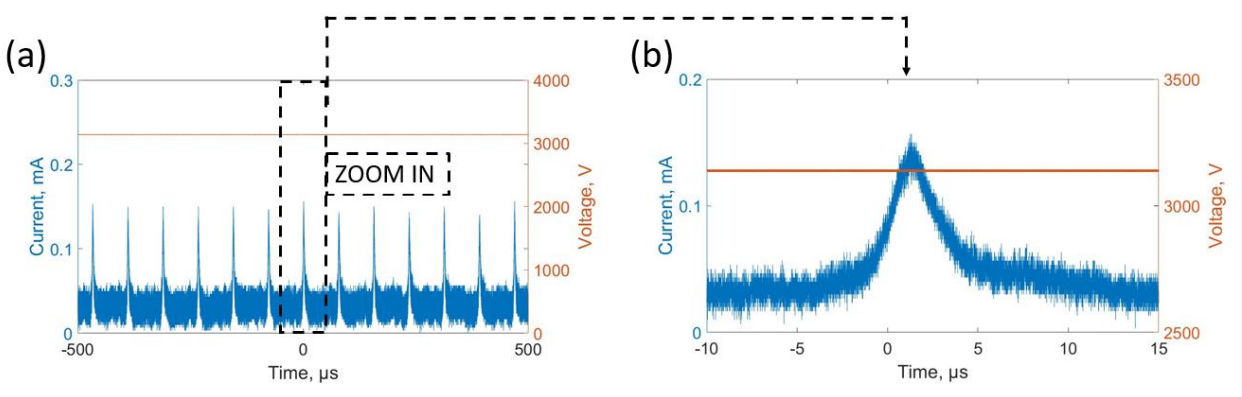

Figure 4-7. Current and voltage waveforms of the APPJ driven by DC high voltage. (a) Multiple breakdown events. (b) Temporally resolved individual breakdown.

4.2 Enhancement of positive pulsed corona by dielectric enclosure

Xingxing Wang, Andrei Khomenko, and Alexey Shashurin
Purdue University, School of Aeronautics and Astronautics, West Lafayette, IN 47907, USA

Portions of this chapter were previously published in AIP Advance
DOI: 10.1063/1.5117830

4.2.1 Abstract

In this work, the effect of positive pulsed corona enhancement by introducing Teflon dielectric enclosure in vicinity to the electrode assembly was studied. The discharge operating in air without the dielectric was able to operate within a very narrow voltage range of approximately 200 V. The pulsing frequency was below 1.2 kHz and current peaks were below 14 mA. Increasing the applied voltage onto the positive electrode beyond this range would result in sparks between the electrodes. When the Teflon tube enclosure surrounding the high voltage electrode was used, the window of stable pulsed corona operation expanded up to 3-5 kV. The pulsing frequency increased up to 12 kHz and the current peak level increased to approximately 35 mA. Increasing voltage beyond the point with peak pulsing frequency would result in a drop of pulsing frequency until the discharge pulsations stopped completely. The Teflon enclosure was able to enhance the average power deposited into the discharge from 10 to 220 mWatt. In addition, the product gases of the enhanced pulsed corona were tested to be mostly ozone with traceable amount of NO_2. The discharge used about 150 eV and 1950 eV per one ozone molecule and nitrogen dioxide molecule respectively.

4.2.2 Introduction

Atmospheric pressure cold plasmas have been found of great value in the field of bio-engineering, medicine, food processing, etc. due to its ability to produce reactive gas species and radicals with minimal energy consumption and gas heating [114] [15] [145] [146] [147]. Conventional atmospheric pressure cold plasmas are generated in noble gas, N2, or air by alternating or pulsed HV powers, with a heating of gas by usually less than 50K while electron temperature can be 1-10 eV [114]. Corona discharge is a very widely used method to produce atmospheric pressure cold plasmas [114]. It's been shown to have a great value in the industry for decontamination, pollution control, etc [148]. It is also applicable in flow control over airfoil for

being able to increase lift, delay separation, etc. [149]. In addition, DC corona discharge devices have been miniaturized for various kinds of applications such as air particle monitoring [150], removing airborne bacteria in respirator [151], bacteria lysis cartridge for water-borne pathogen detection system [152], etc. Negative corona discharge was also utilized for a pressure sensor and a flow velocity meter [153] [154].

One type of corona discharge called 'pulsed corona', which is also known as 'flashing corona' [18] [155] is operating at relatively low voltages where discharge occurs in the intermittent pattern. In a pin-to-plane electrode geometry, with the pin anode separated 31 mm from the plane cathode, positive pulsed corona starts at the voltage of about +5 kV in the form of repetitive current pulses before which, there was no discharge and only a non-self-sustaining direct current on the order of 10^{-14} A (formed by cosmic rays and natural radioactivity) can be observed in the system. [18] [156]. As the applied voltage increases, the frequency of current pulses peaks at the level of 6.5 kHz. As the voltage keeps increasing, the frequency of current pulses drops back to zero, converting into a 'silent' pulseless corona regime. The current level of these pulses is below 1 μA. This kind of discharge behavior is defined as "pre-inception streamers". For pre-inception streamers, as streamer is initiated from the positive electrode, it creates a channel of positive charges that reduce overall field on the anode and prohibit the next streamer from triggering until positive charges are removed from the anode vicinity and the electric field around the anode is restored. This concept was implemented in a DC-driven helium plasma jet device reported recently in works [157] [34].

Utilization of the DC voltage for driving the pulsed corona discharge offers significant benefits for practical applications in comparison to use of radio-frequency (RF). This is due to the relief of the electrical insulation requirements, significant reduction of EM radiation, and easy availability of DC high voltage power supplies rather than RF supplies operating in kV range [157]. However, due to its nature of being an auto-oscillator, control of parameters of pulsed corona such as current level and pulsing frequency can be troublesome since these parameters are naturally chosen by the system itself without any external control. At the same time, ways to control discharge current and repetition frequency are critical since these determine the 'plasma dose' produced by the plasma generator. In previous work with the helium plasma jet device driven by DC HV and operates at auto-oscillatory mode with a constant voltage level, several ways of controlling the current level and repetition frequency of pulsed corona pulses in relatively narrow

range were briefly demonstrated. Specifically, repetition frequency can be increased twice by increasing the helium flow rate from 0.3 to 0.9 LPM, five times by bringing the grounded electrode closer to the anode from 20 cm to 2 cm. In addition, increasing the supplied voltage level from 4.5 to 5 kV resulted in tripling the repetition frequency and doubling the peak current level [157] [34].

Therefore, benefits of DC-driven pulsed corona for cold plasma generation were reported previously. However, ways to control and adjust the discharge parameters in DC-driven pulsed corona were not studied thoroughly. In this work, we demonstrate that parameters of DC-driven positive pulsed corona can be effectively controlled by introducing dielectric surfaces in proximity to electrode assembly when operating at atmospheric conditions.

4.2.3 Experimental setup

A stainless-steel sewing needle with a tip diameter of approximately 200 μm that was fixed onto the end of a high voltage (HV) cable was utilized as the HV central electrode. Positive high voltage up to 20 kV was supplied by a Bertan 225-20 DC HV power supply. A bare copper wire was utilized as the ground electrode. The assemblies were attached to a linear stage separately in order to precisely control the gap distance between the electrodes. When testing the discharge behavior without the dielectric, the grounded wire was directly facing the HV electrode as shown in Fig 4-8(a). When testing with the Teflon enclosure, the enclosure of Teflon between the two electrodes was introduced into the system by inserting the central electrode cable into a Teflon tube with ID of 1/8” and OD of 1/4”. The grounded copper wire was wrapped at the other end of the Teflon tube across its center. A schematic drawing of the plasma device is shown below in Fig 4-8 (a) and (b). The schematics of the circuitry connection are also shown below in Fig 4-9. We used a high-power 1 MΩ current-limiting resistor in series with the HV power supply. A Tektronix P6015A HV probe up to 30 kV (Voltage probe 1) was connected to the high voltage electrode to monitor the voltage applied to the discharge (for accurate current measurement, presented below, this probe was unplugged). A non-inductive precision 1% 950 Ω resistor was connected in series on the HV line to measure the current on the high voltage side of the discharge. A special Lecroy high voltage fiber optically isolated probe (HVFO) was used to measure the voltage drop on the resistor, both DC and AC components. On the high voltage side, the current flowing through the circuitry I is express as: $I = \Delta V/R$, where ΔV is the voltage potential difference on the 950 Ω resistor. In companion to that a Lecroy PP022 probe (Voltage probe 2) was connected to the grounded

copper wire, which was coupled to ground by another precision 1% 950 Ω resistor. Additionally, we investigated an AC component of the HV side current by a Bergoz fast current transformer (not shown in Figure 2). Thus, we had evaluated three different readings – two for the HV side and one for Ground side – and found them in good agreement between each other for all working regimes. Further, only Ground side current shunt was used for current measurement. The oscilloscope used in this experiment was Lecroy HDO 800 with bandwidth of 3 GHz.

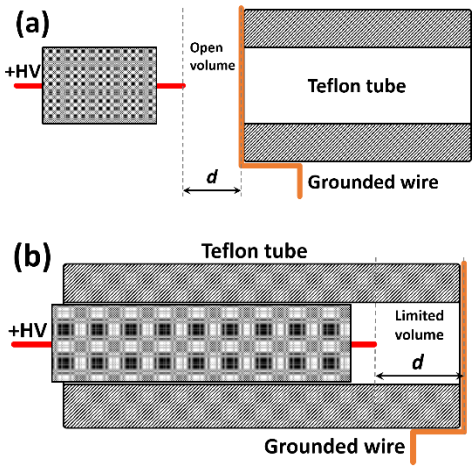

Fig 4-8. Experimental setup for the case without Teflon enclosure (a) and with Teflon enclosure (b).

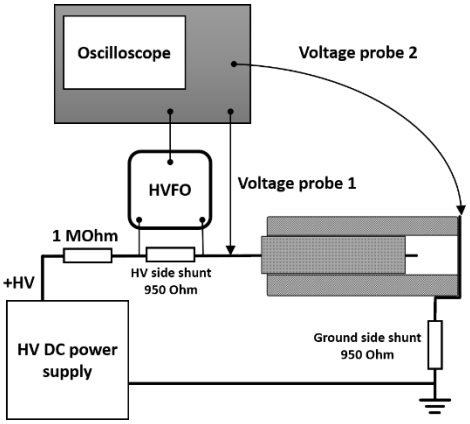

Fig 4-9. Electric circuitry used in the experiment.

In order to measure the reactive gases produced by the pulsed corona, the Teflon tube was placed in an acrylic enclosure where a constant air stream blows on the discharge, as shown in Fig 4-10. The downstream flow was directed to gas analyzers. For nitric oxide and nitrogen dioxide we utilized a Thermo 42C high level NO-NO_2-NO_x analyzer with a measuring principle based on chemiluminescence, and for ozone a custom-built device based on UV absorption at 254 nm was used.

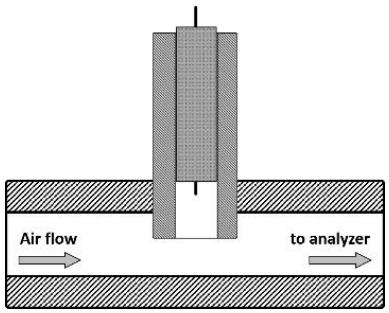

Fig 4-10. Schematics of the system utilized for testing reactive gases produced by the plasma source.

4.2.4 Experimental results and discussion

At a fixed gap distance between electrodes *d*, when increasing the voltage *V*, the current pulses would start to initiate in the form of irregular pulsations. As *V* increases, the current pulse became more stable and repeatable. An example of the continuous current pulses is shown below in Fig 4(a). A close look of a single current pulse is also shown in Fig 4-11(b). One can see from Fig 4-11(b) that individual discharge event consists of two stages: at the beginning stage, the current peak of about 14 mA and duration of about 100 ns was generated; while at the later stage, current pulse of about 100 μA and duration tens of μs was observed. The shape and duration of each individual pulse in all conditions tested in this work were very repeatable with variations <10%. It is important to note that, the discharges studied in this work is only positive pulsed corona discharges. Trichel pulses that associated with negative polarity voltage is not considered in this work [158].

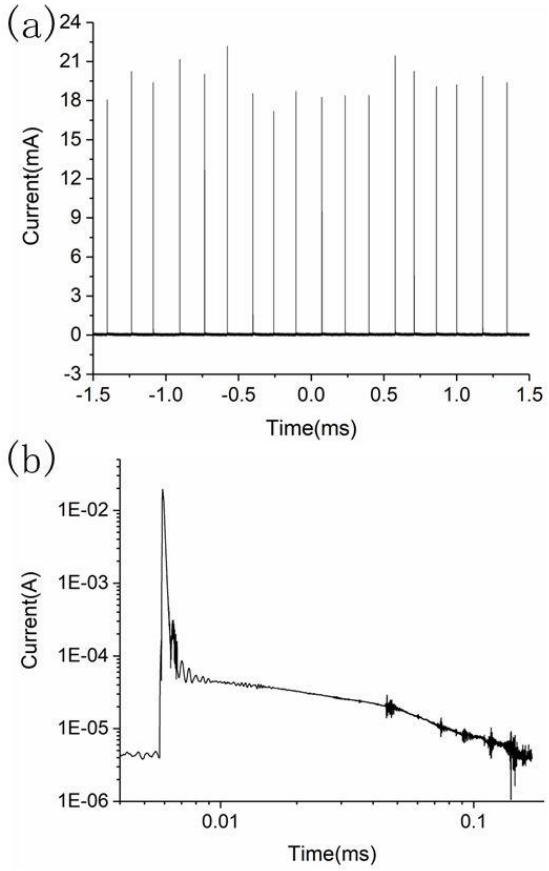

Fig 4-11. Temporal evolution of current of DC-driven pulsed corona without dielectric. (a) Series of current pulses, (b) Typical appearance of the individual current pulse.

The gap distance *d* was adjusted between 4 and 12 mm with the increment of 1 mm. For the case of electrode assembly without the Teflon enclosure shown in the Fig 4-12(a), the dependencies of pulsed corona pulsing frequency and peak current value vs. V at different gap distances are shown below as Fig 4-12(a) and Fig 4-12(b). It was observed that starting from the moment when continuous pulses started to operate, as *V* increases, both pulsing frequency and peak current increases rapidly and quickly reaches the level that leads to sparks. It can be seen that the voltage range of continuous pulsing operation was very narrow, approximately 200 V at each gap distance. Within that range, when d =4 mm, frequency increased from f_{min} =0.01 kHz to f_{max} =1.2 kHz when voltage increased from 4.7 to 4.9 kV. As the gap distance increases, the frequency range shrinks by both having a greater minimum value f_{min} and a smaller maximum value f_{max}. At d = 12 mm, the frequency increased from 0.5 kHz to 0.58 kHz when voltage increased from 16.6 to 16.9 kV. On the other hand, when d increases, the minimum value of current pulses I_{peak}

increases from 7.5 to 13 mA. However, the maximum value of I_{peak} saturates at the level of approximately 14 mA starting from d = 5 mm.

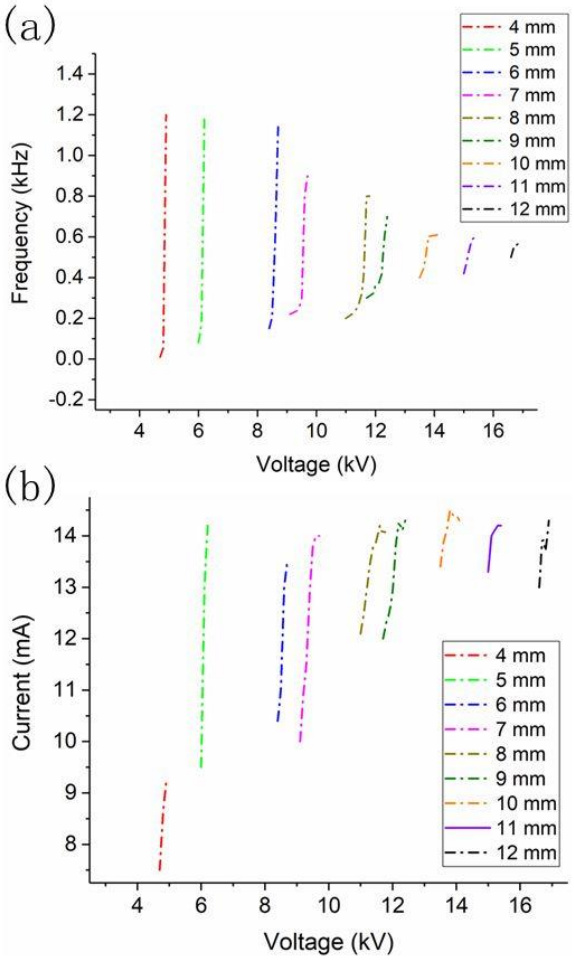

Fig 4-12. Frequency of current pulses vs. DC voltage at different gap distances without Teflon (a). Peak value of current pulses vs DC voltage at different gap distances without Teflon (b).

For the case when the Teflon enclosure was introduced into the system as shown in the Fig 4-8(b), the frequency and current peak value of stable pulsed corona pulses were measured as shown below in Fig 4-13(a) and (b). A bell-shaped distribution of pulsing frequency vs. driving DC voltage was observed for all gap distances as shown in Fig 4-13 6(a), indicating that as voltage increases, the device was able to reach the 'silent' pulseless region after reaching the maximum pulsing frequency. For d = 5mm, the pulsing frequency increases from zero up to 12 kHz at V = 6.5 kV, then drops back to zero at V = 7.8 kV. One can also see that, as d increases, f_{max} drops from

12 kHz at d = 5mm, down to 2.2 kHz at d = 11mm. In addition, as d increases, the range of operating voltage expands from 3 to 5 kV. On the other hand, the peak value of current pulses shows a similar trend as without the Teflon enclosure, as shown in Fig 4-11(b) and Fig 4-13(b). For each d, as voltage increases, I_{peak} increases. The minimum value of I_{peak} also increases with d, from 12 mA at d = 5 mm up to 30 mA at d >10 mm. Saturation of I_{peak} was also observed. The saturation level of value of current peaks was about 35 mA and could be achieved when $d \geq 5$ mm.

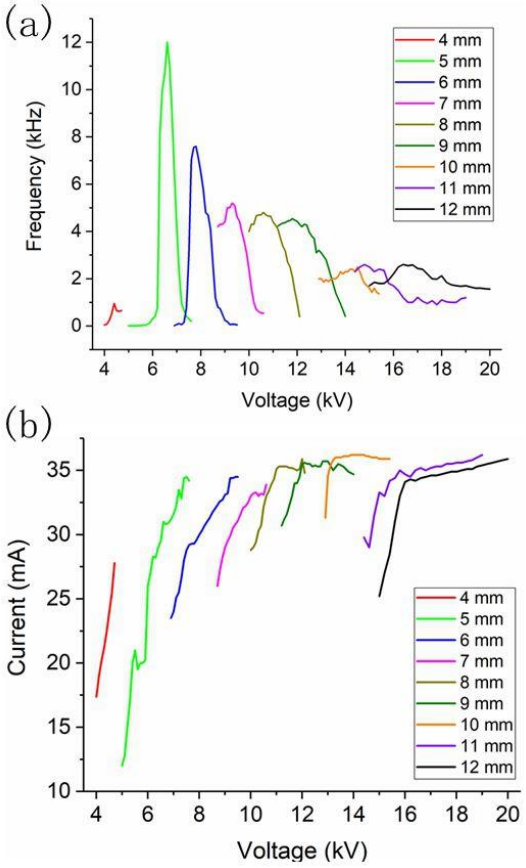

Fig 4-13. Frequency of current pulses vs. DC voltage at different gap distances with Teflon enclosure (a). Peak value of current pulses vs DC voltage at different gap distances with Teflon enclosure (b).

By comparing the operation of this plasma source with and without the Teflon enclosure, it can be concluded that a Teflon tube enclosure can greatly stabilize the current pulsations of pulsed corona source and expand the operational voltage range. It also enhances the pulsations by both increasing the pulsing frequency by one order of magnitude and peak current value. In

addition, it enables a pulseless region between the continuous current pulsing and strong sparks, which is important for practical applications where stable operation without sparks is desirable. The average power consumption of the pulsed corona in both cases is calculated as $P = f \int_{\text{one pulse}} I\,V dt$. Fig 4-14 shows a comparison of average discharge power with and without the Teflon enclosure for d = 5 mm. One can see that the operational voltage range is much wider with the application of a Teflon enclosure. In addition, the Teflon enclosure significantly increases the average discharge power from 10 mW up to 220 mW. Thus, it can be seen that the dielectric enclosure is able to enhance the discharge energy deposition by 22 times which can potentially increase the production of the active species and specific gas particles.

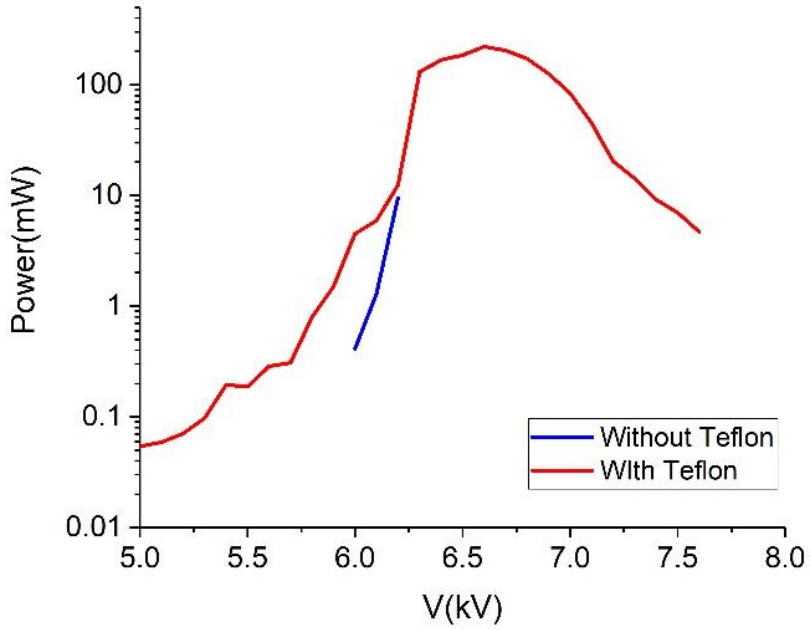

Fig 4-14. Comparison of the average discharge power with and without Teflon enclosure for 5 mm gap distance.

The effect of enhancement of pulsed corona using a dielectric enclosure can be potentially explained by the presence and accumulation of nitrogen metastable molecules N_2^* created during the discharge in the limited air volume in vicinity to the electrodes compare to an open volume in a common corona discharge (see Fig 4-8). Indeed, the Teflon enclosure tube inhibits these metastable molecules from diffusing away from the electrodes thus increasing the local concentration of metastable molecules in the vicinity of the electrodes [159]. Higher concentration

of the metastable molecules can cause production of more seed electrons due to the associative ionization mechanism [160]. These additional seed electrons thus enhance the avalanches developing in the front of the streamer head and cause streamer inception at lower electric fields on the anode tip.

Therefore, the enhanced pulsed corona discharge looks promising for nitrogen oxides and ozone generation because of higher energies deposited to the discharge in comparison to a normal corona discharge. For the latter, it's a well-known fact that it was used for ozone generation previously but now mostly replaced by generators based on a dielectric barrier discharge (DBD) because of power density and energy efficiency [161]. As we found before the enhanced pulsed corona consumes more than 20 times of electrical power than a normal one, thus we expected significant rise in ozone production in the enhanced pulsed corona regime and following experiments were conducted in order to confirm these speculations. The discharge had been placed in the additional acrylic case to cover the airstream as shown in Fig 4-10(b). It has to be noted, that stable operational range has slightly changed compared to that then the discharge was fully exposed to the stagnant ambient air. For gas analysis we picked an operational point where the gap was 10 mm, the DC voltage was 10-10.5 kV, and the resulting pulse repetition frequency was about 6 kHz. An average discharge consuming power in such regime is close to 220 mW or $1.4*10^{18}$ eV/s.

By varying air flow rate, ozone, nitric oxide and nitrogen dioxide concentrations were measured, as presented in Fig 4-15. The nitric oxide graph is not shown because its amount was always below the measuring limit of our equipment. Absence of nitric oxide has been predicted after we found a significant amount of ozone in the corona's exhaust. Indeed, in an ozone rich mixture NO quickly converts to NO_2 according to the following reaction [162]: $NO + O_3 \rightarrow NO_2 + O_2$.

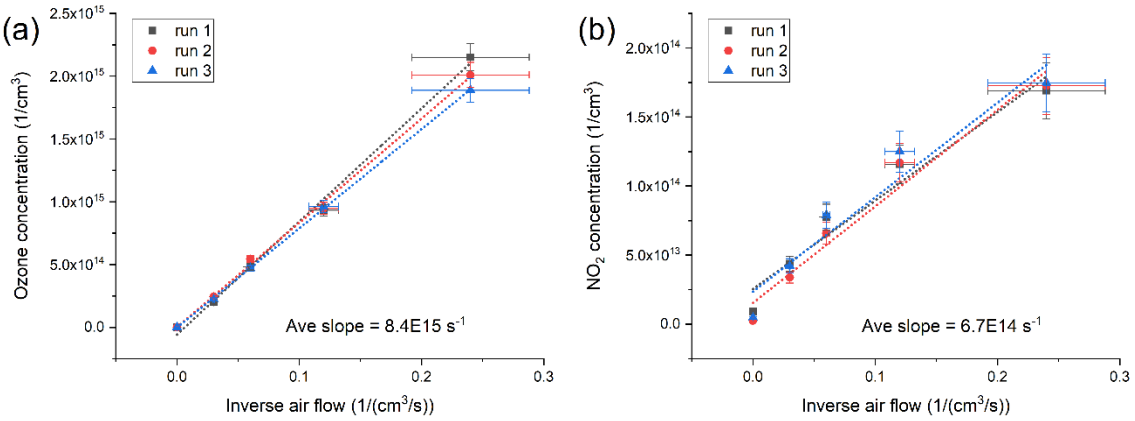

Fig 4-15. Ozone (a) and nitrogen dioxide (b) concentrations with respect to inverse air flow. The points with zero inverse air flow (or infinite air flow) correspond to plasma-off case.

According to the Fig 4-15(a), ozone concentration increased linearly with inverse air flow which is indicative of constant ozone production regardless of the air flow rate, but for NO_2 we see slightly non-linear behavior – low NO_2 than it should be at 0.5 and 0.25 l/min – it indicates the discharge does not have enough fresh air to successfully evacuate all the chemical products from the space around it at these pretty low flow rates.

If one approximates the line slope in the Fig 4-15, a molecule production rate in one second can be found. By dividing the average discharge power to the production rate, the energy cost per one molecule may be determined. The enhanced corona discharge has about 150 and 1950 eV/molecule production efficiencies for ozone and NO_2 respectively, what is higher than the values commercially available devices have, and previous data published. For instance in case of plasma ozone production, it has been reported to achieve around 30 eV/molecule for atmospheric air and much less, even 10 eV/molecule, for pure oxygen as an input [163]. For nitrogen dioxide, values less than 100 eV/molecule in gas phase has been reached [164].

Furthermore, the lifetime of the electrode was briefly investigated. It took the system approximately 2 hours until the level of current pulses decayed to zero which indicates a fully degradation of the electrode tip. It was observable that the tip of electrode was covered with black layer which is potentially the oxidation of the metal electrode. The electrode could be recovered by filing off this layer. Future work includes a more thorough investigation of the lifetime of the electrode and its cause including the utilization of other methods such as optical microscopy, SEM

for the surface observation, AFM for the surface roughness evaluation, EDX for the material species on the surface, etc.

4.2.5 Conclusion

In this work a DC-driven plasma device that utilizes pulsed corona discharges was studied, and the effect of the Teflon enclosure between electrodes in order to control the characteristics of the discharge was demonstrated. It was shown that a Teflon enclosure can increase the amplitude and frequency of current pulses. At a gap distance of 5 mm, the average discharge power was increased from 10 to 220 mWatt due to the Teflon enclosure. In addition, use of the Teflon enclosure causes a significantly more stable operation of the discharge. The product reactive gases of the enhanced pulsed corona were tested to be mostly ozone with traceable amount of NO_2. The discharge uses about 150 eV and 1950 eV per one ozone molecule and nitrogen dioxide molecule, respectively.

4.3 Study of atmospheric pressure plasma jet parameters generated by DC voltage driven cold plasma source.

Xingxing Wang, and Alexey Shashurin
Purdue University, School of Aeronautics and Astronautics, West Lafayette, IN 47907, USA

This chapter was previously published in Journal of Applied Physics
DOI: 10.1063/1.4986636

4.3.1 Abstract

In this work, plasma and discharge parameters of a DC voltage driven cold plasma source were measured. The device exhibits a plasma jet with a length of 3 cm and a pulsation frequency of about 2.75 kHz. The peak current of each pulse was about 1.1 mA and the duration was about 5 μs. The repetition rate could be increased by raising the DC voltage level. By utilizing the microwave scattering system, electron density in the plasma was measured to be about ~10^{11} cm^{-3}. Vibrational and rotational temperatures of the APPJ were also measured by optical emission spectroscopy (OES). The vibrational temperature was measured to be 2850 K and rotational

temperature to be 300K at the applied voltage of 5 kV. No strong dependence of the temperatures was found with the DC voltage level.

4.3.2 Introduction

Atmospheric pressure plasma jets (APPJ) has become a very popular research topic after it was discovered to have a wide application in the field of bio-engineering, medicine, food processing, etc [114] [15] [116] [146] [147]. It has been successfully used for sterilization purposes in those fields. In addition, it exhibits other advantages over traditional means of sterilization, such as steam or chemicals. The APPJ leaves no residuals, making it perfect for the sterilization of punctured wounds as chemicals may cause extend damage to the wounds [119]. Furthermore, APPJ was also found to be applicable in treating various types of cancers and tumors, etc [15] [116] [119] [120] [121].

Conventional APPJs are excited in helium flow exhausted into open air. The APPJs are traditionally generated by repetitive pulsed discharges with a frequency typically in the range of 10s of kHz. This pulsation frequency is controlled by the frequency of the periodic discharge-driving voltage [37] [124] [125] [126] [127] [128] [129]. A streamer formed at each breakdown propagates at the velocity of 10^6-10^8 cm*s^{-1} for several centimeters until the local fraction of O_2 is about 1% in the jet [165]. Typical electron density inside of the jet is in the range of 10^{12}-10^{13} cm^{-3} and the heavy particles are near room temperature at 300-350 K [37].

Traditionally the APPJs are driven by AC or pulsed-DC HV operating in the kV range, but such power sources have certain disadvantages. Firstly, the time-varying power sources of the system are often associated with high cost, especially if a wide range of operating frequency is required. Another downside of the application of AC/pulsed-DC HV is that there are serious safety concerns with their operation [166]. The use of time-varying HV sources reduces resistance of insulating shields due to the capability of displacement current conduction and increases danger of electric shock. Thirdly, operating the time-varying HV sources causes EMI with other sensitive electronics nearby that can potentially be disastrous during some medical procedures [167]. In comparison, APPJs driven by DC high voltage are free from the above disadvantages due to relief of requirements to the electrical insulation thickness, availability of large number of commercially offered power supplies and significant reduction of the EM radiation.

Previously, we found that by using DC high voltage, the APPJ can be generated in the form of pulses [157]. For each breakdown, the current pulse had a duration of 3 μs and a peak value of 0.2 mA. The frequency of the pulses was in the range of 2-10 kHz and could be controlled by applying different discharge geometries and by varying the helium flow rate, while keeping the applied DC voltage constant. The device operates in a self-oscillatory mode at which breakdowns will initiate every time when the electric field near the HV electrode reaches the threshold value. After the breakdown, a streamer initiates and a positive potential column is established along the path of the streamer, building up a channel of positive space charge. The streamer later stops propagating but the remaining positive space charge still retains the electric field near the cathode under the threshold value. Later the positive charges decays, electric field near the cathode restores and the next cycle of breakdown starts.

Therefore, atmospheric-pressure plasma jet driven by DC high voltage and ways to control the streamer firing rate were demonstrated previously. However, plasma properties were not studied. In this paper, we report measurements of plasma and discharge characteristics of DC voltage driven cold plasma source, namely total electron number, electron density, vibrational/rotational temperatures and temporal dynamics of discharge current and voltage.

4.3.3 Methods and equipment

DC voltage driven cold plasma device. The schematics of the device are shown below in Figure 4-16. DC high voltage up to 5 kV was supplied by a Bertan 225 power supply to the central high voltage electrode, while a piece of copper foil wrapped outside the nozzle was used to provide the ground. A 10 kΩ shunt resistor was connected in series in the HV line for the measurement of current. A voltage probe (Lecroy PPE6kV) was hooked at each end of the resistor to monitor current and voltage. The helium flow into the device was controlled by a mass flow controller (MFC) (Alicat MC-10SLPM). The helium flow rate during the experiment was chosen to be 5 LPM, since operation of the source at lower flow rates (<3 LPM) caused strong arcing between the electrodes, and at higher flow rates (>6 LPM) the APPJ turned into turbulent without enhancement of its length or brightness.

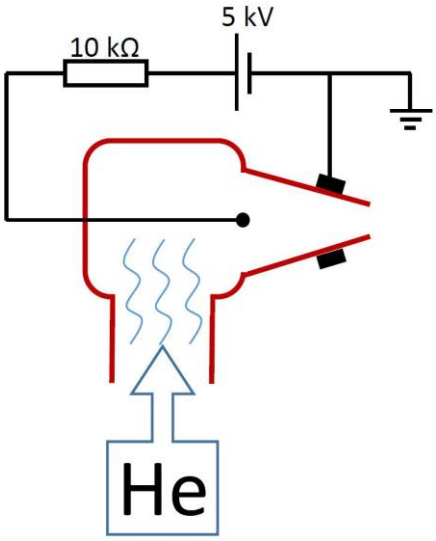

Figure 4-16. Schematic of the DC driven plasma device

Several electrode geometries were tested to maximize intensity and length of the plasma jet. As result, the diameter of the central hole and the ground electrode were chosen to be 3 mm and 9.2 mm respectively. The final version of the DC driven plasma device is shown in Figure 4-17, in standby and in operation. The device utilizes a single coaxial HV wire and a gas line. When the device was operating, the length of the APPJ was about 3 cm.

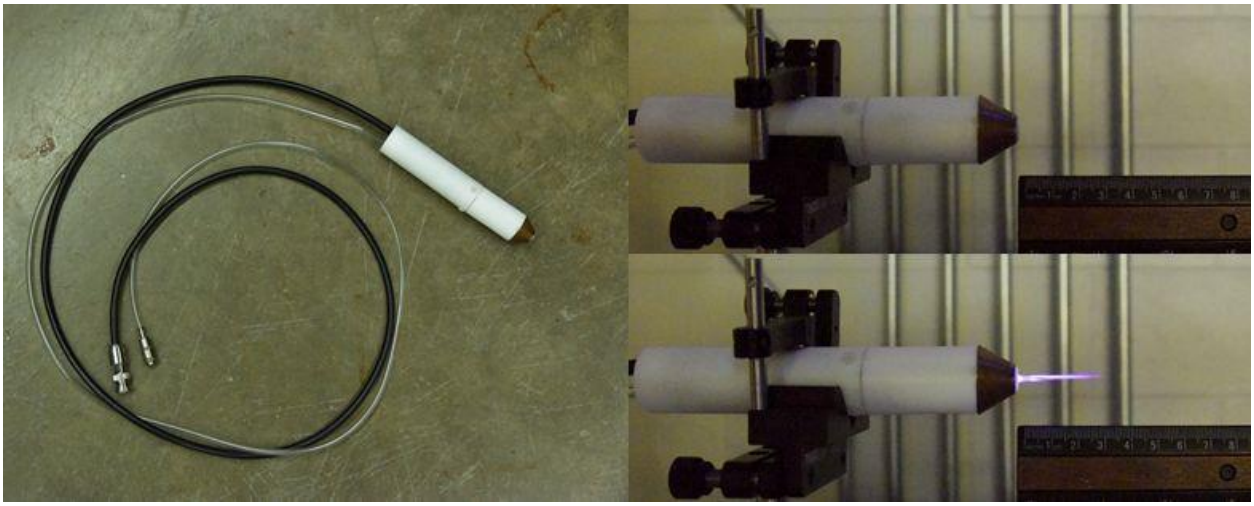

Figure 4-17. DC driven plasma device when DC voltage was 5 kV and helium flow rate was 5 LPM

Rayleigh Microwave Scattering System. A Rayleigh microwave scattering (RMS) system was utilized to measure the total electron number (N_e) and electron density (n_e) within the APPJ [56]. The method is based on the elastic scattering of the microwaves off the plasma volume. The scattered radiation is created as result of polarization of the plasma channel in the external microwave field. For the thin plasma channel, when amplitude of microwave field is nearly uniformly distributed inside the plasma, the radiation in far-field is equivalent to the Hertz dipole radiation. Overall, such a process is analogous to elastic Rayleigh scattering of light, when radiation wavelength significantly exceeds the scatterer size. Amplitude of the signal scattered from the plasma is proportional to the total electron numbers in the plasma volume. RMS system calibrated using dielectric scatterers with known physical properties can be used to determine absolute values of electron numbers N_e and number densities n_e as detailed [37] [56].

The schematics of the microwave scattering system is shown in Figure 4-18. A horn antenna was used to radiate microwave onto testing object as well as to receive the scattered signal. Two outputs I (in-phase) and Q (quadrature) from an I/Q mixer were used to determine output signal U_{out} proportional to the amplitude of the scattered field as: $U_{out} = \sqrt{I^2 + Q^2}$. It can be shown that U_{out} is related to the properties of plasmas and dielectric scatterers as followed [37] [168] [35]:

$$U_{out} = \begin{cases} A\frac{e^2}{\nu}N_e, & for\ plasma \\ AV\varepsilon_0(\varepsilon - 1)\omega, & for\ dielectric\ scatterers \end{cases} \quad (7)$$

A: proportionality coefficient

V: volume of the dielectric material

ε_0: vacuum permittivity

ν: collisional frequency

ε: relative permittivity

ω: frequency of microwave

Before applying the RMS system to measurements of the plasma jet parameters, proportionality coefficient A was determined using dielectric scatterers made of Teflon. Teflon bullets (ε = 2.1, diameter 3.2 mm) driven by a pneumatic gun flying in a path 15 cm away perpendicular to the horn were used for calibration. The value of A was found to be $6.623 *$

$10^2 \frac{V*s}{cm^2*F}$ using the bottom relation of Equation 1. Then, top expression of the Equation 1 was used to determine N_e. Using collision frequency estimation $1.46*10^{12}$ s^{-1} [58], it can be re-written to the following form:

$$N_e = U_{out}[Volts] * 2.072 * 10^{12} \quad (8)$$

If the volume of the plasma V_0 is known, average plasma density n_e can then be determined by:

$$n_e = \frac{N_e}{V_0} \quad (3)$$

A frequency sweep was done and the operation frequency was chosen to be 10.707 GHz as the system generated minimal signal by the reflection from the surroundings and its components. The distance between the horn antenna and plasma jet was set to be 15 cm to ensure that the wave front of the electric field was flat when hitting the APPJ [56] [168].

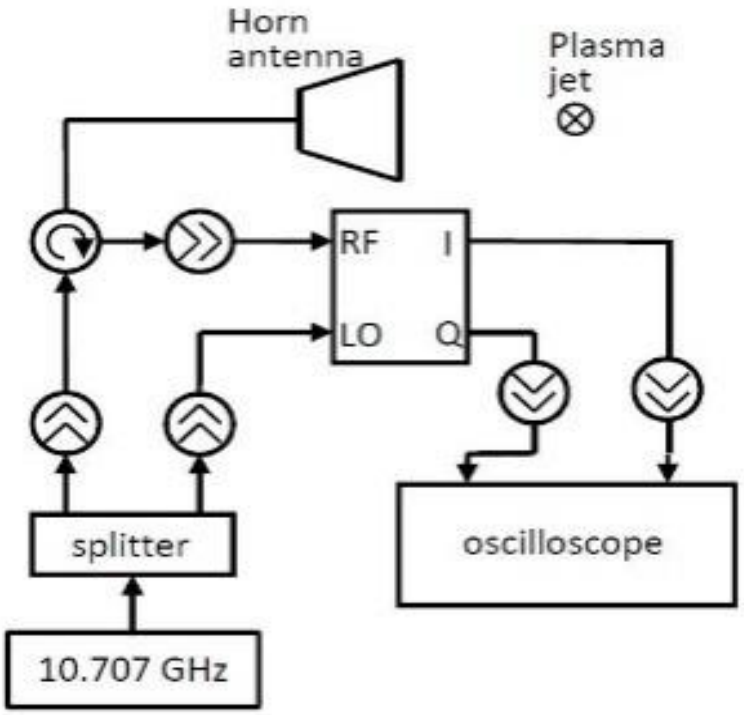

Figure 4-18. Setup of the Rayleigh Microwave Scattering system

Optical Emission Spectroscopy. A spectrometer (Princeton Instrument Acton SpectraPro SP-2500) was utilized to measure the rotational and vibrational temperatures of the APPJ. The spectrum of the nitrogen second positive system ($C^3\Pi_u \rightarrow B^3\Pi_g$) was measured. The wavelength

range of 362 – 382 nm was chosen to record spectral band with $\Delta v = v'-v'' = -2$. Lenses (AF-S Micro NIKKOR 40mm 1:28G and a 10x magnifier) and extension (~5 cm) were used at the end of the optic fiber cable to ensure that focused APPJ image was located exactly in the plane where optic fiber entrance was placed. This approach greatly improved signal-noise ratio. The setup of the OES measurement system is shown in Figure 4-19. SPECAIR was used to do the fittings to find the vibrational and rotational temperatures, T_{vib} and T_{rot} respectively.

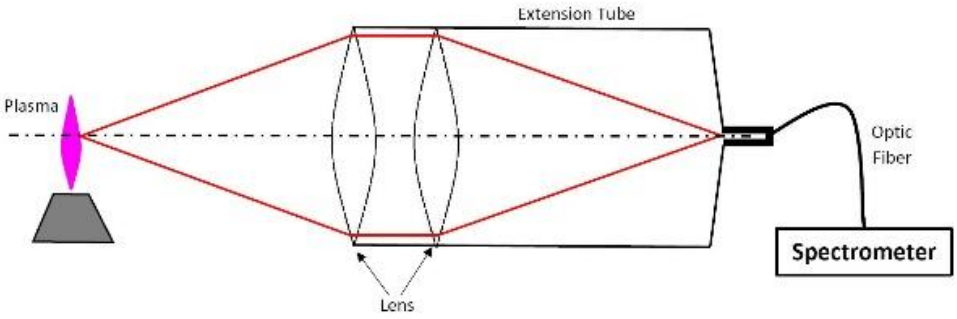

Figure 4-19. Setup of the optics for OES measurement

4.3.4 Results and discussion

Figure 4-20 shows the temporal evolution of discharge voltage, discharge current, total electron number in plasma jet N_e and an image of streamer propagation. One can see from Figure 4-20 that sequence of the breakdowns at a frequency of about 2.75 kHz was generated at application of 5 kV DC voltage and each current pulse had an amplitude of about 1.0-1.2 mA. A close look of the voltage (green), current (blue) and total number of electrons N_e (red) of an individual breakdown is shown in Figure 4-20(a). It can be observed that the current pulse duration was about 5 μs and the voltage was constant at 5 kV during the breakdown. The peak value of N_e was about $6.5*10^9$ and the rise of N_e was delayed by approximately 2 μs from the moment of discharge current maximum. The propagation of the streamer captured in a single breakdown event using ICCD camera (Princeton Instruments PI-MAX4) is shown in Figure 4-20(b). The black rectangles in Figure 4-20(a), t1-t5, represent the moments at which images shown in Figure 4-20(b) were taken. The multiple locations of a singular streamer tip are also labeled in Figure 4-20(b) respectively. The average velocity of the streamer propagation was estimated to be around $6.67*10^5$ cm/s. Comparing with the plasma jet parameters reported in ref [169], the visible length

of the jet was extended by three times, the peak value of current increased by about ten times, duration of the pulses also was slightly expanded, and the repetition frequency decreases from 15 kHz to 2.75 kHz.

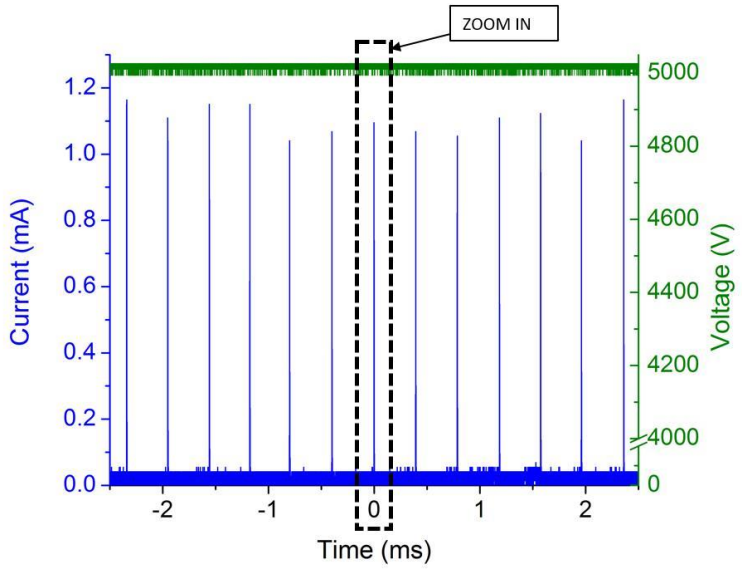

Figure 4-20. Waveforms of current and voltage of series streamer breakdowns. Current is generated in pulses with a constant 5 kV applied voltage. The region marked in dashed rectangle is presented in Figure 4-21.

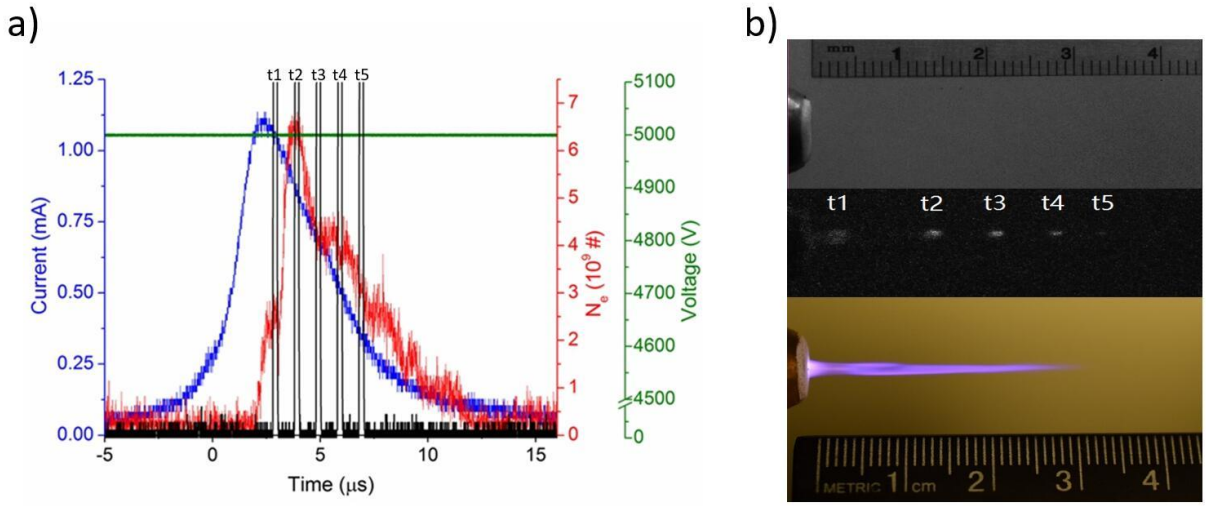

Figure 4-21. (a) Waveforms of current, voltage, and N_e from a single streamer breakdown. [t1]-[t5] represents the times periods when the intensifier of the ICCD camera is working. (b) Photograph of the streamer at certain times from [t1] to [t5]. This image is taken during a single breakdown.

The correlation between the time between the breakdowns T_{rep} and the applied voltage is shown in Figure 4-22. One can see from Figure 4-22 that, as voltage increases, T_{rep} decreases. The range of voltage adjustment was between 4.5 kV and 5 kV, since intensity of the plasma jet greatly reduced below 4.5 kV, while voltage above 5 kV resulted in periodic arcing events terminating plasma jet to the ground electrode. T_{rep} decreased from 1500 μs to 500 μs with voltage increase from 4.5 to 5 kV, which can be explained by faster recovery of the electric field on the HV electrode to the breakdown threshold value when the electrode carried higher potential. In addition, vertical error bars indicate larger variability of the time between the breakdown events at lower voltages.

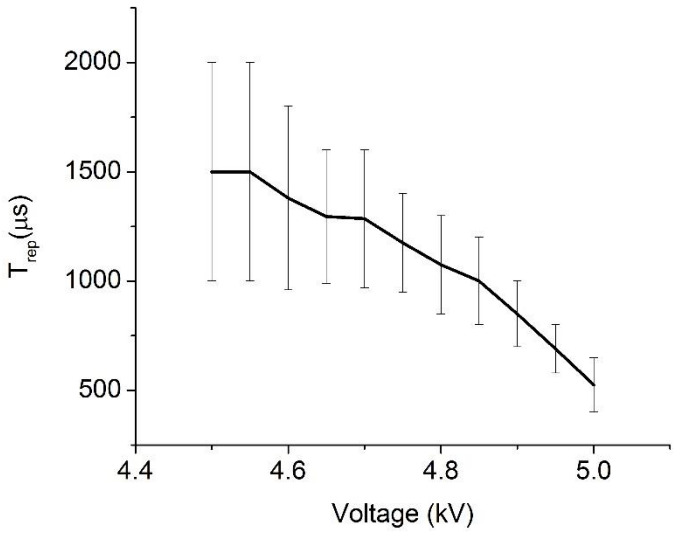

Figure 4-22. T_{rep} of the streamer breakdown vs. the applied voltage

Average plasma density n_e in the plasma jet was determined as $n_e = \frac{N_e}{V_0}$ using constant plasma volume V_0=0.05 cm^3 (cylinder with 0.2 cm diameter and 1.5 cm height). This model for the plasma volume was taken based on the following observation. One can see in Figure 4-20(a) that total number of plasma electrons in the plasma volume start decreasing at t=4 μs well before the streamer reached its maximal length of 3 cm at t=7 μs. This fact clearly indicates that root of the streamer channel experienced decay during streamer propagation, since otherwise total electron numbers N_e would increase until maximal streamer length is reached at t=7 μs. Therefore,

length of the plasma channel corresponding to the moment of time t=4 μs was chosen in this estimation, namely 1.5 cm. Proposed here approach might underestimate initial values of plasma density on times t<4 μs.

Based on the assumptions and calculations above, n_e can now be plotted. Figure 4-23 below shows the evolution of n_e (purple) with respect to time along with the change of current and N_e. One can see from Figure 4-23 that, the trend of n_e overlaps with the trend of N_e, reaching a maximum value of $1.4*10^{11}$ cm^{-3} about 2 μs after current reaches its peak.

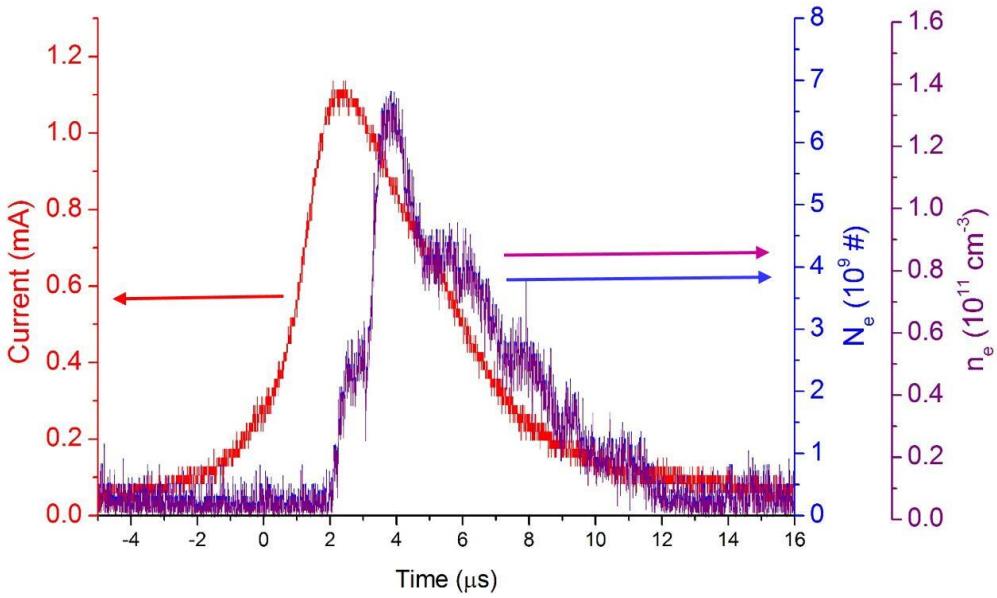

Figure 4-23. Waveforms of current, N_e and n_e from one streamer breakdown

It is interesting to see how the strength of the breakdown changes with the applied voltage. The maximum values of current and n_e in a single pulse breakdown with respect to the applied voltage are shown in Figure 4-24 when varying the voltage from 4.5 kV to 5 kV. One can see that both the peak current and peak n_e increase with the applied voltage, and they follow a similar trend. Peak current increases from 0.65 mA to 1.15 mA and maximum of n_e increases from $1.7*10^{11}$ cm^{-3} to $3.5*10^{11}$ cm^{-3}.

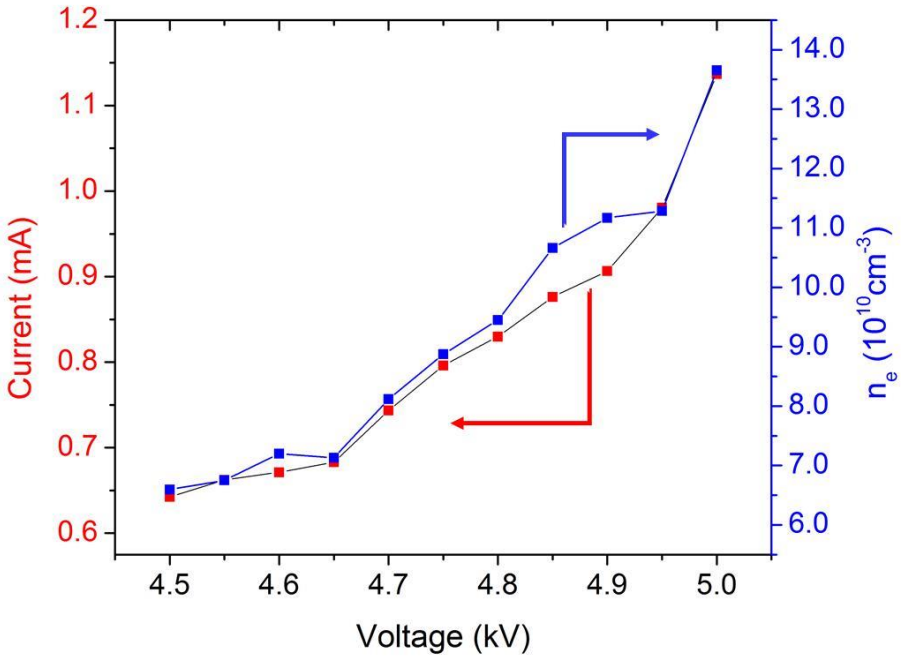

Figure 4-24. Maximum of current and n_e vs applied voltage

A sample of the spectrum is shown in Figure 4-25(a), when the applied voltage was 5 kV, along with the best fitting from SPECAIR. The resulted T_{vib} was 2847 K and T_{rot} was 303 K. After running SPECAIR for the spectrum at applied voltages ranging from 4.7 kV to 5 kV, it was found that there was no strong dependence of T_{vib} and T_{rot} on the applied voltage. T_{vib} was in the range of 2675±175 K and T_{rot} was in the range of 338±38 K. The resulted plot is shown in Figure 4-25(b).

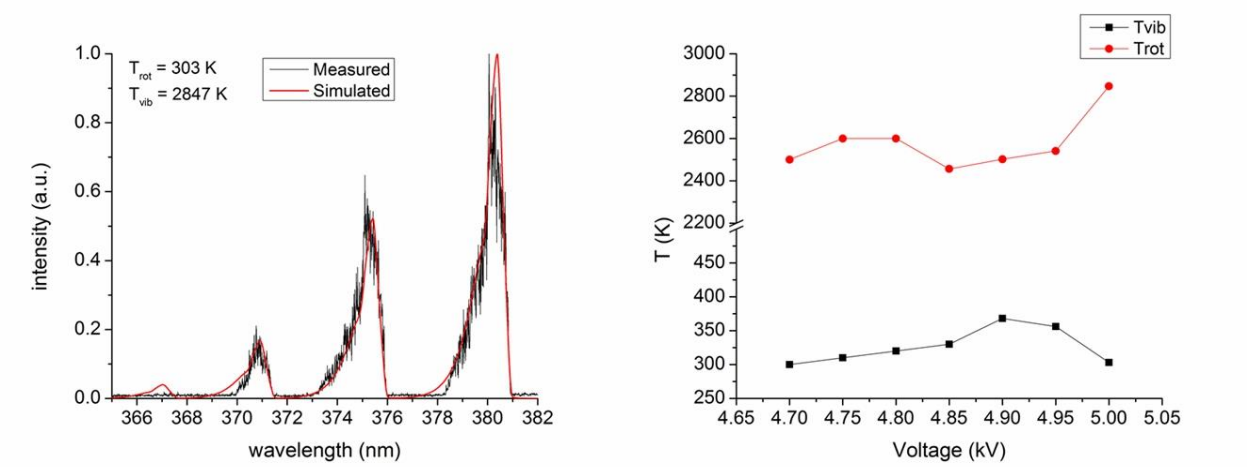

Figure 4-25. Measurement by OES. (a) Measured and simulated spectrum when applied voltage was 5 kV. (b) T_{rot} and T_{vib} when applied voltage is between 4.7 kV and 5 kV.

4.3.5 Conclusion

DC voltage driven cold plasma source tested in this work exhibits a jet with a length of 3 cm and a pulsation frequency of about 2.75 kHz when 5 kV DC driving voltage is used. The peak current of each pulse was about 1.1 mA and the duration was about 5 μs. As the applied voltage increased, repetition rate increased and breakdowns became more repeatable. By utilizing a microwave scattering system, the electron density n_e of the APPJ was measured. Peak value of the plasma density was about $1.4*10^{11}$ cm^{-3} at the applied voltage of 5 kV. Optical emission spectroscopy was employed to measure the vibrational/rotational temperatures. At the applied voltage of 5 kV, T_{vib} was found to be 2847 K and T_{rot} to be 303 K.

5 CONCLUSIONS

5.1 Summary

To conclude, a comprehensive study on the nanosecond HV discharge with pin-to-pin configuration was first conducted at atmospheric conditions. Two discharge regimes, namely, spark and corona, were able to be distinguished by multiple discharge parameters and visual presentation. Spark regime was achieved at smaller gap distances (<6mm) with larger pulse energy per gap distance (0.6-1 mJ/mm). A secondary breakdown could be observed during the later stage of the 90ns HV pulse, associated with the transition from the nanosecond spark regime to the cathodic arc regime. During steady-state operation before the second breakdown, a dynamic balance between the generation and removal of electrons could be reached based on the corresponding conduction current and local reduced field. The energy deposition during the secondary breakdown event is less efficient than the nanosecond spark regime, which can be deliberately prevented by shrinking the pulse width below 70 ns. The characteristic decay time of the electrons after the HV pulse is around 150-200 ns which is contributed by both dissociative recombination and three-body attachment. Decay for later stage is governed by attachment (1-2μs after) due to the drop of electron density. In addition, plasma produced within the spark regime tends to have a higher temperature and has a trend towards equilibrium condition with decreasing gap distance. Furthermore, the influence of the memory effect begins to be noticeable at a repetition frequency higher than 1 kHz, which results in an increase in local gas temperature and a drop in gas density. At higher repetition frequencies, a slower decay rate and lower electron number density were observed, the latter of which however corresponds to a higher ionization degree. On the other hand, the operation of nanosecond discharges within corona regime could be achieved at larger gap distances (>8mm) with lower pulse energy per gap distance compared to the spark regime (~0.1 mJ/mm). The resulted production of electrons and gas heating were also less profound in comparison.

Secondly, a flashing corona type APPJ driven by pure DC high voltage was studied. It was demonstrated that a helium APPJ device was operable with a constant DC high voltage when streamer discharges were triggered in the kHz range in an auto-oscillatory mode. This type of APPJ is advantageous over traditional APPJs, which are driven by time-varying power supplies.

The temperature and electron number density of the APPJ were measured to be <400 K, ~10^{11} cm^{-3}, respectively. It was also demonstrated that a dielectric enclosure could enhance the intensity of the flashing corona with regard to its triggering frequency and discharge current level. This signifies the direction of the DC-driven APPJ development when extensive production of active gas species is desired for sterilization-related applications.

5.2 Recommendation for future work

This section presents a list of recommended work to further investigate NRP discharges and DC-driven APPJs.

NRP pin-to-pin discharge:

1. The lower bound of the gap distance studied was 2mm. Based on the trend derived, it has been observed that a higher temperature and electron number density can be achieved at smaller gaps. Thus, it is valuable to study the discharges at even shorter gaps where a fully-ionization and thermal plasma can potentially be realized.
2. Electron temperature is a parameter that was not directly measured in this work but instead estimated based on literature. Since it is one of the most critical parameters that affect the evaluation of both collisional frequency (total electron number) and attachment/recombination coefficient (decay rate), it is valuable to directly measure the electron temperature of this particular discharge so that the dynamics of the electrons can be more accurately presented.
3. Discharge parameters such as gas temperature and density shall be measured at multiple locations of the plasma. This 'map' of the parameters will be more beneficial for future references as well as source data for simulation.

DC-driven APPJ:

1. APPJs are much appreciated in sterilization applications for their ability to produce certain gas species. Thus, it is necessary to evaluate the production of gas species by the DC-driven APPJ in terms of types of species and their concentrations before actual implementation of this APPJ in a certain scenario.

2. For industrial application of DC-driven APPJ, one should also consider device up-scaling in which multiple jets can be generated to multiply the gas species production. One potential route is to connect multiple APPJ devices in parallel to one power supply.

PUBLICATIONS AND PRESENTATIONS

Peer-reviewed Journals

1. X. Wang, A. Patel, and A. Shashurin, “Combined microwave and laser Rayleigh scattering diagnostics for pin-to-pin nanosecond discharges”, Journal of Applied Physics, **129**, 183302, 2011.
2. X. Wang, and A. Shashurin, "Gas Thermometry by Optical Emission Spectroscopy Enhanced with Probing Nanosecond Plasma Pulse", AIAA Journal **58**, 7(2020)
3. X. Wang, A. Khomenko, and A. Shashurin, "Enhancement of positive pulsed corona by dielectric enclosure ", AIP Advances **9**, 105029 (2019)
4. X. Wang, P. Stockett, R. Jagannath, S. Bane and A. Shashurin, "Time-resolved measurements of electron density in nanosecond pulsed plasmas using microwave scattering", Plasma Sources Sci. Technol. **27** (2018) 07LT02
5. X. Wang and A. Shashurin, “DC-driven plasma gun: self-oscillatory operation mode of atmospheric–pressure helium plasma jet comprised of repetitive streamer breakdowns”, Plasma Sources Sci. Technol. **26**, 02LT02 (2017).
6. X. Wang and A. Shashurin, “Study of atmospheric pressure plasma jet parameters generated by DC voltage driven cold plasma source”, Journal of Applied Physics **122**, 063301 (2017).
7. A. Khomenko, V. Podolsky and X. Wang, “Different approaches of measuring high-voltage nanosecond pulses and power delivery in plasma systems”, Electr Eng (2020). https://doi.org/10.1007/s00202-020-01058-8
8. A. Sharma, M. N. Slipchenko, M. N. Shneider, X. Wang, K. A. Rahman & A. Shashurin, "Counting the electrons in a multiphoton ionization by elastic scattering of microwaves", Sci Rep **8**, 2874 (2018).

Conference Papers/presentations

1. X. Wang and A. Shashurin, “Temporally resolved measurements of gas temperature using optical emission spectroscopy enhanced with probing nanosecond plasma pulse”, AIAA Scitech 2020 Forum
2. X. Wang and A. Shashurin, “Study of the transition between modes of nanosecond repetitive pulsed discharge”, AIAA Aviation 2019 Forum
3. X. Wang and A. Shashurin, “Thomson microwave scattering for electron number density diagnostics of miniature plasmas at low pressure”, AIAA Aviation 2019 Forum
4. X. Wang and A. Shashurin, “Experimental Study of Modes of Operation of Nanosecond Repetitive Pulsed Discharges in Air”, AIAA Scitech 2019 Forum
5. X. Wang and A. Shashurin, “Study of Atmospheric Pressure Plasma Jet Driven by DC High Voltage”, AIAA Scitech 2018 Forum

APPENDIX A –VIBRATIONAL TEMPEARTURE OF N_2 AT GROUND STATE

It is important to note that, by utilizing SPS of N_2 for the evaluation of temperature, T_{vib} measured in this work represents the vibrational temperature of nitrogen in C state instead of ground state (X). By assuming that the N_2(C) is mainly excited from N_2(X), one can evaluate T_{vib} for N_2(X) using Frank-Condon factor for N_2(C→X) transition. The table of the Frank-Condon factor is provided below in **Table 2**, and the resulted correlation between T_{vib}(C) and T_{vib}(X) is plotted down below in **Fig 5-1**. However, it is important to ensure the validity of the assumption that N_2(C) is mainly excited from N_2(X) which may not be true under all circumstances. For plasma cases where Ar is present, N_2(C) can be also excited from Ar* by: $N_2(X) + Ar^* \rightarrow N_2(C) + Ar$. Thus, a direct correlation between N_2(X) and N_2(C) cannot be built.

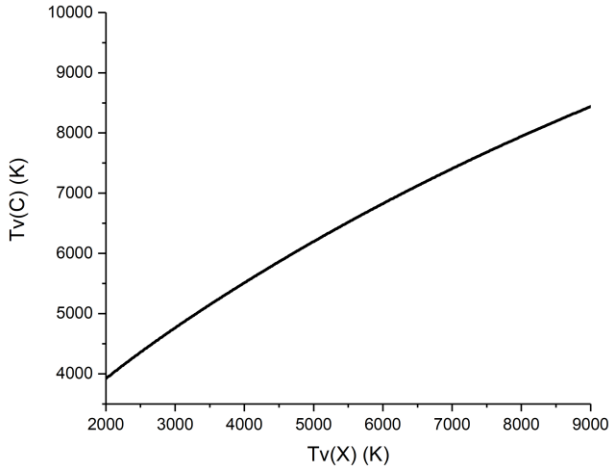

Fig 5-1. Vibrational temperature of C state vs vibrational temperature at ground (X) state

Table 2. Frank-Condon coefficients for nitrogen Tanaka band system (C-X)

	$v'' = 0$	$v'' = 1$	$v'' = 2$	$v'' = 3$	$v'' = 4$	$v'' = 5$
$v' = 0$	5.59E-01	3.36E-01	9.03E-02	1.33E-02	1.12E-03	6.28E-05
$v' = 1$	3.03E-01	8.73E-02	3.64E-01	1.95E-01	4.47E-02	5.84E-03
$v' = 2$	1.01E-01	2.71E-01	1.82E-03	2.44E-01	2.67E-01	9.52E-02
$v' = 3$	2.76E-02	1.82E-01	1.30E-01	7.11E-02	9.92E-02	2.80E-01
$v' = 4$	7.16E-03	7.88E-02	1.82E-01	2.42E+02	1.48E-01	9.47E-03

REFERENCES

[1] S. Samukawa, M. Hori, S. Rauf, K. Tachibana, P. Bruggenman, G. Kroesen, J. C. Whitehead, A. B. Murphy, A. F. Gutsol, S. Starikovskaia, U. Kortshagen, J. P. Boeuf, T. J. Sommerer, M. J. Kushner, U. Czarnetzki and N. Mason, "The 2012 plasma roadmap," *Journal of Physics D-Applied Physics*, vol. 45, no. 37, 2012.

[2] M. Laroussi and T. Akan, "Arc-free atmospheric pressure cold plasma jets: a review," *Plasma Process. and Polym.*, vol. 4, pp. 777-788, 2007.

[3] A. Schutze, J. Y. Jeong, S. E. Babayan, J. Park, G. S. Selwyn and R. F. Hicks, "The atmospheric-pressure plasma jet: a review and comparison to other plasma sources," *IEEE Trans. Plasma Sci.*, vol. 26, no. 6, 1998.

[4] X. Li and M. Farid, "A review on recent development in non-conventional sterilization technologies," *Jounal of Food Engineering*, vol. 182, pp. 33-45, 2016.

[5] A. Fridman, Plasma Chemestry, Cambridge: Cambridge University Press, 2008.

[6] N. D. Geyter and R. Morent, "Nonthermal plasma sterilization of living and nonliving surfaces," *Annu. Rev. Biomed. Eng.*, vol. 14, pp. 255-274, 2012.

[7] G. Fridman, G. Friedman, A. Gutsol, A. B. Shekhter, V. N. Vasilets and A. Fridman, "Applied Plasma Medicine," *Plasm Process. Polym.*, vol. 5, no. 6, pp. 503-533, 2008.

[8] S. Singh, R. Chandra, S. Tripathi, H. Rahman, P. Tripathi, A. Jain and P. Gupta, "The bright future of dentistry with cold plasma - Review," *IOSR Journal of Dental and Medical Scieneces*, vol. 13, no. 10, pp. 06-13, 2014.

[9] W. Kim, M. G. Mungal and M. A. Capelli, "The role of in situ reforming in plasma enhanced ultra lean premixed methan/air flames," *Combustion and Flame*, vol. 157, pp. 374-383, 2010.

[10] Q. L. Pham, D. A. Lacoste and C. O. Laux, "Stabilization of a premixed methane-air flame using nanosecond repetitively pulsed dishcarges," *IEEE Transaction on Plasma Science*, vol. 39, pp. 2264-2265, 2011.

[11] G. L. Pilla, D. A. Lacoste, D. Veynante and C. O. Laux, "Stabilization of a swirled propane-air flame using a nanosecond repetitive pulsed plasma," *IEEE Transactions on Plasma Science*, vol. 36, pp. 940-941, 2008.

[12] O. V. Penkov, M. Khadem, W. Lim and D. Kim, "A review of recent applications of atmospheric pressure plasma jets for materials processing," *J. Coat. Technol. Res.,* vol. 12, no. 2, pp. 225-235, 2015.

[13] D. V. Roupassov, A. A. Nikipelov, M. M. Nudnova and A. Y. Starikovskii, "Flow separation control by plasma actuator with nanosecond pulsed-periodic discharge," *AIAA Journal,* vol. 47, p. 1680185, 2009.

[14] J. Little, K. Takashima, M. Nishihara, I. Adamovich and M. Samimy, "Separation control with nanosecond-pulse-driven dielectric barrier discharge plasma actuators," *AIAA Journal,* vol. 50, pp. 350-365, 2012.

[15] M. Laroussi, "The Biomedical Applications of Plasma: A Brief History of the Development of a New Field of Research," *IEEE Tans. Plasma Sci.,* vol. 36, no. 4, pp. 1612-1614, 2008.

[16] M. G. Kong, G. Kroesen, G. Morfill, T. Nosenko, T. Shimizu, J. van Dijk and J. L. Zimmermann, "Plasma medicine: an introductory review," *New Journal of Physics,* vol. 11, no. 115012, 2009.

[17] M. Laroussi, "Low-temperature plasma jet for biomedical applications: a review," *IEEE Trans. on Plasma Sci.,* vol. 43, no. 3, pp. 703-712, 2015.

[18] Y. P. Raizer, Gas Discharge Physics, Berlin: Springer-Verlag, 1991, pp. 350 - 352.

[19] A. F. H. van Gessel, B. Hrycak, M. Jasinski, J. Mizeraczyk, J. J. A. M. van der Mullen and P. J. Bruggeman, "Temperature and NO density measurements by LIF and OES on an atmospheric pressure plasma jet," *J. Phys. D: Appl. Phys.,* vol. 46, no. 095201, 2013.

[20] M. Qian, C. Ren, D. Wang, J. Zhang and G. Wei, "Stark broadening measuremnet of the electron density in an atmospheric pressure argon plasma jet with double-power electrodes," *J. Appl. Phys.,* vol. 107, no. 063303, 2010.

[21] A. F. H. v. Gessel, E. A. D. Carbone, P. J. Bruggeman and J. J. A. M. v. d. Mullen, "Laser scattering on an atmospheric pressure plasma jet: disentagling Rayleigh, Raman and Thomson scattering," *Plasma Sources Sci. Technol.,* vol. 21, no. 015003, 2012.

[22] A. Shashurin, M. N. Shneider, A. Dogariu, R. B. Miles and M. Keidar, "Temporary-resolved measurement of electron density in small atmospheric plasma," *Appl. Phys. Lett.,* vol. 96, no. 171502, pp. 1-3, 2010.

[23] S. M. Starikovskaia, N. B. Anikin, S. V. Pancheshnyi, D. V. Zatsepin and A. Y. Starikovskii, "Pulsed breakdown at high overvoltage: development, propagation and energy branching," *Plasma Sources Sci. Technol.,* vol. 10, pp. 344-355, 2001.

[24] E. I. Mintoussov, S. J. Pendleton, F. G. Gerbault, N. A. Popov and S. M. Starikovskaia, "Fast gas heating in a nitrogen-oxygen discharge plasma: II. Energy exchange in the afterglow of a volume nanosecond discharge at moderate pressure," *J. Phys. D: Appl. Phys.*, vol. 44, no. 285202, 2011.

[25] N. A. Popov, "Fast gas heating in a nitrogen-oxygen discharge plasma: I. Kinetic mechanism," *J. Phys. D.: Appl. Phys.*, vol. 44, no. 285201, 2011.

[26] D. Z. Pai, D. A. Lacoste and C. O. Laux, "Transitions bewteen corona, glow, and spark regimes of nanosecond repetitively pulsed discharges in air atmospheric pressure," *J. Appl. Phys.*, vol. 107, no. 093303, 2010.

[27] D. L. Rusterholtz, D. A. Lacoste, G. D. Stancu, D. Z. Pai and C. O. Laux, "Ultrafast heating and oxygen disssociation in atmospheric pressure air by nanosecond repetitively pulsed discharges," *J. Appl. D: Appl. Phys,* vol. 46, no. 464010, 2013.

[28] R. M. v. d. Horst, T. Verreycken, E. M. v. Veldhuizen and P. J. Bruggeman, "Time-resolved optical emission spectroscopy of nanosecond pulsed discharges in atmospheric-pressure N2 and N2/H2O mixtures," *J. Phys. D: Appl. Phys.*, vol. 45, no. 345201, 2012.

[29] F. Sainct, D. Lacoste and C. Laux, "Investigation of water dissociation by Nanosecond Repetitive Pulsed Discharge in superheated steam at atmospheric pressure," in *51th AIAA Aerospace Sciences Meeting including the New Horizons Forum and Aerospace Exposition*, Grapevine, Texas, 2013.

[30] X.-M. Zhu, J. L. Wlash, W.-C. Chen and Y.-K. Pu, "Measurement of the temperal evolution of electron density in a nanosecond pulsed argon microplasma: using both Stark broadening and an OES line-ratio method," *J. Phys. D: Appl. Phys.*, vol. 45, no. 295201, 2012.

[31] D. A. Xu, M. N. Shneider, D. A. Lacoste and C. O. Laux, "Thermal and hydrodynamic effects of nanosecond discharges in atmosphreic pressure air," *J. Phys. D: Appl. Phys*, vol. 47, no. 235202, 2014.

[32] D. Pai, D. Lacoste and C. Laux, "Nanosecond reprtitively pulsed discharge in air at atmospheric pressure - spark regime," *Plasma Sources Sci. Technol.*, vol. 19, no. 065015, 2010.

[33] J. Miles, C. Murray, A. Ross, K. Lemmer, J. Russell and S. Adams, "Time resolved electron density and temperature measurement via Thomson scattering in an atmospheric nanosecond pulsed discharge," *Plasma Sources Sci. Technol.*, vol. 29, no. 07LT02, 2020.

[34] X. Wang and A. Shashurin, "Study of atmospheric pressure plasma jet parameters generated by DC voltage driven cold plasma source," *J. Appl. Phys.*, vol. 122, no. 063301, 2017.

[35] A. Shashurin, D. Scott, T. Zhuang, J. Canady, I. I. Beilis and M. Keidar, "Electric discharge during electrosurgery," *Scientific Reports,* vol. 5, no. 9946, 2015.

[36] A. Sharma, M. N. Slipchenko, M. N. Shneider, X. Wang, K. A. Rahman and A. Shashurin, "Counting the electrons in a multiphoton ionization by elastic scattering of microwaves," *Scientific Reports,* vol. 8, no. 2874, 2018.

[37] A. Shashurin and M. Keidar, "Experimental approaches for studying non-equilibrium atmosphreic plasma jets," *Phys. Plasmas,* vol. 22, no. 122002, 2015.

[38] T. Ombrello, S. H. Won, Y. Ju and S. Williams, "Flame propagation enhancement by plasma excitation of oxygen. part i: Effects of O3," *Combustion and Flames,* vol. 157, pp. 1906-1915, 2010.

[39] W. Sun, S. H. Won and Y. Ju, "In situ plasma activated low temperature chemistry and the s-curve transition in dme/oxygen/helium mixture," *Combustion and Flame,* vol. 161, pp. 2054-2063, 2014.

[40] M. S. Bak, H. Do, M. G. Mungal and M. A. Cappelli, "Plasma-assisted stabilization of laminar premixed methane/air flames around the lean flammability limit," *Combustion and Flame,* vol. 159, no. 10, pp. 3128-3137, 2012.

[41] D. A. Lacoste, J. P. Moeck, D. Durox, C. O. Laux and T. Schuller, "Effect of nanosecond repetitively pulsed dishcarges on the dynamics of a swirl-stabilized lean premixed flame," *Journal of Engineering for Gas Turbines and Power,* vol. 135, no. 101501, 2013.

[42] D. A. Lacoste, D. A. Xu, J. P. Moeck and C. O. Laux, "Dynamic response of a weakly turbulent lean-premixed flame to nanosecond repetitively pulsed discharges," *Proceedings of the Combustion Institute,* vol. 34, pp. 3259-3266, 2013.

[43] J. P. Moeck, D. A. Lacoste, C. O. Laux and C. O. Paschereit, "Control of combustion dynamics in a swirl-stabilized combustor with nanosecond repetitively pulsed discharges," in *51th AIAA Aerospace Sciences Meeting*, 2013.

[44] J. P. Moeck, D. A. Lacoste, D. Durox, T. F. Guiberti, T. Schuller and C. O. Laux, "Stabilization of a methane-air swirl flame by rotating nanosecond spark discharges," *IEEE Transactions on Plasma Science,* vol. 42, pp. 2412-2413, 2014.

[45] D. V. Roupassov, A. A. Nikipelov, M. M. Nudnova and A. Y. Starikovskii, "Flow seperation control by plasma actuator with nanosecond pulsed-periodic discharge," *AIAA Journal,* vol. 47, p. 1680185, 2009.

[46] M. Nishihara, D. Gaitonde and I. Adamovich, "Effect of nanosecond pulse discharges on oblique shock and shock wave-boundarly layer interaction," in *51st AIAA Aerospace Sciences Meeting*, Grapevine, TX, 2013.

[47] K. Kinefuchi, A. Y. Starikovskiy and R. B. Miles, "Control of shock wave-boundary layer interaction using nanosecond dielectric barrier discharge plasma actuators," in *52nd AIAA/SAE/ASEE Joint Propulsion Conference*, Salt Lake City, UT, 2016.

[48] B. DeBlauw, G. Elliot and C. Dutton, "Active control of supersonic base flows with electric arc plasma actuators," *AIAA Journal*, vol. 52, pp. 1-16, 2014.

[49] M. Samimy, M. Kearney-Fischer, J. H. Kim and A. Sinha, "High-speed and high-reynolds number jet control using arc filament plasma actuators," *Journal of Propulsion and Power*, vol. 28, pp. 269-280, 2012.

[50] Y. G. Utkin, S. Keshav, J. H. Kim, J. Kastner, I. V. Adamovich and M. Samimy, "Development and use of localized arc filament plasma actuators for high-speed flow control," *J. Phys. D: Appl. Phys*, vol. 40, pp. 605-636, 2007.

[51] D. L. Rusterholtz, D. A. Lacoste, G. D. Stancu, D. Z. Pai and C. O. Laux, "Ultrafast heating and oxygen disssociation in atmospheric pressure air by nanosecond repetitively pulsed discharges," *J. Appl. D: Appl. Phys*, vol. 46, 2013.

[52] M. S. Bak, W. Kim and M. A. Cappelli, "On the quenching of excited electronic states of molecular nitrogen in nanosecond pulsed dishcarges in atmospheric pressure air," *Appl Phys Lett*, vol. 98, 011.

[53] D. Pai, G. Stancu, D. Lacoste and C. Laux, "Nanosecond repetitively pulsed discharges in air at atmospheric pressure - the glow regime," *Plasma Sources Sci. and Technol.*, vol. 18, no. 045030, 2009.

[54] D. Pai, D. Lacoste and C. Laux, "Nanosecond Repetitive Pulsed Plasmas in Preheated Air at Atmospheric Pressure - The Diffuse Regime," in *39th Plasmadunamcs and Lasers Conference*, Seattle, Washington, 2008.

[55] E. Pfender, "Electric Arcs and Arc Gas Heaters," in *Gaseous Electrocnis Volume 1*, New York, San Francisco, London, Aademic Press, 1978, p. 330.

[56] M. N. Shneider and R. B. Miles, "Microwave diagnostics of small plasma objects," *J. Appl. Phys.*, vol. 98, no. 033301, 2005.

[57] A. Shashurin, D. Scott, T. Zhuang, J. Canady, I. Beilis and M. Keidar, "Electric discharge during electrosurgery," *Scientific Reports*, vol. 4, no. 9946, 2015.

[58] Y. P. Raizer, Gas Discharge Physics, Moscow, Russia: Springer-Verlag, 1987, pp. 350 - 352.

[59] P. Chu and X. Lu, Low Temperature Plasma Technology: Methods and Applications, Boca Raton, FL: CRC Press, 2004.

[60] M. Nishihara, K. Takashima, J. W. Rich and I. V. Adamovich, "Mach 5 bow shock control by a nanosecond pulse surface dielectric barrier discharge," *Physics of Fluids,* vol. 23, 2011.

[61] K. Kinefuchi, A. Y. Starikovskiy and R. B. Mile, in *52nd AIAA/SAE/ASEE Joint Propulsion Conf.*, Salt Late City, UT, 2016.

[62] X. Wang, R. Jagannath, S. Bane and A. Shashurin, "Experimental Study of Modes of Operation of Nanosecond Repetitive Pulsed Discharges in Air," in *AIAA Scitech*, San Diego, CA, 2019.

[63] X. Wang, P. Stockett, R. Jagannath, S. Bane and A. Shashurin, "Time-Resolved Measurements of Electron Density in Nanosecond Pulsed Plasmas Using Microwave Scattering," *Plasma Source Sci. Technol.,* vol. 27, no. 07LT02, 2018.

[64] A. Starikovskiy and N. Aleksandrov, "Plasma-assisted ignition and combustion," *Prog. Energy Combust. Sci.,* vol. 39, pp. 61-110, 2013.

[65] Q. Wang, F. Doll, V. M. Monnedlly, D. J. Economou, N. Sadeghi and G. F. Franz, "Experimental and theoretical study of the effect of gas flow on gas temperature in an atmosphreic pressure microplasma," *J. Phys. D: Appl. Phys.*, vol. 40, pp. 4202-4211, 2007.

[66] P. J. Bruggeman, N. Sadeghi, D. C. Schram and V. Linss, "Gas temperature determinatino from rotational lines in non-equilibrium plasmas: a review," *Plasma Source Sci. Technol.,* vol. 23, no. 023001, 2014.

[67] S. Adams, J. Miles, T. Ombrello, R. Brayfield and J. Lefkowitz, "The effect of inter-pulse coupling on gas temperature in nanosecond-pulsed high-frequency discharges," *J. Phys. D: Appl. Phys,* vol. 52, no. 355203, 2019.

[68] D. L. Rusterholz, D. A. Lacoste, G. D. Stancu, D. Z. Pai and C. O. Laux, "Ultrafast heating and oxygen dissociation in atmosphreic pressure air by nanosecond repetitively pulsed discharges," *J. Phys. D: Appl. Phys,* vol. 46, no. 464010, 2013.

[69] B. Singh, L. K. Rajendran, M. Giarra, P. P. Vlachos and S. P. M. Bane, "Measurement of the flow field induced by a spark plasma using particle image velocimetry," *Experiments of Fluids,* vol. 59, no. 179, 2018.

[70] A. Lo, A. Cessou, P. Boubert and P. Vervisch, "Space and time analysis of the nanosecond scale discharge in atmosphreic pressure air: I. Gas temperature and vibrational distribution function of N2 and O2," *J. Phys. D: Appl. Phys,* vol. 47, no. 115201, 2014.

[71] C. N. Dennis, C. D. Slabaugh, I. G. Boxx, W. Meier and R. P. Lucht, "5 kHz thermometry in a swirl-stabilized gas turbine model combustor using chirped probe pulse femtosecond

CARS. Part 1: Temporally resolved swirl-flame thermometry," *Combustion and Flame,* vol. 173, pp. 441-453, 2016.

[72] S. Roy, W. D. Kulatilaka, D. R. Richardson, R. P. Lucht and J. R. Gord, "Gas-phase single-shot thermometry at 1 kHz using fs-CARS spectroscopy," *Optics Letters,* vol. 34, no. 24, 2009.

[73] A. Lo, G. Cleon, P. Vervisch and A. Cessou, "Spontaneous Raman scattering: a useful tool for investigating the afterflow of nanosecond scale discharges in air," *Appl Phys B,* vol. 107, pp. 229-242, 2012.

[74] X. Wang and A. Shashurin, "Study of atmospheric pressure plasma jet parameters generated by DC voltage driven cold plasma source," *J. Appl. Phys.,* vol. 122, no. 063301, 2017.

[75] A. Sharma, M. N. Slipchenko, M. N. Shneider, X. Wang, K. A. Rahman and A. Shashurin, "Counting the electrons in a multiphoton ionization by elastic scattering of microwaves," *Sci. Reports,* vol. 8, no. 2874, 2018.

[76] X. Wang, P. Stockett, R. Jagannath, S. Bane and A. Shashurin, "Time-resolved measurements of electron density in nanosecond pulsed plasmas using microwave scattering," *Plasma Sources Sci. Technol.,* vol. 27, no. 07LT02, 2018.

[77] X. Wang and A. Shashurin, "Study of the transition between modes of nanosecond repetitive pulsed discharge," in *AIAA Aviation*, Dallas, TX, 2019.

[78] X. Wang and A. Shashurin, "Gas thermometry by optical emission spectroscopy enhanced with probing nanosecond plasma pulse," *AIAA Journal,* vol. 58, no. 7, 2020.

[79] R. B. Miles, W. R. Lempert and J. N. Forkey, "Laser Rayleigh scattering," *Meas. Sci. Technol.,* vol. 12, pp. R33-R51, 2001.

[80] M. Boyda, G. Byun and K. T. Lowe, "Investigation of velocity and temperature measurement sensitivities in cross-correlation filtered Rayleigh scattering (CCFRS)," *Meas. Sci. Technol.,* vol. 30, no. 044004, 2019.

[81] R. L. McKenzie, "Progress in Laser Spectroscopic Techniques for Aerodynamic Measurements: An Overview," *AIAA Journal,* vol. 31, no. 3, 1993.

[82] F.-q. Zhao and H. Hiroyasu, "The application of laser Rayleigh scattering to combustion diagnostics," *Prog. Energy Combst. Sci.,* vol. 19, pp. 447-485, 1993.

[83] X. Wang, R. Jagannath, S. Bane and A. Shashurin, "Experimental study of modes of operation of nanosecond repetitvely pulsed discharges in air," in *AIAA Scitech*, San Diego, 2019.

[84] C. Limbach, C. Dumitrache and A. P. Yalin, "Laser light scattering from equilibrium, high temperature gases: limitations on Rayleigh scattering thermometry," in *AIAA Plasmadynamics and lasers conference*, Washington, D.C., 2016.

[85] C. M. Limbach, *Characterization of nanosecond, femtosecond and dual pulse laser energy deposition in air for flow control and diagnostic applications,* PhD Thesis, 2015.

[86] A. Lo, A. Cessou and P. Verrisch, "Space and time analysis of the nanosecond scale discharges in atmospheric pressure air: II. Energy transfers during the post-discharge," *J. Phys. D: Appl. Phys,* vol. 47, no. 115202, 2014.

[87] N. A. Popov, "Pulsed nanosecond discharge in air at high specific deposited energy: fast gas heating and active particle production," *Plasma Sources Sci. Technol.,* vol. 25, no. 044003, 2016.

[88] Y. Itikawa, "Cross sections for electron collisions with nitrogen molecules," *Journal of Physical and Chemical Reference Data,* vol. 35, no. 31, 2006.

[89] Y. Itikawa and A. Ichimura, "Cross section for collisions of electrons and photons with atomic oxygen," *Journal of Physical and Chemical Reference Data,* vol. 19, no. 637, 1990.

[90] R. D. Hake and A. V. Phelps, "Momentum-transfer and inelastic-collision cross sections for electrons in O2, CO, and CO2," *Physical Review,* vol. 158, no. 1, 1967.

[91] J. Miles, C. Murray, A. Ross, K. Lemmer, J. Russell and S. Adams, "Time resolved electron density and temperature measurements via Thomson scattering in an atmospheric nanosecond pulsed discharge," *Plasma Sources Sci. Technol.,* vol. 29, no. 07LT02, 2020.

[92] A. Dogariu, M. N. Shneider and R. B. Miles, "Versatile radar measurement of the electron loss rate in air," *Appl. Phys. Lett.,* vol. 103, no. 224102, 2013.

[93] J. J. Jennon and M. J. Mulcapy, "Microwave measurement of attachment in oxygen-nitrogen mixtures," *Proc. Phys. Soc.,* p. 78, 1543.

[94] D. Spence and G. J. Schulz, "Three-body attachment in O2 using electron beams," *Physical Review A,* vol. 5, no. 2, 1972.

[95] X. Deng, A. Y. Nikiforov, P. Vanraes and C. Leys, "Direct current plasma jet at atmosphreic pressure operating in nitrogen and air," *J. Appl. Phys.,* vol. 113, no. 023305, 2013.

[96] M. Thiyagarajan and J. Scharer, "Experimental investigation of ultraviolet laser induced plasma density and temperature evolution in air," *J. Appl. Phys.,* vol. 104, no. 013303, 2008.

[97] A. Sharma, E. L. Braun, A. R. Patel, K. A. Rahman, M. N. Slipchenko, M. N. Shneider and A. Shashurin, "Diagnostics of CO concentration in gaseous mixtures at elevated pressures by resonance enhanced multi-photon ionization and microwave scattering," *J. Appl. Phys.,* vol. 128, no. 141301, 2020.

[98] A. Lo, A. Cessou, C. Lacour, B. Lecordier, P. Boubert, D. A. Xu, C. O. Laux and P. Vervisch, "Streamer-to-spark transition initiated by a nanosecond overvoltage pulsed discharge in air," *Plasma Sources Sci. Technol.,* vol. 26, no. 045012, 2017.

[99] A. Chelouah, E. Marode, G. Hartmann and S. Achat, "A new method for temperature evaluation in a nitrogen discharge," *J. Phys. D: Appl. Phys.,* vol. 27, pp. 940-945, 1994.

[100] X. L. Deng, A. Y. Nikiforov, P. Vanraes and C. Leys, "Direct current plasma jet at atmospheric pressure operating in nitrogen and air," *J. Appl. Phys.,* vol. 113, no. 023305, 2013.

[101] Q. Y. Zhang, D. Q. Shi, W. Xu, C. Y. Miao, C. Y. Ma, C. S. Ren, C. Zhang and Z. Yi, "Determination of vibrational and rotational temperatures in highly constricted nitrogen plasmas by fitting the second positive system of N2 molecules," *AIP Advances,* vol. 5, no. 057158, 2015.

[102] S. D. Popa, "Vibrational distribution in a flowing nitrogen glow discharge," *J. Phys. D: Appl. Phys.,* vol. 29, pp. 411-415, 1996.

[103] X. Wang, A. Patel and A. Shashurin, "Combined microwave and laser Rayleigh scattering diagnostics for pin-to-pin nanosecond discharges," *J. Appl. Phys.,* vol. 129, no. 183302, 2021.

[104] A. Roettgen, I. Shkurenkov, M. S. Simeni, V. Petrishchev, I. V. Adamovich and W. R. Lempert, "Time-resolved electron density and electron temperature measurements in nanosecond pulse discharge in helium," *Plasma Sources Sci. Technol.,* vol. 25, no. 055009, 2015.

[105] T. Shao, V. F. Tarasenko, C. Zhang, M. I. Lomaev, D. A. Sorokin, P. Yan, A. V. Kozyrev and E. K. Baksht, "Spark discharge formation in an inhomogeneous electric field under conditions of runaway electron generation," *J. Appl. Phys.,* vol. 111, no. 023304, 2012.

[106] V. F. Tarasenko, E. K. Baksht, A. G. Gurachenko, I. D. Kostyrya, M. I. Lomaev and D. V. Rybka, "Generation of supershort avalanche electron beams and formation of diffuse discharge in different gases at high pressure," *Plasma Devices and Operations,* vol. 16, no. 4, 2008.

[107] B. Isak, Plasma and Spot Phenomena in Electrical Arcs, Gewerbestrasse, Switzerland: Springer, 2020.

[108] I. A. Kossyi, A. Y. Kostinsky, A. A. Matveyev and V. P. Silakov, "Kinetic scheme of the non-equilibrium discharge in nitrogen-oxygen mixtures," *Plasa Sources Sci. Technol.,* vol. 1, pp. 207-220, 1992.

[109] J. Dutton, "A survey of electron swarm data," *J. Phys. Chem. Ref. Data.,* vol. 4, no. 577, 1975.

[110] S. Stepanyan, N. Minesi, A. Tibere-Inglesse, A. Salmon, G. D. Stancu and C. O. Laux, "Spatial evolution of the plasma kernel produced by nanosecond discharge in air," *J. Phys. D. Appl. Phys.,* vol. 52, no. 29, 2019.

[111] B. Singh, L. K. Rajendran, P. P. Vlachos and S. P. M. Bane, "Two regime cooling in flow induced by a spark discharge," *Phys. Rev. Fluids,* vol. 5, no. 1, p. 14501, 2020.

[112] B. Singh, L. K. Rajendran, J. Zhang, P. P. Vlachos and S. P. M. Bane, "Vortex rings drive entrainment and cooling in flow induced by a spark discharge," *Phys. Rev. Fluids,* vol. 5, p. 114501, 2020.

[113] M. N. Shneider and R. B. Miles, "Microwvae diagnostics of small plasma objects," *J. Phys. D: Appl. Phys,* vol. 98, no. 033301, 2005.

[114] A. Fridman, Plasma Chemistry, Cambridge University Press, 2008.

[115] M. Laroussi, "The biomedical application of plasma: A brief history of the development of a new field of research," *IEEE Trans. Plasma Sci.,* vol. 36, no. 4, pp. 1612 - 1614, 2008.

[116] M. Keidar, R. Walk, A. Shashurin, P. Srinivasan, A. Sandler, S. Dasgupta, R. Ravi, R. Guerrero-Preston and B. Trink, "Cold plasma selectivity and the possibility of a paradigm shift in cancer therapy," *British Journal of Cancer,* vol. 105, pp. 1295 - 1301, 2011.

[117] A. Shashurin, M. Keidar, S. Bronnikov, R. A. Jurjus and M. A. Stepp, "Living tissue under treatment of cold plasma atmospheric jet," *Appl. Phys. Lett,* vol. 93, no. 181501, pp. 1 - 4, 2008.

[118] G. Morfill and J. Zimmermann, "Plasma Health Care - Old Problems, New Solutions," *Contrib. Plasma Phys,* vol. 52, no. 7, pp. 655 - 663, 2012.

[119] G. Fridman, G. Fridman, A. Gutsol, A. B. Shekhter, V. N. Vasilets and A. Fridman, "Applied Plasma Medicine," *Plasma Process. Polym,* pp. 503-533, 2008.

[120] L. Brulle, M. Vandamme, D. Ries, E. Martel, E. Robert, S. Lerondel, V. Trichet, S. Richard, J.-M. Pouvesle and A. Le Pape, "Effects of a Non Thermal Plasma Treatment Alone or in Combination with Gencitabine in a MIA PaCa2-Iuc Orthotopic Pancreatic Carcinoma Model," *PLOS ONE,* vol. 7, no. 12, 2012.

[121] M. Keidar, A. Shashurin, O. Volotskova, M. A. Stepp, P. Srinivasan, A. Sandler and B. Trink, "Cold atmospheric plasma in cancer therapy," *Physics of Plasmas,* vol. 20, no. 057101, 2013.

[122] Y. Duan, C. Huang and Q. Yu, "Low-Temperature Direct Current Glow Discharges at Atmospheric Pressure," *IEEE Trans. Plasma Sci,* vol. 33, no. 2, pp. 328 - 329, 2005.

[123] A. Shashurin and M. Keidar, "Experimental approches for studying non-equilibrium atmospheric plasma jets," *Physics of Plasmas,* vol. 22, no. 122002, pp. 1 - 10, 2015.

[124] H. Luo, Z. Liang, B. Lv, X. Wang, Z. Guan and L. Wang, "Observation of the transition from a Townsend discharge to a glow discharge in helium at atmospheric pressure," *Appl. Phys. Lett,* vol. 91, no. 221504, pp. 1 - 3, 2007.

[125] I. Radu, R. Bartnikas and M. R. Wertheimer, "Dielectric barrier discharges in atmospheric pressure helium incylinder-plane geometry: experiments and model," *J. Phys. D: Appl. Phys.,* vol. 37, pp. 449 - 462, 2004.

[126] I. Radu, R. Bartnikas and M. R. Wertheimer, "Frequency and Voltage Dependence of Glow and Pseudoglow Discharges in Helium Under Atmospheric Pressure," *IEEE Trans. Plasma Sci.,* vol. 31, no. 6, pp. 1363 - 1378, 2003.

[127] F. Tochikubo, T. Chiba and T. Watanabe, "Structure of Low-Frequency Helium Glow Dishcarge at Atmospheric Pressure between Parallel Plate Dielectric Electrodes," *Japanese Journal of Applied Physics,* vol. 38, pp. 5244 - 5250, 1999.

[128] K. Urabe, T. Morita, K. Tachibana and B. N. Ganguly, "Investigation of discharge mechanisms in helium plasma jet at atmospheric pressure by laser spectroscopic measurements," *J. Phys. D: Appl. Phys,* vol. 43, no. 095201, 2010.

[129] Q. Xiong, X. P. Lu, K. Ostrikov, Y. Xian, C. Zou, X. Xiong and Y. Pan, "Pulsed dc- and sine-wave-excited cold atmospheric plasma plumes: A comparative analysis," *Physics of Plasmas,* vol. 17, no. 043506, pp. 1 - 8, 2010.

[130] G. V. Naidis, "Modelling of plasma bullet propagation along a helium jet in ambient air," *J. Phys. D: Appl. Phys.,* vol. 44, no. 215203, pp. 1 - 5, 2011.

[131] G. V. Naidis, "Modeling of plasma jets emerged into ambient air: Influence of applied voltage, jet radius, and helium flow velocity on plasma jet characteristics," *J. Appl. Phys.,* vol. 112, no. 103304, pp. 1 - 5, 2012.

[132] R. Morrow and J. J. Lowe, "Streamer propagation in air," *J. Phys. D: Appl. Phys.,* vol. 30, pp. 614 - 627, 1997.

[133] W. J. Yi and P. F. Williams, "Experimental study of streamers in pure N2 and N2/O2 mixtures and a ≈13 cm gap," *J. Phys. D: Appl. Phys,* vol. 35, pp. 205 - 218, 2002.

[134] G. E. Georghious, A. C. Metaxas and R. Morrow, "The effect of photoemission on the streamer development and propagation in short uniform gaps," *Appl. Phys. Lett,* vol. 34, pp. 200 - 208, 2001.

[135] X. L. Deng, A. Y. Nikiforov, P. Vanraes and C. Leys, "Direct current plasma jet at atmospheric pressure operating in nitrogen and air," *Journal of applied physics,* 2013.

[136] K. Matra, "DC non-thermal atmospheric-pressure plasma jet generated using a syringe needle electrode," *Japanese Journal of Applied Physics,* 2016.

[137] Y. Xian, S. Wu, Z. Wang, Q. Huang, X. Lu and J. F. Kolb, "Discharge Dynamics and Modes of an Atmospheric Pressure Non-Equilibrium Air Plasma Jet," *Plasma Process and Polymers,* 2013.

[138] K. Hensel, K. Kucerova, B. Tarabova, M. Janda and Z. Machala, "Effects of air transient spark discharge and helium plasma jet on water bacteria, cells, and biomolecules," *Biointerphase,* 2015.

[139] R. Morrow, "The theory of positive glow corona," *J. Phys. D: Appl. Phys.,* vol. 30, pp. 3009 - 3114, 1997.

[140] K. Yan, T. Yamamoto, S. Kanazawa, T. Ohkubo, Y. Nomoto and J.-S. Chang, "Control of Flow Stabilized Positive Corona Discharge Modes and NO Removal Characteristic in Dry Air by CO2 Injection," *Journal of Electrostatics,* vol. 46, pp. 207 - 219, 1999.

[141] Y. P. Raizer, G. M. Milikh, M. N. Shneider and S. V. Novakovski, "Long streamers in the upper atmosphere above thundercloud," *J. Phys. D: Appl. Phys,* vol. 31, pp. 3255 - 3264, 1998.

[142] J. D. Jackson, Classical Electrodynamics, Wiley, 1998.

[143] A. Shashurin, M. N. Sneider and M. Meidar, "Measurement of streamer head potential and conductivity of streamer column in cold nonequilibrium atmospheric plasmas," *Plasma Sources Sci. Technol.,* vol. 21, no. 034006, pp. 1 - 6, 2012.

[144] X. Lu, G. Naidis, M. Laroussi and K. Ostrikov, "Guided ionization waves: Theory and experiments," *Physics Reports,* vol. 540, pp. 123 - 166, 2014.

[145] M. Keidar, R. Walk, A. Shashurin, P. Srinivasan, A. Sandler, S. Dasgupta, R. Ravi, R. Guerrero-Preston and B. Trink, "Cold plasma selectivity and the possibility of a paradigm shift in cancer therapy," *Br. J. Cancer,* vol. 105, pp. 1295-1301, 2011.

[146] A. Shashurin, M. Keidar, S. Bronnikov, R. A. Jurjus and M. A. Stepp, "Living tissue under treament of cold plasma atmospheric jet," *Appl. Phys. Lett,* vol. 93, no. 181501, 2008.

[147] G. E. Morfill and J. L. Zimmermann, "Plasma Health Care - Old Problems, New Solutions," *Contrib. Plasma Phys.,* vol. 52, no. 7, pp. 655-663, 2012.

[148] Y. Lee, W. Jung, Y. Choi, J. Oh, S. Jang, Y. Son, M. Cho and W. Namkung, "Application of Pulsed Corona Induced Plasma Chemical Process to an Industrial Incinerator," *Envion. Sci. Technol.,* vol. 37, pp. 22563-2567, 2003.

[149] T. Corke, C. Enloe and S. P. Wilkinson, "Dielectric Barrier Discharge Plasma Actuators for Flow Control," *Annu. Rev. Fluid Mech.,* vol. 42, no. 505-29, 2010.

[150] B. Chua, A. S. Wexler, N. C. Tien, D. A. Niemeier and B. A. Holmen, "Design, fabrication, and testing of a microfabricated corona ionizer," *Journal of Microelectromechanical System,* vol. 17, no. 1, pp. 115-123, 2008.

[151] M. Park, A. Son and B. Chua, "Microorganism-ionizing respirator with reduced breathing resistance suitable for removing airborne bacteria," *Sensors and Actuator B: Chemical,* vol. 276, pp. 437-446, 2018.

[152] E.-H. Lee, H.-J. Lim, A. Son and B. Cua, "A disposable bacterial lysis cartridge (BLC) suitable for an in-situ water-borne pathogen detection system," *Analyst,* vol. 140, pp. 7776-7783, 2015.

[153] B. Chua and A. Son, "Sensing absolute air pressure using micro corona discharge," *Sensors and Actuators A: Physical,* vol. 217, pp. 49-55, 2014.

[154] B. Chua and J. J. Pak, "Miniaturized corona flow sensor operating in drift mobility incremnet mode for low flow velocity measurement," *Sensors and Actuators A: Physical,* vol. 224, pp. 65-71, 2015.

[155] A. Fridman and L. A. Kennedy, Plasma Physics and Engineering, Boca Ranton, FL: CRC Press, 2011.

[156] M. Goldman and A. Goldman, "Corona Dishcarge," in *Gaseous Electronics, Volume I: Elecctrical Discharges,* New York, Academic Press Inc, 1978, pp. 238-242.

[157] X. Wang and A. Shashurin, "DC-driven plasma gun: self-oscillatory operation mode of atmospheric-pressure helium plasma jet comprised of repetitive streamer breakdowns," *Plasma Source Sci. Techno.,* vol. 26, no. 02T02, 2017.

[158] Y. Akishev, V. Karalnik, I. Kochetov, A. Napartovich and N. Trushkin, "High-current cathode and anode spots in gas discharges at moderate and elevated pressures," *Plasma Sources Sci Technol.*, vol. 23, no. 054013, 2014.

[159] G. Hartmann and I. Gallimberti, "The influence of metastable molecules on the streamer progression," *J. Phys. D" Appl. Phys.*, vol. 8, pp. 670-680, 1975.

[160] N. A. Popov, "Associative Ionization Reacitons Involving Excited Atoms in Nitrogen Plasma," *Plasma Physics Reports,* vol. 35, no. 5, pp. 436-449, 2009.

[161] M. Goldman, A. Goldman and R. S. Sigmond, "The corona discharge, its properties and specific uses," *Pure Appl. Chem.*, vol. 57, no. 9, pp. 1353-1362, 1985.

[162] A. C. Gentile and M. J. Kushner, "Reaction chemstry and optimization of plasma remediation of NxOy from gas streams," *J. Appl. Phys.*, vol. 78, no. 3, pp. 2074-2085, 1995.

[163] M. Kogoma and S. Okazaki, "raising of ozone formation efficiency in a homogeneous glow discharge plasma at atmosphreic pressure," *J. Phys. Phys.*, vol. 27, no. 9, pp. 1985-1987, 1994.

[164] M. A. Malik, "Nitric Oxide Production by High Voltage Electrical Discharges for Medical Uses: A Review," *Plasma Chem. Plasma Process,* vol. 36, no. 3, pp. 737-766, 2016.

[165] M. Thiyagarajan, A. Sarani and C. Nicula, "Optical emission spectroscopic diagnostics of a non-thermal atmospheric pressure helium-oxygen plasma jet for biomedical applications," *J. Appl. Phys.*, vol. 113, no. 233302, 2013.

[166] E. Gochenbach and W. Hauschild, "The selection of the frequency range for high-voltage on-site testing of extruded insulation cable systems," *IEEE Insul. Mag.*, vol. 16, no. 6, pp. 11-16, 2000.

[167] G. L. Skibinski, R. J. Kerkman and D. Schlegel, "EMI emissions of modern PWM AC drivers," *IEEE Industry Applications Magazine,* vol. 5, no. 6, pp. 47-81, 1999.

[168] A. Shashurin, Encyclopedia of Plasma Technology, Taylor & Francis, 2017.

[169] X. Wang and A. Shashurin, "DC-driven plasma gun: self-oscillatory operation mode of atmospheric-pressure helium plasma jet comprised of repetitive streamer breakdowns," *Plasma Sources Sci. Technol,* vol. 26, no. 2, pp. 1-6, 2017.

[170] S. O. Macheret, M. N. Shneider and R. B. Miles, "Modeling of air plasma generation of repetitive high-voltage nanosecond pulses," *IEEE transactions on plasma science,* vol. 30, no. 3, 2002.

[171] J. T. Horstmann, P. Hennigsson, A. L. Thomas and R. J. Bomphrey, "Wake development behind paired wings with tip and root trailing vortices: consequences for animal flight force estimates," *PloS ONE*, vol. 9(3), no. e91040, 2014.